The origin of surface recrystallization in extrusion of 6xxx aluminum alloys.

The Origin of Surface Recrystallization in Extrusion of 6xxx Aluminum Alloys

by

William H. Van Geertruyden

Presented to the Graduate and Research Committee

of Lehigh University

in Candidacy for the Degree of

Doctor of Philosophy

in

Materials Science and Engineering

Lehigh University

April 30, 2004

Approved and recommended for acceptance as a dissertation in partial fulfillment of the requirements for the degree of Doctor of Philosophy.

4/20/2004
Date

Dr. Wojciech Z. Misiolek
Dissertation Advisor

4/20/2004
Accepted Date

Committee Members:

Dr. Marcelo Goncalves

Dr. Arnold Marder

Dr. Michael Notis

Dr. Paul Wang

ACKNOWLEDGEMENTS

I would like to thank the following individuals and organizations for their contribution to this work. Money takes precedent in this country and this dissertation would not have been possible without the funding from the Department of Energy, Contract #: DE – FC07 – O1ID14191.

I would like to begin by thanking the enormous help of my advisor and committee chairman, Dr. Wojciech Misiolek. I never would have thought that six years after stepping into his office and talking about aluminum that I would be where I am today. His professional and personal advice has proven to be invaluable in my young career.

I would also like to thank the tremendous effort from my dissertation committee in their help to steer the direction of my research in times of doubt. First, I would like to thank Dr. Michael Notis for joining the committee in mid – journey and helping me in my research effort. I owe many thanks to Dr. Arnold Marder for teaching me the fundamentals of physical metallurgy and advice on life, research and how to be a professional. Thanks to Dr. Paul Wang for sharing his knowledge of metal processing and fundamentals of physical metallurgy. One of these days, I will see him on a ski slope or golf course, preferably the latter. Finally, thanks to Dr. Marcelo Goncalves for extensive discussions and debates of the fundamentals of deformation and annealing behavior in metals. Also many thanks for his hospitality in Sao Paulo where many of the seeds of this research were planted.

The laboratory engineers and technicians at Lehigh also contributed much to this work. Dave Ackland and Bill Mushock helped tremendously with all the Scanning Electron Microscopy work as well as EBSD. Arlan Benscoter helped a great deal in the procedure of electroetching as well as all of the light optical microscopy. His talent and knowledge of metallography are world – class and much of my knowledge of metallography is thanks to him.

Many of the results presented in this research have been produced with the help of members of Alcoa, Inc. The small – scale extrusion experiments were performed at Alcoa Technical Center in Monroeville, PA by Joe Genito. Many thanks also to the advice and information from Jaakko Suni whose knowledge in physical metallurgy and texture was incredibly valuable. Walt Cebulak, Dan Severa, and the rest of the ATC staff were extremely hospitable as well in all of my journeys to the western part of the state. I owe many thanks to Jeff Victor for giving me the industrial perspective and also his help with industrial extrusion experiments performed at Alcoa Engineered Products in Cressona, PA.

The hot torsion experiments were performed by the very capable and professional staff at Dynamic Systems, Inc. in Poestenkill, NY. Specifically, Rick Welch, Chris Christian, Todd Bonesteel, and Dave Ferguson deserve my appreciation for their hospitality and for helping me figure out how to twist hot aluminum in less than a ¼ second without breaking it. I promise no more "dummy samples."

This dissertation would not have been possible without the help of the IMF crew and graduate students who helped me through difficult times and some tough

experimentation throughout the years: Alex Bandar, Heather Browne, Steven Claves, Mario Epler, Frank Gift, Kai Lorcharoensery, Andy Prescott and my boys Mike Giunta and Neil Hurley. Also thanks to Brian Newbury for his friendship and support over the years.

Finally, I would like to thank my devoted family and friends who gave me much love and support over the many years of graduate work. To my brothers, I continue to look up to you both for inspiration. It is always comforting knowing that I have you both to depend on for support. To my mother and father, thank you for love and encouragement throughout the years.

I do not know what I may appear to the world; but to myself I seem to have been only like a boy playing on the seashore, and diverting myself in now and then finding a smoother pebble or a prettier shell than ordinary, whilst the great ocean of truth lay all undiscovered before me.

- *Sir Isaac Newton*

TABLE OF CONTENTS

List of Tables

List of Figures

Figure 102: Proposed theory of Peripheral Coarse Grain (PCG) structure formation based on experimental results in this research. Frames a – d represent the microstructural evolution during deformation, while E – F represent the microstructural evolution during annealing. High angle grain boundaries are marked by dark lines and low angle grain boundaries by light gray.

Figure 103: PCG depths measured from small – scale extrusion experiments as a function of the calculated average Zener Hollomon parameter, $Z_{avg.}$ for both alloys studied.

Figure 104: Plot of Log Z based on the maximum strain rate and temperature achieved at the center and surface of the extrusion from numerical simulation results.

Figure 105: Depth of PCG versus values of the Zener Hollomon Parameter, Z at the surface of the extrudate based on Finite Element Model results. The extrusion parameters used were R = 40, and ram speed = 1.3 mm/s.

Figure 106: Average grain radius, $R_{avg.}$ as a function of volume fraction to particle diameter, F_v / d ratio. Lines represent regions where A) Broadening of Grain Size Distribution (W<0.1), B) Normal + Abnormal Grain Growth (0.1>W>0.25), C) Abnormal Grain Growth only (0.25>W>1), and D) No Growth occur (W>1).

Figure 107: Average grain radius, $R_{avg.}$ as a function of volume fraction to particle diameter, F_v / d ratio. Lines represent regions where Normal Grain Growth, Abnormal Grain Growth, and No Growth occur. The F_v / d ratio for the low Cr 6061 alloy is shown as a dark vertical line. Average grain radius after high and low $T_{def.}$ torsion of the low Cr 6061 alloy are shown.

Figure 108: Flow chart for conditions whereby Abnormal Grain Growth occurs in a high stacking fault material deformed to large strains.

List of Symbols and Abbreviations

The following symbols have been used in this research. Wherever appropriate, the value of the constant has been identified in the text. In some cases, traditional symbols have been altered to avoid confusion within the text.

α	Constant
β	Constant
b	Burgers vector
b'	Constant
C	Constant
d	Dispersoid particle diameter
δ	Subgrain diameter
D	Grain size (diameter)
D_0	Original grain size (diameter)
D_b	Starting billet diameter
E_D	Energy per unit volume resolved from grain boundaries
ε	Strain
ε_{eff}	Effective strain
ε_c	Critical strain
$\dot{\varepsilon}$	Strain rate
$\dot{\varepsilon}_{avg}$	Average strain rate
γ	Grain boundary energy
γ_i	Grain boundary energy of an individual grain in an average grain assembly

γ_{avg}	Average grain boundary energy of an average grain assembly
γ_m	Critical grain boundary (15° misorientation)
ϕ	Rotation of torsion in radians
F_v	Volume fraction of second phase dispersoids
G	Shear modulus
Γ	Dislocation line tension
K	Constant
K_1	Constant
L	Torsion sample gauge length
L_d	Average distance of dislocation movement
m	Strain rate sensitivity exponent
M	Grain boundary mobility
M_{avg}	Average mobility of an average grain assembly
M_i	Mobility of an individual grain within an average grain assembly
ν	Poissons ratio
n	Avrami exponent
P_D	Driving pressure for recrystallization
P_Z	Drag force imposed by a dispersion of second phase particles
Q	Activation energy
ρ	Dislocation density
r	Torsion gauge length radius
R	Extrusion ratio

R_{avg}	Average grain radius of an average grain assembly
R_i	Individual grain radius in an average grain assembly
R_{lim}	Limiting grain radius for abnormal grain growth in an average grain assembly
R_G	Universal gas constant
t	Time
T	Temperature
T_{def}	Deformation temperature
T_{start}	Starting billet temperature for small – scale extrusion experiments
v	Ram speed
W	Constant representing relationship between average grain radius, volume fraction and diameter of dispersoids
X_V	Volume fraction recrystallized
Z	Zener Hollomon parameter
Z_{avg}	Average Zener Hollomon parameter based on an average strain rate

cDRX	Continuous Dynamic Recrystallization
DMZ	Dead Metal Zone
DRX	Dynamic Recrystallization
DSC	Differential Scanning Calorimetry
EBSD	Electron Backscatter Diffraction
EDS	Energy Dispersive Spectroscopy
gDRX	Geometric Dynamic Recrystallization
JMAK	Johnson Mehl Avrami Kolmogorov
LOM	Light Optical Microscopy
ND	Normal Direction
OIM	Orientation Imaging Microscopy
PCG	Peripheral Coarse Grain
PSN	Particle Stimulated Nucleation
SEM	Scanning Electron Microscopy
SIBM	Strain Induced Boundary Migration
SRX	Static Recrystallization
TD	Transverse Direction
TEM	Transmission Electron Microscopy

ABSTRACT

During extrusion of many aluminum alloys, surface imperfections may be present as a result of imposed processing parameters. One such surface imperfection is the presence of coarse grains at the surface, known as a Peripheral Coarse Grain (PCG) structure that has been known to affect mechanical properties and aesthetics of the extruded material. The objective of this research is to understand the origin of the PCG structure in 6xxx series aluminum alloys and further understand the effect of processing parameters on its appearance.

Physical simulation experiments were performed and included small – scale and industrial – scale extrusion as well as hot torsion testing at elevated values of strain and temperature compensated strain rate, Z. The results from small – scale extrusion experiments show that with increasing ram speed, extrusion ratio, starting billet temperature, and decreasing amount of Cr, the depth of the PCG structure increases. Upon further characterization of the extrusion discard, it has been concluded that the primary mechanism of the coarse grain formation in extrusion is the result of a static recrystallization process. In the absence of the coarse grain structure, a microstructure that consisted of fine, equiaxed grains was present in extrusion which was consistent with the one at the surface of samples after hot torsion to effective strains greater than 2.5. It was determined that due to the high cooling rate after hot torsion testing, that the fine, equiaxed microstructure is created as a result of a dynamic process such as continuous dynamic recrystallization or geometric dynamic recrystallization.

Due to the presence of the fine, equiaxed high angle grain boundaries present after large strain deformation, the models that define stored energy from the measurement of subgrain size and subgrain misorientation should not be used to accurately predict the PCG structure. A theoretical model, based on the microstructural evolution in extrusion, has been developed here that relates the grain size after hot deformation to the occurrence of abnormal grain growth in a material that contains a homogeneous dispersion of fine particles. Future experiments have been suggested that will quantitatively predict the PCG depth in extrusion.

1.0 INTRODUCTION

Aluminum and its alloys are generally regarded as having high formability when compared to other engineering materials. Given their high ductility, relatively low flow stress and face centered cubic crystal structure, complex parts using these alloys can be formed at relatively low pressures. Aluminum alloys are attractive for industries concerned with weight savings, corrosion resistance, and those seeking a good combination of mechanical properties. Over the past seventy-five years, the aluminum industry has taken advantage of this combination of properties. However in recent years aluminum alloys are being sought after even more for applications in high performance sectors such as the automotive, aerospace, and building/construction industries. More than ever, the quality of the product, in terms of both mechanical properties and surface quality, is being highly scrutinized. In addition, it is not currently economical to use aluminum in many of these applications because the cost of forming aluminum with desired structural characteristics is high. This high cost is partially due to the fact that extrusion is a batch process that has much inherent inefficiency. When the aluminum product is extruded, if mechanical properties or surface characteristics are not within specification, the material must be scrapped and recycled. This action will increase the energy consumption and cost of the processed aluminum. According to the Aluminum Association's *Aluminum Statistical Review for 1999*, U.S. product net shipments of extruded shapes, extruded pipe & tube, and rod & bar was 4,278 million pounds.[1] A 2% increase in aluminum recovery would result in extrusion scrap reduction of 85 million pounds per year. This means that 85 million

pounds per year of extruded aluminum would not have to be scrapped, re – melted, re – cast, re – preheated and re – extruded at an estimated total cost of $0.22 per pound. Thus the cost savings to the U.S. extrusion industry of a 2% reduction in scrap is estimated to be over $18 million per year.

Despite research efforts to limit and even eliminate undesirable features and properties in aluminum alloy extrusions, there still exist imperfections whose origins have not yet been fully understood. One such group of imperfections is one that presents itself on the surface of an extrudate. These imperfections are highly undesirable, as they have been attributed to a reduction in mechanical properties as well as visual aesthetics. There are many surface imperfections that may form during aluminum extrusion. These imperfections include: heat checking, pick – up, "orange peel," and a Peripheral Coarse Grain (PCG) structure as they are known in industrial practice. Since all of these surface imperfections form as a result of the extrusion process, it can be assumed that a change in processing parameters will be able to limit or even eliminate them. The PCG structure is particularly important to reduce or eliminate due to its effect on mechanical properties and aesthetics. This imperfection presents itself as a collection of large recrystallized grains at the periphery of an extruded product. As most aluminum alloys receive some surface treatment, whether it is anodization, inorganic coating, machining, or other chemical treatment, all of these processes will be directly affected by the grain characteristics on the surface of the extrudate. Additionally, a significant amount of the extrusions produced using the alloys studied in this research are used as bar stock for machining applications or as

feedstock in a forging process. Therefore, mechanical properties of the PCG structure vs. the inner unrecrystallized core are critical in determining the machining characteristics or quality of the forged product.

In this research, the origin of the PCG structure has been investigated due to its industrial significance. It is important to understand the evolution of the microstructure as it is carried into the surface of the product. A detailed investigation into the effect of processing parameters on its occurrence has been made here. In order to predict its formation, a model of PCG development has been developed and proposed based on the microstructural development during deformation.

2.0 BACKGROUND

2.1 Aluminum Extrusion

2.1.1 Extrusion Practice and Procedure

The production of modern aluminum extrusion has been in practice for over seventy five years. The process involves forcing a block of an aluminum billet with a ram through a die with a given orifice. The billet is typically round for extrusion as compared to a rectangular shape in rolling. This process is usually performed at high temperatures, typical for hot the working regime without the use of lubrication. The extrusion process is either performed by an indirect or direct method as can be seen in Figure 1. The process is capable of producing extrudates of a given cross – sectional dimension with good tolerances, a hollow cross – section, and a wide array of structural features.

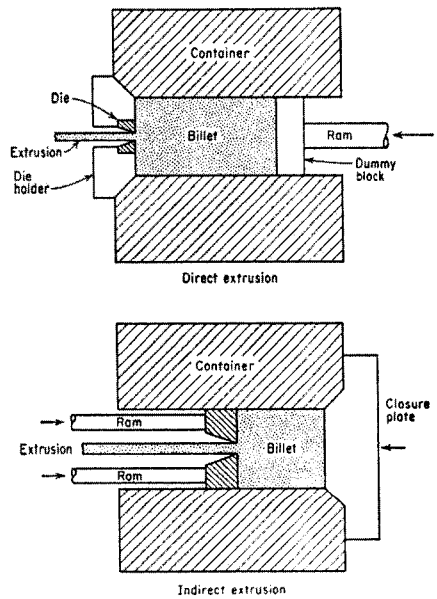

Figure 1: Schematic diagram showing main components of a direct (top) and indirect (bottom) extrusion press.[2]

In direct extrusion, the ram forces the billet through the die and moves in the same direction as the extruded material. Therefore, friction is present along both the billet/die and billet/container interfaces. Indirect extrusion involves forcing the die in the opposite direction to that of the moving extrudate. Therefore, friction will only be present at the billet/die interface. The use of indirect versus direct extrusion method is dependent upon the desired features of the product. The advantages of indirect extrusion are mainly due to the reduced presence of friction in the billet: lower overall load, more uniform metal flow across the extrudate, less tendency for surface cracks to develop, and increased tooling life. Conversely, the disadvantages of indirect extrusion are that impurities and defects from the billet surface make their way to the extrudate surface more easily, resulting in the practice of machining or scalping the initial billet. Also, the area of the hollow ram limits the available cross sectional area and length of the extruded product.[3] Direct extrusion is capable of producing larger cross sectional products due to the increased press capacity.[4]

2.1.2 Metal Flow in Extrusion

The metal flow in the extrusion process is very complex as compared to other forming processes such as wire drawing and rolling due to the non – axisymmetric conditions and high strain. The metal flow is dictated by the temperature during extrusion, friction along the container and die, state of stress, and ram speed. The traditional method of determining flow patterns during extrusion is the visioplastic technique. This technique uses a billet, typically made from modeling material such as

plasticine, wax, or low melting temperature metals (e.g., lead and tin), cut in half along the length with grid marks placed on each half. The advantage of using these materials is that they mimic the flow behavior of metals such as aluminum at hot deformation temperatures. The billet is then extruded partially and split open once again to reveal the resultant flow pattern. The metal flow in direct versus indirect extrusion is markedly different as shown in Figure 2. [5]

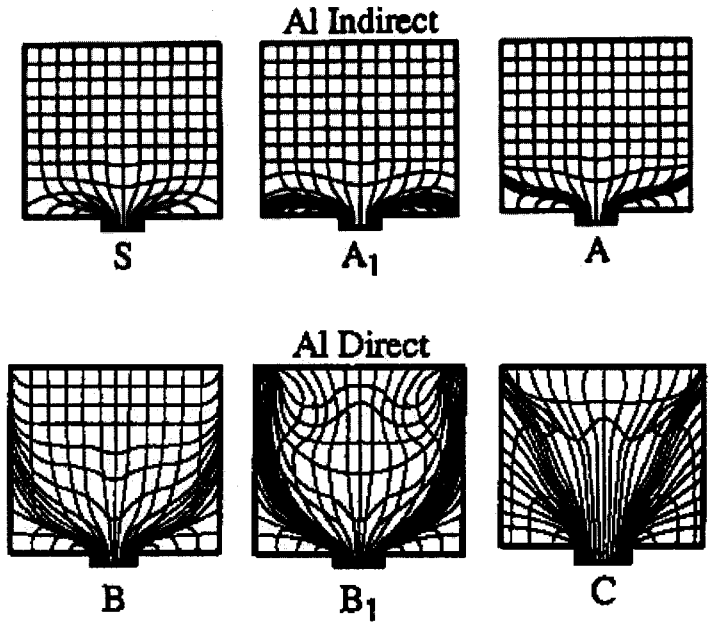

Figure 2: Examples of flow patterns created by direct and indirect extrusion of metals.[5]

Indirect extrusion is typically regarded as representing Type A_1 flow pattern shown in Figure 2. This is associated with no friction at the container wall and presence of a "Dead Metal Zone" (DMZ) that forms along the die face. Due to the lack of metal flow in this region, it is assumed that the deformation conditions are low. In the direct extrusion process, many different types of flow patterns are possible, as seen

in patterns S, A, B, and C. Type S flow pattern is associated with direct extrusion with considerable lubrication such as for steel and titanium extrusion where the lubricant forms a continuous film and separates the billet material from the container. Therefore, there is little friction at the container/ billet interface. Type A and B flow patterns represent direct extrusion of different materials representing various levels of flow stress at the deformation temperature. Type B flow pattern most closely resembles that of direct extrusion of aluminum and its alloys. In these flow patterns, a DMZ forms in the corners at the die end of the billet. This is a result of material being stagnant in the corner, unable to escape through the die orifice easily. A "shear intensive zone" forms along the interface between the DMZ and main deformation zone in the center of billet. This shear intensive zone undergoes a very high strain and strain rate.[6] Type B_1 and C flow are extreme conditions in direct extrusion with very large DMZ and large shear intensive zones. This is usually found in $\alpha + \beta$ brass extrusion, whereby there is very high friction at the container/billet interface combined with intense cooling at the surface leading to a higher flow stress in these locations of the billet.

It is known that the origin of the extrudate's surface comes from the metal flow pattern in the billet itself. Lefstad et al performed experiments whereby customized billets of an aluminum alloy retrofitted with strips of Al-Cu strips at evenly spaced positions perpendicular to the extrusion direction on the undeformed billet's surface.[7] The billets were then partially extruded on industrial indirect and direct extrusion presses with flat – faced dies. The results showed that the billet surface will make its way into the extruded product at different depths depending on the distance from the

die face. Figure 3 shows partially extruded billets from direct extrusion at two different levels of completion. It can be seen that the surface of the billet will flow into the extrudate in one of two ways: either along the DMZ or from behind the main deformation zone. In contrast, during indirect extrusion, in Figure 4 the billet surface markers from the front of the billet (marked 1, 2 and 3) make their way much sooner than markers from the back of the billet, 4 and 5. These first three markers travel along the DMZ at the face of the die into the extrudate surface.

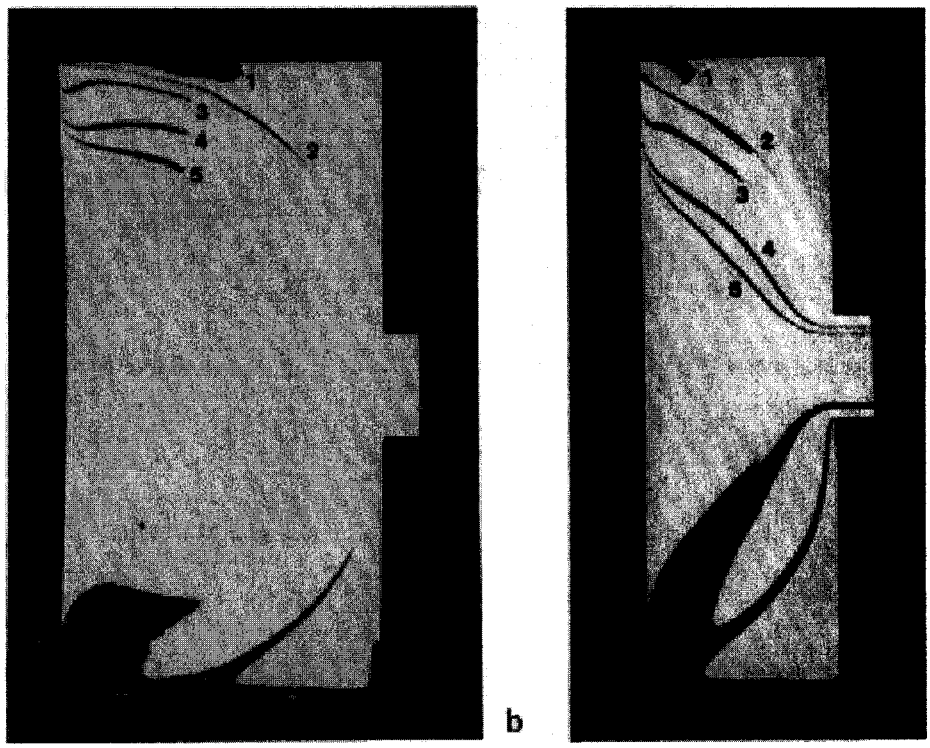

Figure 3: 6xxx aluminum alloy billet extruded via direct extrusion to 78 and 87% completion.[7]

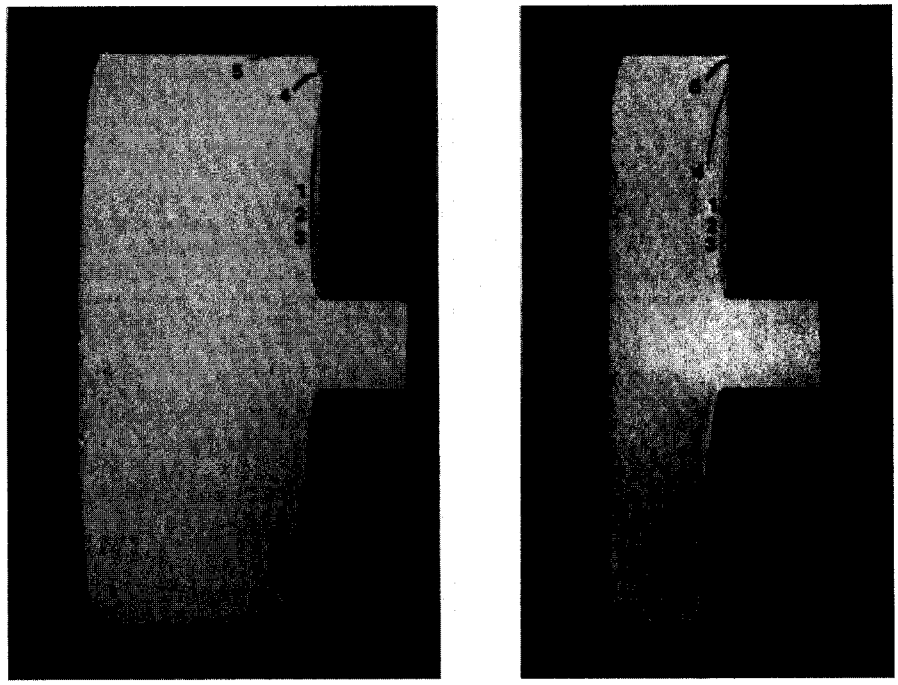

Figure 4: 6xxx aluminum alloy billet extruded via indirect extrusion to 83% (left) and 92% (right) completion.[7]

2.2 Deformation and Annealing Behavior

2.2.1 Stored Energy and the Deformed Structure

It is known that the characteristics of recrystallization are strongly dependent on the deformed state and prior plastic strain.[8] During thermo - mechanical processing at elevated temperatures there is a competition between hardening and softening in the material. Energy is being introduced through heat and deformation and causes dislocations to pile up or become entangled at second phase particles, grain and subgrain boundaries. The dislocation density increases and, therefore, so does the work hardening. Conversely, because of the high temperature of the process, these

dislocations may become free to move and annihilate each other, thereby softening the material. It is because of this competition between annihilation and generation of dislocations that aluminum alloys can exhibit steady state flow at large strains.[9] If the material is not able to annihilate the dislocations fast enough, then the driving force for recrystallization during deformation increases. This phenomenon of recrystallization of completely new grains during deformation is also known as dynamic recrystallization (DRX). A general equation for the minimum conditions to induce recrystallization dynamically is given by the following formula:[10]

$$\frac{\rho_m^{\,3}}{\dot{\varepsilon}} > \frac{2\gamma}{KL_dMGb^5} \qquad (1)$$

where:
ρ_m = dislocation density
$\dot{\varepsilon}$ = strain rate
γ = grain boundary energy
K = constant
L_d = mean slip distance of dislocations
M = boundary mobility
G = shear modulus
b = Burgers vector

For a given material, the right hand side of equation 1 is kept constant at a particular temperature. In materials with a low stacking fault energy, such as Cu, Ni, and γ Fe, the ability of dislocations to glide and cross – slip is limited.[11] Therefore, dislocations will build up faster in these materials during deformation. The driving force for these materials to dynamically recrystallize increases. When the stacking fault energy is high, for example in aluminum and α Fe, dislocations are very mobile

and can climb, glide, and cross – slip easily.[12] During hot deformation these materials will prefer to dynamically recover. This is because the dislocation density in equation 1 will never be high enough to overcome the value of the right hand side of the equation. This lack of a critical dislocation density is of interest here because, although aluminum alloys do not normally undergo DRX (because of their low hot worked dislocation densities), the nucleation and growth of new grains can indeed be induced in the presence of sufficient quantities of a hard second phase.[13] These appear to raise the local dislocation densities and lattice curvatures above the critical levels needed for the initiation and propagation of dynamically recrystallized grains. DRX has been observed in high purity aluminum and aluminum with high solute concentrations.[14,15] The high solute concentrations were found to restrict dislocation motion to the point where the dislocation density to an appreciable amount to induce DRX.

In Figure 5, true stress vs. true strain is plotted for a 0.68% carbon steel after tensile testing at various temperatures.[16] It can be seen that this material exhibits dynamic recrystallization as shown by the multi – peak stress oscillations, especially at higher temperatures. In Figure 6, an Al – Mg alloy is shown to exhibit extensive dynamic recovery at various strain rates exhibited by the flat curve at higher strains.[16]

In most industrial aluminum alloys, DRX is not likely to occur to the extent of low stacking fault energy materials. As a result, the subgrain coalescence mechanism associated with high stored energy nucleation is not likely to play a role. Instead,

dynamic recovery is the overriding mechanism for strain softening. Strain-induced boundary migration (SIBM) or some other low energy mechanism is of primary interest as it relates to the characteristics of the deformed structure.[17] SIBM involves a bulging of a high angle grain boundary into a region of high dislocation density, becoming a favorable site for nucleation.

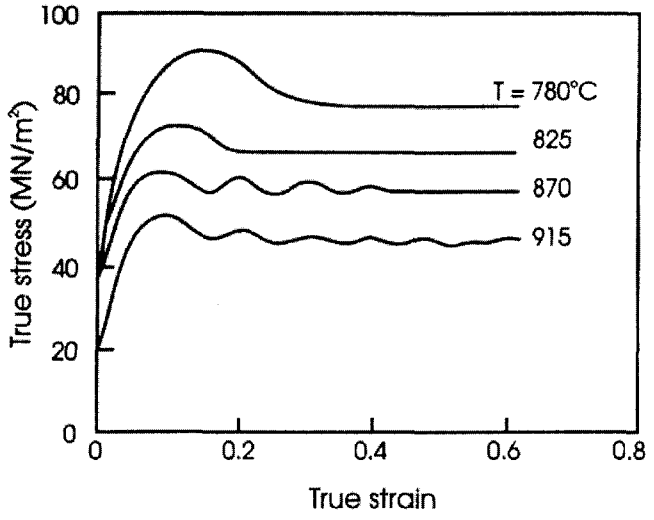

Figure 5: 0.68 % C steel at various temperatures depicting dynamic recrystallization.[16]

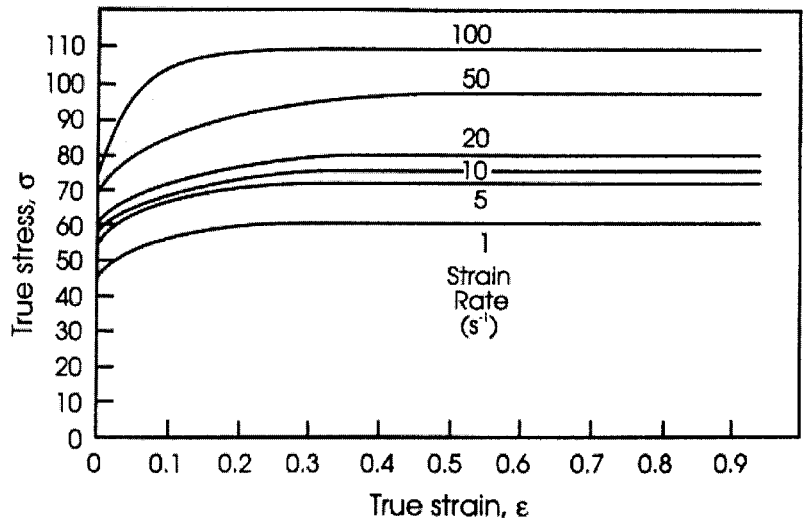

Figure 6: Al - 1% Mg alloy deformed at 400^{0}C at different strain rates exhibiting steady state flow and dynamic recovery.[16]

As mentioned earlier, the as – deformed structure plays a significant role in how the annealed microstructure will develop. The hot – deformed structure of aluminum alloys has been studied significantly in the literature and its evolution during deformation is summarized in Figure 7.

Typically, the progression of how an aluminum alloy microstructure evolves during hot deformation in rolling or extrusion is as follows. First, the starting microstructure is usually made up of equiaxed, crystallographically random oriented grains with a uniform average grain size (Figure 7A). While it is usually assumed that grains are equiaxed after homogenization, grains can exhibit unusual shapes, as has been studied in three-dimensional studies [18]. The material response to deformation conditions will depend in some part on the shape and size of these initial grains. The initial grain size will depend on the amount of grain refiner during casting as well as homogenization conditions. When the material starts to be deformed, the grains

undergo a shape change, which depends on the state of stress and strain conditions (Figure 7B). For example, a compressive state of stress would produce a flattened, pancake-shaped grain structure while a tensile state of stress would result in long, elongated grains in the tensile direction. During hot deformation of aluminum alloys, such as rolling or extrusion, the state of stress can become very complex and will vary in the billet and deformation zones. For example, in direct extrusion, the center of the extrudate typically experiences plain strain compression. At the periphery, however, there is a very high shear or tensile component, depending on the friction and extrusion ratio, as the material exits the die. To make the situation even more complex, the history of the material before it reaches the die must be taken into consideration. The state of stress may be a combination of compressive and shear/tensile.

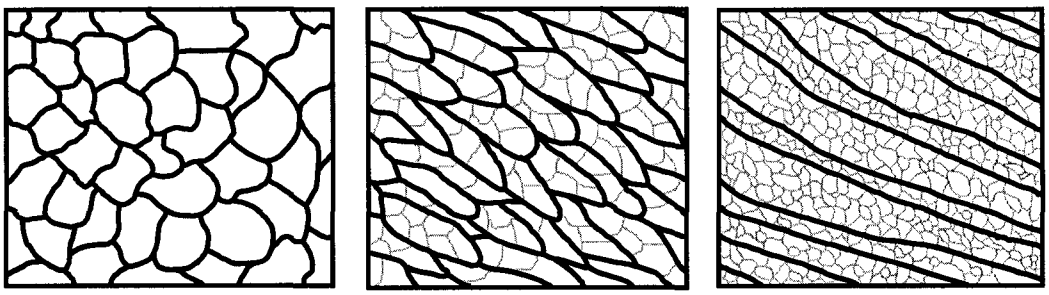

Figure 7: Schematic diagram showing the progression of a typical microstructure in hot deformation of an aluminum alloy. Dark lines represent high angle grain boundaries (>15°), while light gray lines represent low angle grain boundaries (<15°).

After steady state deformation, the grains will begin to develop low – angle subgrain boundaries of constant mean misorientation and size (Figure 7C). After

higher deformation in extrusion and rolling, the material resembles a "banded" or "fibrous" microstructure with high angle grain boundaries separating regions of different crystal orientation. This type of structure can be seen in Figure 8 for the case of a 2014 aluminum alloy hot rolled at 300°C to 50% reduction in a single pass. It is generally known that the deformation structure of a hot deformed material will never reach a true steady state regime during dynamic recovery. This is especially true at higher strains where grain boundaries develop a serrated structure, especially at high values of deformation temperature and low strain. For example, in Figure 8, notice that the grains boundaries are serrated, which is a typical indication of dynamic recovery. Within the banded microstructure, subgrains exist and remain equiaxed in shape. Eventually, the high angle grain boundaries will exhibit oscillations that are related to the subgrain size.

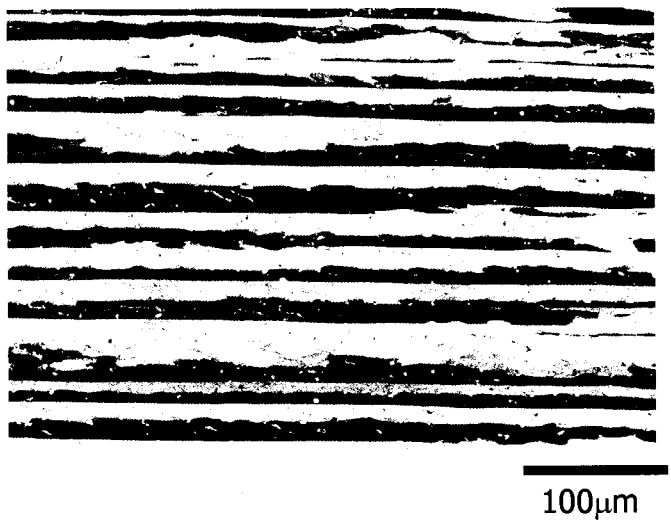

Figure 8: Hot rolled 2014 aluminum alloy showing banded microstructure and serrated grain boundaries. The material was rolled at 300°C to 50% reduction in a single pass.

The strain rate and deformation temperature are usually combined in the form of a Zener Holloman parameter (Z), where:

$$Z = \dot{\varepsilon} \exp\left(Q/R_G T_{def.}\right) \quad (2)$$

where:

Z = Zener Holloman parameter
$\dot{\varepsilon}$ = strain rate
Q = Activation energy (Al self diffusion)
R_G = Gas constant
$T_{def.}$ = Deformation temperature

The term temperature compensated strain rate is also used to define the parameter Z. The effect of the Zener Holloman parameter on the dislocation density, flow stress, and subgrain size of aluminum alloys has been studied heavily [10]

An expression relating these different values has been established as:

Flow Stress

$$Z = \dot{\varepsilon} \exp\left(Q/R_G T\right) A \sinh(\alpha\sigma)^n \quad (3)$$

where:
A, α, n, and R = constants
σ = Flow stress

Subgrain Size

$$\delta^{-m} = a + b' \ln Z \quad (4)$$

where:
a, b', m = constants
δ = subgrain size

A majority of the stored energy in a hot deformed material is in the form of line and planar defects (dislocations and grain boundaries). During hot deformation, point defects such as vacancies can be formed, but its contribution to the stored energy compared to dislocations is negligible. Therefore, in this research, more emphasis of quantifying stored energy will be on dislocations and grain boundaries. Grain boundary properties have been heavily studied in the literature, but many questions still remain as to their characteristics especially at high misorientation angles (>15°). The energy of grain boundaries has been computed and measured experimentally by Hasson and Goux [19]. It is known that the energy of a grain boundary increases with misorientation angle up to a value, usually assigned as 15° (Figure 9). Beyond this value, the grain boundary energy generally plateaus with the exception of coincidence site lattice points and twin boundaries.

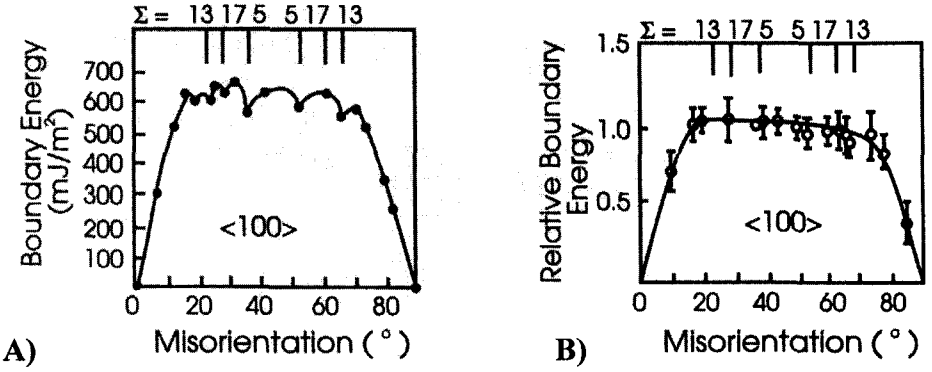

Figure 9: A) Calculated and B) Measured grain boundary energy as a function of misorientation angle for a <100> type boundary. [19]

For misorientations below 15°, a Read Shockley equation has been used to relate the energy at each misorientation [20]:

$$\gamma = \gamma_m \, {}^{\Theta_{avg.}}\!/_{\Theta_m} \left(1 - \ln {}^{\Theta_{avg.}}\!/_{\Theta_m}\right) \qquad (5)$$

where:
$\Theta_{avg.}$ = Average misorientation
Θ_m = Critical misorientation (15°)
γ_m = Critical boundary energy
γ = Grain boundary energy

The primary focus of quantifying stored energy in this research will be on grain boundary misorientation and grain size. There is a considerable effect of dislocations on stored energy, but will be addressed only in terms of average values based on constitutive equations. There are several ways to quantify stored energy in a deformed material. Traditional techniques include Differential Scanning Calorimetry (DSC), X-ray Broadening Techniques, and Transmission Electron Microscopy (TEM). DSC analysis is usually considered too diffuse and overlapping in order to get exact data for recovered and recrystallized structures. X-ray broadening techniques are limited to measuring the localized inhomogeneous lattice strain energy. Finally, traditional TEM allows one to locate and characterize individual dislocations. However, the process to quantify the dislocations in even a moderately deformed material would be a daunting task. Therefore, a new procedure, or context by which stored energy is quantified needs to be developed and implemented in order to predict recrystallization nucleation potential.

A general equation relating strain and stored energy in the terms of the density of dislocations has been made [10], whereby:

$$\varepsilon = \rho\, b\, L_d \tag{6}$$

where:
ε = true strain
ρ = dislocation density
b = Burgers vector
L_d = average distance of dislocation movement

The energy per unit volume, E_D, resolved from boundary misorientations can be approximated as:

$$E_D = \frac{3\gamma_0\Theta(A - \ln\Theta)}{\delta} \tag{7}$$

where:

δ = subgrain diameter
Θ = boundary misorientation angle

and

$$A = 1 + \ln\left(b/2\pi r_0\right) \tag{8}$$

where:

b = Burgers vector
r_0 = radius of the dislocation core (usually between b and 5b)

and

$$\gamma_0 = Gb/4\pi(1-\nu) \tag{9}$$

where:

G = shear modulus
ν = Poisson's ratio

While these relationships provide the basis for stored energy contributions from dislocations and grain boundaries, it still needs to be correlated to processing conditions.

Vatne, et al [21] have developed a formulation for the driving pressure necessary for recrystallization to occur in a high stacking fault material and the derivation is given below.

The average stored energy of a composite structure can be defined as:

$$P_D = \alpha \frac{\gamma_{SB}}{\delta} + \rho\Gamma \tag{10}$$

where:
α = geometric constant on the order of 3
γ_{SB} = average subgrain boundary energy
δ = average subgrain size after deformation
ρ = dislocation density within subgrains
Γ = dislocation line tension

The dislocation density during deformation can be associated with the subgrain size by:

$$\sqrt{\rho} = C_\rho \frac{1}{\delta} \tag{11}$$

where:
C_p = constant on the order of 5

The subgrain boundary energy can be approximated using the Read Schockley relationship as:

$$\gamma = \frac{Gb\Theta}{4\pi(1-\upsilon)} \ln\left(\frac{e\Theta_c}{\Theta}\right) \tag{12}$$

where:
Θ_c = critical misorientation for a high angle boundary (~15°)
ν = Poisson ratio (~0.33)

If Γ is equal to 0.5 Gb^2, then the stored energy P_D can be expressed as:

$$P_D = \frac{Gb}{\delta}\left[\frac{\alpha\Theta}{4\pi(1-\upsilon)}\ln\left(\frac{e\Theta_c}{\Theta}\right)+0.5C_\rho\frac{b}{\delta}\right] \quad (13)$$

Similar formulations have been used by others in the literature to determine stored energy after extrusion of 6xxx series aluminum alloys.[22,23]. Typically, values of the subgrain size, dislocation density and misorientation angle are measured or are based on relationships given in equation 3, 4, and 11.

2.2.2 Deformation and Annealing Textures in Aluminum Alloys

Several deformation textures exist in hot extrusion and rolling of aluminum alloys. Traditionally, these textures for extrusion have been reported as being a <111> and weaker <100> fiber texture.[24] However, this is the case for simple, round extruded profiles. Aluminum extrusions today consist of very complex shapes where different strain paths will produce local texture gradients. Perocheau and Driver [25] have recently summarized experimental deformation textures from Aukrust [26] and presented simulated textures after extrusion of a 6082 alloy from the center of an extrudate to the surface as can be seen in Figures 10 and 11. Rectangular billets with dimensions of 38×75×265 mm were used and were extruded to plates with dimensions 3.3 x 78.5 mm. It was found that at the center of the extrudate a β fiber exists and a TD (Transverse Direction) rotated copper component exists at the surface. The β fiber can be described as a continuous string of texture components in Orientation Distribution Space, which follows a path from {112}<111> (Cu component) through {123}<634>

(S component) to {110}<112> (Brass component).[27] The β fiber is shown schematically in Figure 12, where ϕ_1, Φ, and ϕ_2 represent the Euler angles that relate the crystallographic orientation to the sample orientation.[28] The maximum orientation component of the β fiber was found to be the S component at the center of the extrudate. In addition to extrusion, simulation of texture development in hot reversible rolling was performed. A pure shear texture {001}<110> was shown to occur at the surface of the rolled product. Typical hot rolling deformation textures are reported as having a β fiber with a maximum at the Brass orientation.[29] The cube texture {001}<100> is also reported as being present in low volume fractions after hot rolling and extrusion.[30]

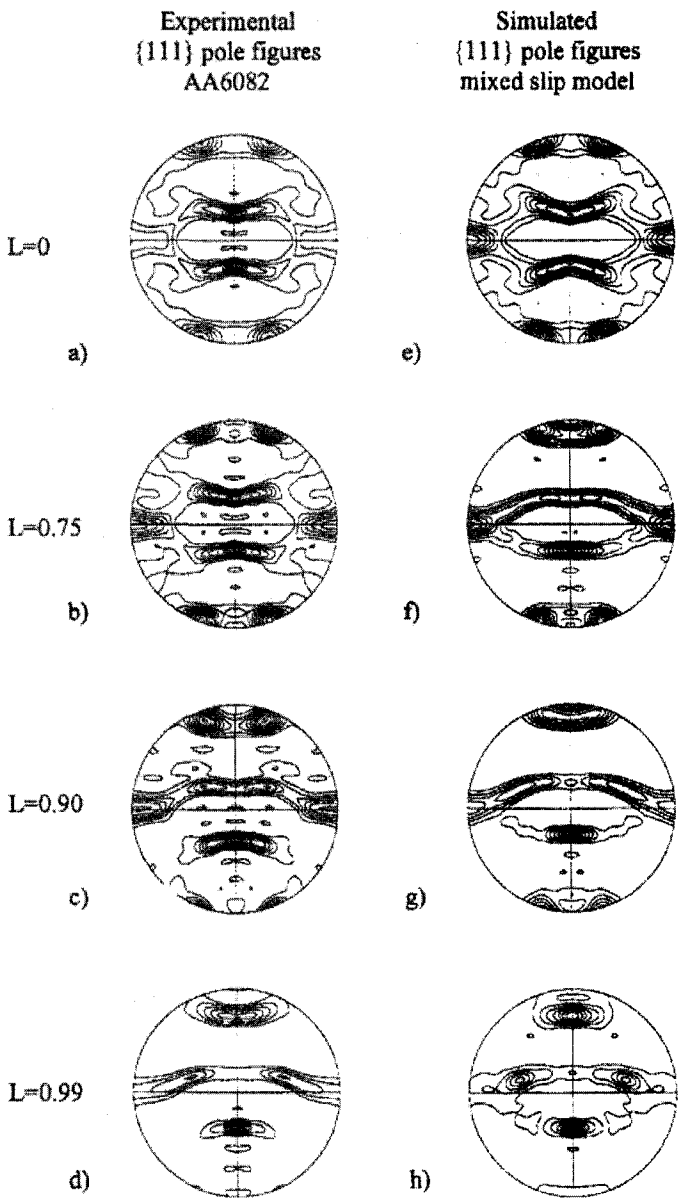

Figure 10: {111} pole figures of experimental (a-d) and simulated (e-h) textures in a 6082 aluminum extrusion. L = 0 represent the center of the extrusion and L = 0.99 represents the surface of the extrusion. (Simulation [24], Experimental [26])

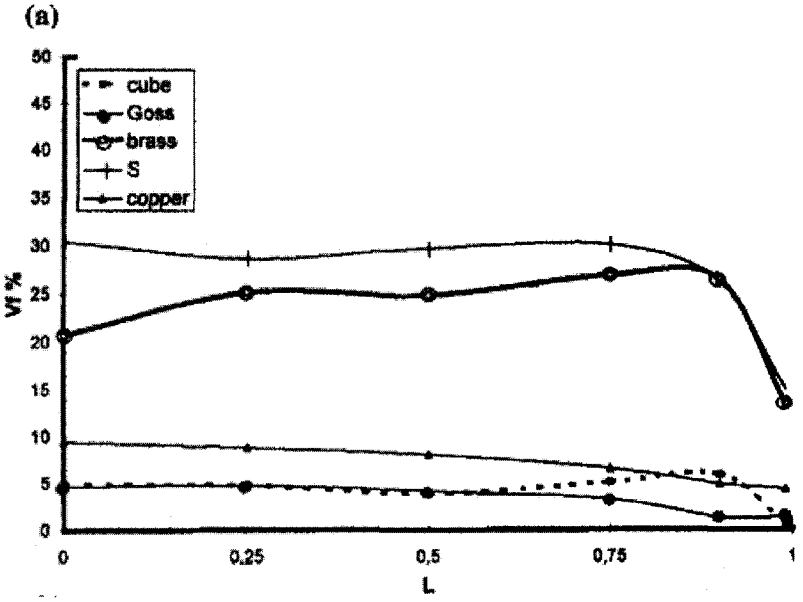

Figure 11: Plot of volume fraction of each texture component in experimental acquisition from the center of the extrudate, L=0, to the surface, L=1.[26]

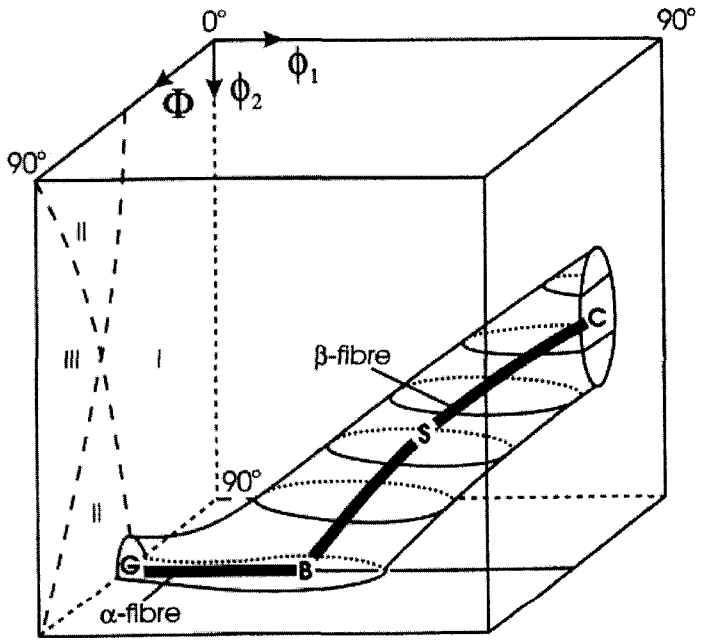

Figure 12: Representation of Orientation Distribution space showing position of the β fiber, where B (Brass, {110}<112>), S ({123}<634>), and C (copper, {112}<111>).[28]

2.2.3 Forms of Recrystallization

Upon annealing a material after deformation, the material is in a position to undergo structural changes and return to a state of lower energy. The stored energy, in the form of free dislocations and grain boundaries, is released due to high temperatures of annealing which promote thermal fluctuations and allow a recrystallized grain boundary to move.

2.2.3.1 Static and Dynamic Recrystallization

It is generally accepted that recrystallized grains do not 'nucleate' as totally new grains by the atom by atom construction assumed by thermodynamics.[31] Instead, these new grains grow from small regions, recovered subgrains or cells, that are already present in the deformed microstructure. The driving force for primary recrystallization is reduction in dislocation density. Static recrystallization involves recrystallization after cold or hot working. Static recrystallization growth kinetics have been modeled and usually follow the traditional Johnson - Mehl - Avrami Kolmogorov (JMAK) type relationship:

$$X_V = 1 - \exp\left[-A_1 t^n\right] \qquad (14)$$

where:

X_V = Volume fraction recrystallized
A_1 = constant based on nucleation and growth kinetics
t = time
n = geometry of the growth sites activated

The mechanism by which traditional dynamic recrystallization takes place has been previously discussed in section 2.2.1.

2.2.3.2 Continuous and Geometric Dynamic Recrystallization

The general process of Continuous Dynamic Recrystallization (cDRX) results in the progression of subgrain structures that evolve into high angle misorientation grains themselves during deformation. The mechanism by which cDRX occurs has been extensively debated in the literature.[32-35] The progression of cDRX grain formation can be seen in Figure 13 for the case of high purity aluminum deformed to relatively high strains of 16.3.[32] It should be noted that this phenomenon differs from traditional Dynamic Recrystallization (DRX) where new, dislocation – free grains are nucleated at prior high angle grain boundaries during deformation.

A similar form of recrystallization during deformation is known as Geometric Dynamic Recrystallization (gDRX). gDRX is essentially a subset of the phenomenon known as cDRX, whereby new grains do not undergo traditional nucleation and growth, but rather develop to accommodate to the geometry of the highly deformed grain. Several authors, most notably Humphreys and McQueen, have observed this phenomenon whereby equiaxed grains with high angle grain boundaries develop during deformation and are on the order of the subgrain size [34-35]. As deformation increases to large strains, grains become flattened and serrations develop at the high angle grain boundaries due to dynamic recovery. These serrations are similar to those

seen at the high angle grain boundaries for the case of hot rolled aluminum in Figure 8. As can be seen schematically in Figure 14, eventually, these serrations grow larger and begin to impinge on each other. When the high angle grain boundaries join, they form new, relatively equiaxed grains.

Humphreys [37] has developed a relationship that predicts a critical strain for gDRX formation, ε_c:

$$\varepsilon_c = \ln(Z^{1/m} D_o) + K \qquad (15)$$

where Z is the Zener Holloman parameter, D_0 is the original grain size, and K is a constant on the order of unity. An example of a gDRX microstructure formed from deformation in torsion is shown in Figure 15. [38]

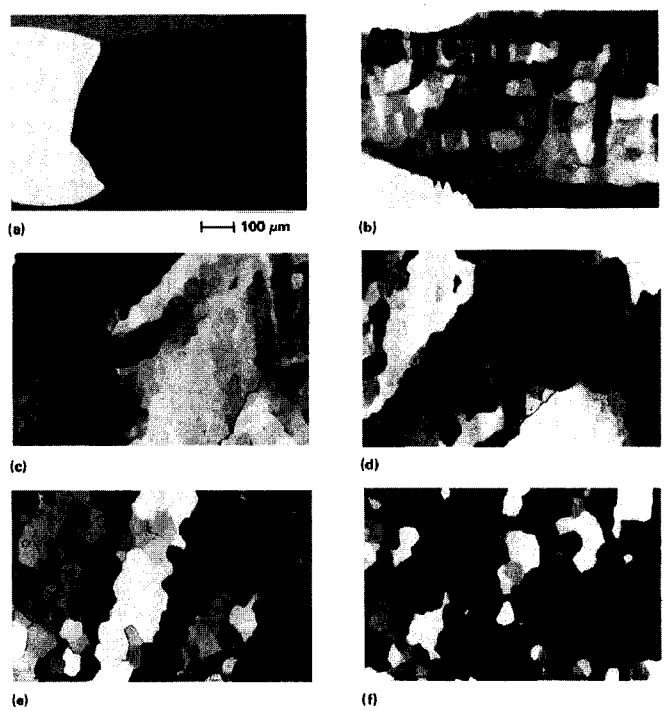

Figure 13: Microstructural evolution of high purity aluminum under compression with increasing strain, ε, a.) 0, b.) 0.2, c.) 0.6, d.)1.26, e.) 4.05, f.) 16.3. [32]

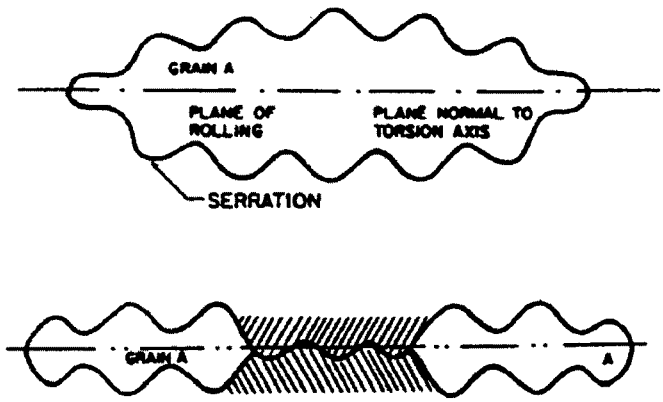

Figure 14: Schematic diagram showing the progression of how serrated grain will transform to new equiaxed grains after further deformation.[32]

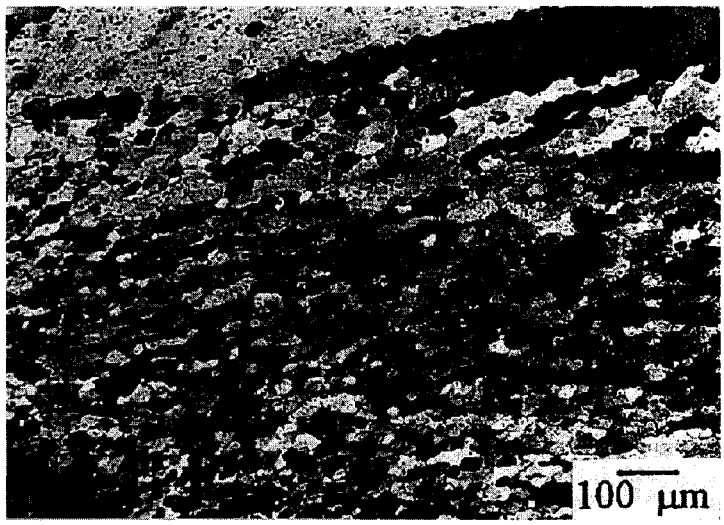

Figure 15: Example of a microstructure formed after Geometric Dynamic Recrystallization showing fine, relatively equiaxed grains. This microstructure is from an Al-Mg sample deformed in torsion to a strain of 40. [38]

The key to this type of structure appears to be extended recovery, whereby high angle boundaries migrate locally in response to boundary tensions of the substructure and local dislocation density variations. In aluminum alloys, the high stacking fault energy of the material allows for this extended recovery to take place.

2.2.4 Effects of Alloying Additions on Annealing Behavior

In this research, alloys of the 6xxx series were investigated due to their industrial significance. 6xxx series aluminum alloys contain Mg and Si as their primary alloying elements. In these alloys Mg and Si combine to form the precipitation hardening phase Mg_2Si. There are many variations of 6xxx series alloys used in industry depending on the desired properties and application. In this research, the focus is primarily on 6061 aluminum alloys. A typical breakdown of alloying elements and their limits for 6061 compared to other 6xxx series alloys are shown in Table I. Generally, Mg and Si levels are comparatively higher in 6061 with other 6xxx series alloys. Within the group of 6061 alloys, different manufacturers and aluminum processing companies will vary the chemistry within the acceptable limits in order to give a broader selection of properties as well as to control processing parameters.

Table I: Alloying additions and limits from Aluminum Association standards.[39]

Element	Si	Fe	Cu	Mn	Mg	Cr	Zn	Ti
Wt. %	0.40-0.80	0.7	0.15-0.40	0.15	0.8-1.2	0.04-0.35	0.25	0.15

Particles less than 1 μm in diameter

As mentioned earlier, Mg_2Si precipitates form readily in 6xxx series alloys as they comprise a majority of the hardening effect for the alloy. The effect of Mg_2Si precipitates on annealing behavior has not been widely studied, but in general, they are regarded as having a negligible effect on recrystallization. These precipitates can be

less than or greater than 1 μm in size and form as plates or rods in shape. Chromium and manganese are typically added to aluminum alloys to increase recrystallization resistance.[40] The mechanisms by which these elements manifest themselves is either by forming Cr or Mn containing dispersoids that induce the phenomena of Zener pinning or increase solute drag. These dispersoids may form as Al(Cr,Mn)Si and range in size from 0.1 to 1 μm.[41,42] Recently, research has shown that Cr and Mn dispersoids are formed from other phases ("μ" phase), which are hexagonal and semicoherent with the Al matrix and nucleate on β' Mg_2Si precipitates.[43] Additionally, it was found that at a Cr content of 0.3 wt.% or higher, the Cr dispersoids form either as α – Al(FeCr)Si or α' – AlCrSi. When the Cr content is below 0.15 wt.%, the Cr containing dispersoids only will form as α – Al(FeCr)Si. The difference between α – Al(FeCr)Si and α' – AlCrSi dispersoids is in the lattice parameter, 1.25 nm and 1.09, respectively. The phenomenon by which these dispersoids act is Zener pinning, which retards the movement of a boundary. The drag pressure, P_Z, imposed by these particles on moving boundaries is given by [44,45]:

$$P_Z = \frac{3F_V\gamma}{d} \qquad (16)$$

where:

γ = grain boundary energy

F_v = volume fraction of particles

d = average particle diameter

Particles greater than 1 μm in diameter

The majority of particles greater than 1 μm in diameter is the insoluble iron containing phases such as AlFeSi and AlFe. These second phase particles usually form during casting at the grain boundary as plates and needles. Upon homogenization, these particles become rounded and may form spheres or a "Chinese script" morphology. Upon deformation, the particles will become aligned in the rolling or extrusion direction and usually stay at the grain boundaries. It is generally known that particles greater than 1 μm in diameter form as nucleation sites for new statically recrystallized grains. This phenomenon is known as Particle Stimulated Nucleation (PSN).[46] During hot deformation, dislocations build up at the interface of these non – deformable particles, thereby leading to a high dislocation density gradient with the surrounding matrix. Upon annealing, new recrystallized grains will prefer to nucleate at these larger particles.

Humphreys and Kalu have determined a formula for the critical particle diameter to become a nucleus for a new recrystallized grain [47]:

$$D_f = (K_1 / TZ)^{1/2} \qquad (17)$$

where:
K_1 = constant equal to 1712 $m^2s^{-1}K$ for aluminum alloys
T = annealing temperature
Z = Zener Holloman parameter

Particle Stimulated nucleation has been found to lead to a predominantly random recrystallization texture. In contrast, traditional recrystallization textures usually form

as a result of one orientation being preferred over another in terms of nucleation and growth. During PSN, the growth of the recrystallizing grain is not dependent on texture, but rather the high dislocation density gradient between the particle and the surrounding material.

2.3 Formation of Extrusion Surface Imperfections

2.3.1 Summary of PCG Structure

As mentioned earlier, the focus of this research has been to determine the origin of a particular surface imperfection, the Peripheral Coarse Grain (PCG) structure, in aluminum extrusion. This PCG structure can manifest itself in both indirect and direct extrusion under certain processing conditions. The structure is characterized as large, relatively equiaxed grains at the surface of an extrudate and extending into the subsurface of the product, sometimes even consuming the entire extrudate in extreme cases. In general, the PCG structure can be controlled by several factors: controlling the exit temperature, increasing or decreasing recrystallization inhibiting elements, and maximizing the extrusion ratio to obtain a critical strain.[48] While these factors may help in short term solutions, a comprehensive understanding and prediction of PCG formation has yet to be made. Previous investigations have attempted to understand and predict PCG formation.[49-51] Many times, PCG formation is attributed to the strain gradient inherent in the extrusion process. In general, it can be assumed that the strain, strain rate, and deformation temperature of the material increases from the center of the extrudate to the surface (Figure 16). At some critical point, a PCG structure develops.

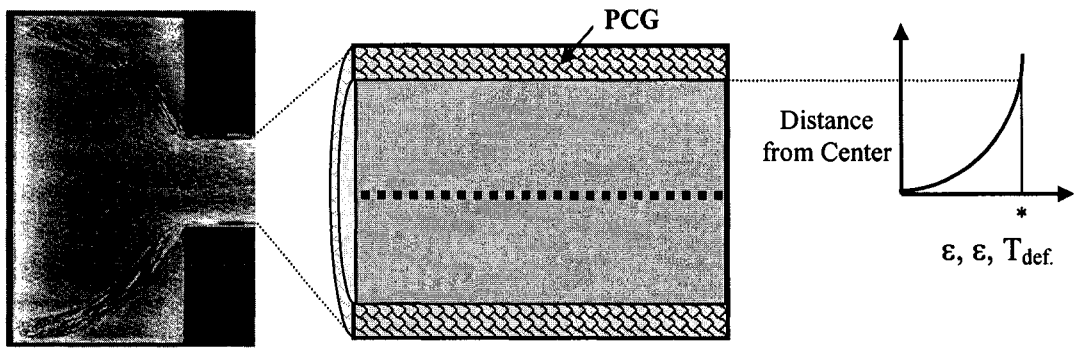

Figure 16: Schematic diagram of a PCG structure displaying a critical strain, strain rate, and temperature of the material whereby a PCG structure forms.

The die design has been known to affect the characteristics of the PCG structure due to its effect on metal flow [52]. For example, if more than one orifice is used in a die, the PCG structure may be skewed when viewed longitudinally, as can be seen in Figure 17. Also, it has been found that the depth of the PCG structure generally increases from the front to the end of the extrudate. This can be seen in a sequence of cross – sectional microstructures from the front, middle, and end of an extrudate (Figure 18).

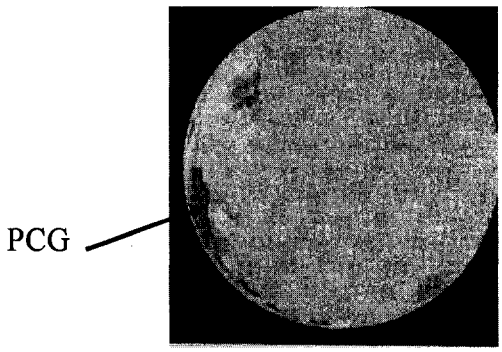

Figure 17: Crescent shaped PCG from an multi – orifice die.[52]

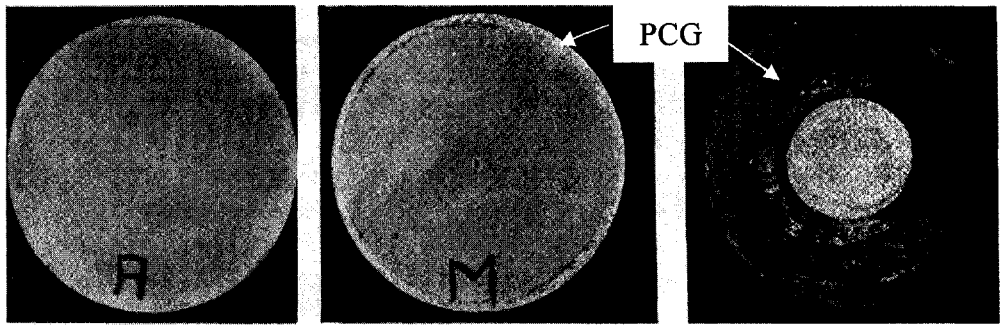

Figure 18: Cross – section of aluminum extrudates at different lengths of the extrudate, A – Front, M – Middle, and E – End of the extrudate. The depth of the PCG increases from none at the front to a considerable depth at the end of the extrudate.[52]

Furu, et al performed small – scale extrusion experiments on a 6082 aluminum alloy with very rapid quenching conditions and extrusion ratio of 40 [49]. The result was an extrudate with no noticeable Peripheral Coarse Grain structure. The structure of the extrudate was characterized by Light Optical Microscopy, Electron Backscatter Diffraction and Transmission Electron Microscopy. It was found in these studies that the texture of the material changed from a β fiber at the center to asymmetrical non – β fiber components at the surface. Additionally, the subgrain size was measured at four positions from the center to the surface and was found to decrease considerably at the surface. The subgrain size and misorientation and different positions in the extrudate are summarized in Table II.

Table II: Summary of subgrain size and misorientation from each position in extrusion experiments [49]

Position (Fraction of radius)	Subgrain Misorientation (° misorientation)	Subgrain Size (μm)
0.95	7.2	1.5
0.85	6.0	2.4
0.5	6.6	2.6
0	6.7	3.0

Zasadzinski et al [50] and Yang et al [51] studied the strain gradient that is present in simple extruded shapes. Zasadzinski performed small – scale extrusion experiments on a 2014 aluminum alloy with an extrusion ratio of 9. It was determined that the maximum strain at the surface was 25.2 and the maximum strain gradient $d\varepsilon/dr$ was 10.8. Yang produced an equation that predicts the effective strain at the surface of an extrudate given different die cone angles. For a die angle of 90°, it was predicted that an effective strain gradient of 1.9 would exist at the surface of the extrudate irrespective of the extrusion ratio. Since a higher strain exists at the surface of an extrudate, it has been accepted that this is the general cause of conditions for a coarse grain recrystallized region are favored. In general, it is known that the strain, strain rate and temperature of deformation increase from the center to the surface of a round extrudate. Also, it is generally known that the PCG structure forms at the surface and its depth generally increases from the front to the back of the extrudate. Despite investigations into the cause and control of the PCG structure there is still is not a good understanding of the mechanism by which this structure occurs. In order to form a predictive context whereby the depth of the PCG structure can be quantified, a direct link between processing parameters (ram speed, exit temperature, extrusion ratio, and chemistry) and PCG depth needs to be made.

2.3.2 Status of Surface Imperfection Prediction Capabilities

There has been an effort in the literature to model and predict the depth of the Peripheral Coarse Grain (PCG) structure. Most attempts to predict the PCG depth in aluminum alloys have been based on the Zener Holloman parameter, Z (as discussed in

Section 2.2.1). In Table III, a list of material characteristics at different states can be seen. On the continuum level, only very general knowledge is known about the deformation characteristics of an aluminum alloy. For example, the stress state, strain, deformation temperature, and strain rate can be predicted based on constitutive flow equations from physical simulation. The most promising and practical tool to predict microstructural evolution at the surface of extrusion seems to be computer modeling. Unfortunately, in the current state of commercially available numerical modeling packages, the role of microstructure is not usually taken into account. For example, on the meso and micro – scale, the material characteristics as listed in Table III are usually generalized or ignored completely.

Table III: Material properties and process parameters relating to the stored energy of a material.

Continuum	**Meso-scale**	**Micro/ Nano Scale**
Strain	Texture (Recrystallized and Deformed)	Second Phase Particles
State of Stress	Average Dislocation Density	Localized Dislocation Density
Strain Rate	Grain Size	Grain Boundary Properties
Deformation Temperature		Subgrain size

In this research, an emphasis will be put on the microstructural features on the micro and meso scale that contribute to the stored energy of aluminum alloy extrudates. This focus will form the basis of the predictive capability that is lacking in numerical modeling efforts.

3.0 STATEMENT OF PURPOSE

The objective of this research is to understand the origin and metallurgical nature of the specific surface imperfection known as a Peripheral Coarse Grain (PCG) structure in extrusion of 6xxx series aluminum alloys. The PCG structure represents a deleterious imperfection that needs to be fully understood in order to prevent its occurrence. A reduction in the presence of the PCG structure will lead to energy and economic benefits as well as an improvement in the mechanical performance and aesthetics of the extruded product.

As was shown in Section 2.0, most research involving the investigation and prediction of surface imperfections such as the PCG structure have focused on the metal flow and variation in strain, strain rate and temperature in the extrudate. Rarely is the metallurgical structure of the as – deformed extrudate surface investigated and correlated with the deformation parameters. Since the PCG structure is likely made up of recrystallized grains, the deformed structure prior to the onset of recrystallization needs to be characterized comprehensively.

In this research, physical simulation experiments are performed in order to correlate the processing parameters with the deformed and annealed microstructure. Since the phenomenon of recrystallization is based on the amount of stored energy in the material, the stored energy in the material after deformation ceases must be fully characterized and quantified. The stored energy approach in this research will form the basis of a predictive context of how coarse, recrystallized grain formation occurs. The

deformed structure that contributes to the stored energy can be characterized on many scales. As identified in the previous section, most research investigating the stored energy have focused on the continuum and nano - scale levels. The deformed structure will be characterized here on the meso – scale, which includes grain morphology and size, boundary misorientation, and microtexture.

4.0 EXPERIMENTAL PROCEDURE

4.1 Material

6061 aluminum alloy material used for these experiments was provided by Alcoa Technical Center with a chemistry resembling those of the Aluminum Association's standards for this alloy. In order to understand the effect of chemistry on recrystallized depth, two alloys representing Cr:Mn ratios of 1:1 (Low Cr) and 2:1 (High Cr) were used. Total Cr + Mn levels in wt. % were as follows: 0.17 (low Cr), and 0.35 (high Cr). Direct Chill (DC) cast billets were homogenized in a laboratory furnace for 3 hours at 555°C and cooled to room temperature at a cooling rate of 16.8°C/hr. Samples used for small-scale extrusion were sectioned from the mid-radius of the homogenized industrial billets. The mid – radius of a cast billet represents an area where a constant average grain size can be found. The shell zone, or inverse segregation zone, found at the periphery of the cast billet usually has a depth that is 5% of the billet diameter. This shell zone is characterized as showing macrosegregation and a non – uniform chemistry. By machining in the mid – radius of the billet, the shell zone is avoided. A schematic diagram showing the placement of small – scale extrusion billets, samples for hot rolling, and hot compression tests (not used in this research), can be seen in Figure 19.

Alcoa Engineered Products in Cressona, PA supplied 6061 aluminum alloy material used for hot torsion experiments. The material was delivered in the as – homogenized condition. The actual homogenization procedure is considered proprietary and was not available for disclosure.

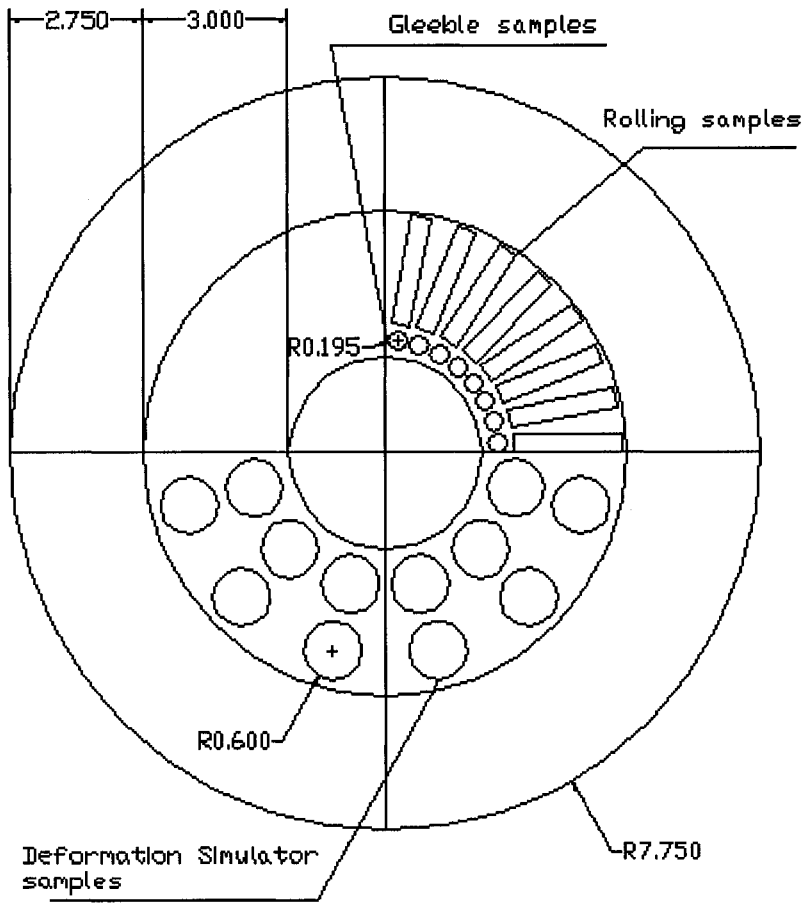

Figure 19: Schematic diagram showing sectioning procedure for samples used in hot rolling and small – scale extrusion experiments. (All dimensions are in inches)

4.2 Small – Scale Extrusion

The material for small – scale extrusion was machined to cylindrical billets with dimensions of 3.81 cm in height and 3.05 cm in diameter. The billets were indirectly extruded on a servo – hydraulic press to a round profile using conditions shown in Table IV. The press, located at Alcoa's Technical Center, is a 39-ton press and is

computer controlled. The billet and container are preheated before extrusion using a clamshell type infrared furnace via quartz tubes with 3 zones of heating capability. The billet and container were brought to the extrusion temperature in less than three minutes, and a hold time of 300 seconds was used. This was to ensure a more uniform temperature of the tooling and aluminum billet. The billets were crushed before extrusion began, which mimics the upsetting processes in extrusion. The crush speed used for these tests was 0.1 mm/s. Indirect extrusion was used to minimize friction between the billet and container interface. Therefore, a majority of the deformation is concentrated at the die exit. The extrudates were cooled using a forced air quench. The partially extruded billets were left in the extrusion container for approximately 60 seconds before they were removed and quenched in water. Temperature data from the test was collected from a thermocouple that was placed inside the die just at the die exit. Therefore, the data may be slightly skewed towards the temperature of the steel die rather than the extruding material. The die material was a H13 steel, a typical die material in extrusion. The bearing length of the die was 0.7mm.

Table IV: Sample designations and testing parameters used in small – scale extrusion tests.

Sample	Alloy	Extrusion Ratio	Starting Billet Temperature°C	Ram Speed mm/s
774	Low Cr 6061	20	400	1.3
775	High Cr 6061	20	400	2.6
776	Low Cr 6061	20	400	2.6
778	Low Cr 6061	40	400	1.3
780	Low Cr 6061	40	400	2.6
781	High Cr 6061	20	482	1.3
782	Low Cr 6061	20	482	1.3
783	High Cr 6061	20	482	2.6
784	Low Cr 6061	20	482	2.6
785	High Cr 6061	40	482	1.3
788	High Cr 6061	20	400	1.3
791	High Cr 6061	40	400	1.3
792	High Cr 6061	40	400	2.6
794	High Cr 6061	40	482	2.6
795	Low Cr 6061	40	482	2.6
796	Low Cr 6061	40	482	1.3

4.3 Industrial – Scale Extrusion

Industrial – scale extrusion experiments were performed at Alcoa Engineered Products in Cressona, PA. The purpose of these tests was twofold: first, to understand the effect of the shell zone on the depth of the Peripheral Coarse Grain (PCG) structure, and second, to compare results with those of small – scale extrusion experiments. Extrusion trials were performed on two direct extrusion presses, one with an 8 inch diameter container, and one with a 12 inch diameter container. Billets of the same

chemistry as the small – scale extrusion billets were used and the extrusion ratio was kept constant at 20. The round to round industrial extrusion experiments are summarized in Table V. Each extrudate was air cooled and then dropped in a water bath approximately 2 minutes after the back-end of each extrudate exited the die.

Two types of billets were used in these experiments in order to understand the effect of the shell zone on the depth of the Peripheral Coarse Grain (PCG) structure. Traditionally DC Cast and homogenized 12 inch billets were used, half of which were further machined to 8 inch diameter. The purpose of machining the billets was to remove the shell zone. These billets were machined at Flurer Machine and Tool Co. in Nazareth, PA.

Table V: Industrial – scale extrusion conditions.

Alloy	Billet Diameter	Extrusion ratio
Low Cr 6061	8" and 12"	20
High Cr 6061	8" and 12"	20

4.4 Hot Torsion

Hot torsion testing was performed at Dynamic Systems, Inc. in Poestenkill, NY under the supervision of the author. Dynamic Systems, Inc. manufactures specialized physical simulation equipment known as a Gleeble. The Gleeble testing machines are unique in that they use resistive heating rather than traditional convective or inductive heating to bring the sample to the testing temperature. Very high current flows and heats the sample through resistance. This technique allows for very rapid heating and

cooling as well as very precise temperature control.

To control the heating and cooling rate, the Gleeble automatically adjusts the current input based on the program temperature and thermocouple reading at the center of the sample. In hot torsion testing, many sample geometries can be used. For the purposes of this testing, the samples were machined as round solid specimens with a reduced radius gauge length. Initially, hollow samples were used for testing, but the given material's mechanical properties were too low to be deformed to such large strains. Therefore, solid bars were used instead. A schematic diagram of the sample dimensions is shown in Figure 20. The advantage of hollow samples for hot torsion testing is that the strain is relatively uniform across the sample radius. The solid samples used have a much larger gradient of deformation from low at the center to a maximum at the surface. In addition to sample geometry selection, the chosen testing setup can vary the deformed behavior considerably. In this testing setup, one side of the bar was constrained, while the other side was free to rotate. In Figure 21, the testing setup for these experiments is shown. The temperature gradient along the gauge length was measured by two thermocouples during the soak period and was of a negligible value. The heating rate used in all hot torsion testing was 5°C / s. The left hand jaws were radially constrained while the right hand side was free to rotate. Additionally, the jaws were not axially constrained, and therefore, the jaws were free to contract as the sample was twisting. A negligible tensile load was therefore recorded due to the force of the sample on the jaws. The torsion conditions used are shown in Table VI. The value of the Zener Hollomon was calculated using equation 2 and a

calculated Q value of 155,880 J/mol-°K. In order to test samples and characterize the deformed structure, very high quenching rates were needed. For this set of tests, a water quench spray head system was employed. After initial trials, it was found that the quenching system allowed for the sample to be quenched to below 100°C within less than 1 second of the end of twisting as can be seen in Figure 22. Therefore, the cooling rate after deformation was at least 380°C/s. The Gleeble equipment used in these experiments has a maximum motor speed of 1500 rpm. With 6.28 radians per revolution, this gives 9420 radians per minute or 157 radians per second. The shear strain was calculated using the following formula:

$$ShearStrain = \left(\frac{\phi * r}{L}\right) \tag{18}$$

where:

ϕ = rotation in radians
r = Radius of the reduced gauge section
L – Gauge length

In terms of effective strain:

$$EffectiveStrain = \frac{ShearStrain}{\sqrt{3}} \tag{19}$$

This can be worked backwards to develop a ratio of specimen radius to gauge length for a desired strain rate. For example, to program an effective strain of 10:

$$ShearStrain = 17.32\left(10 * \sqrt{3}\right)$$

and the resultant amount of twisting will then be: $\phi = \left(\frac{17.32 * 15}{5}\right) = 51.96 radians$

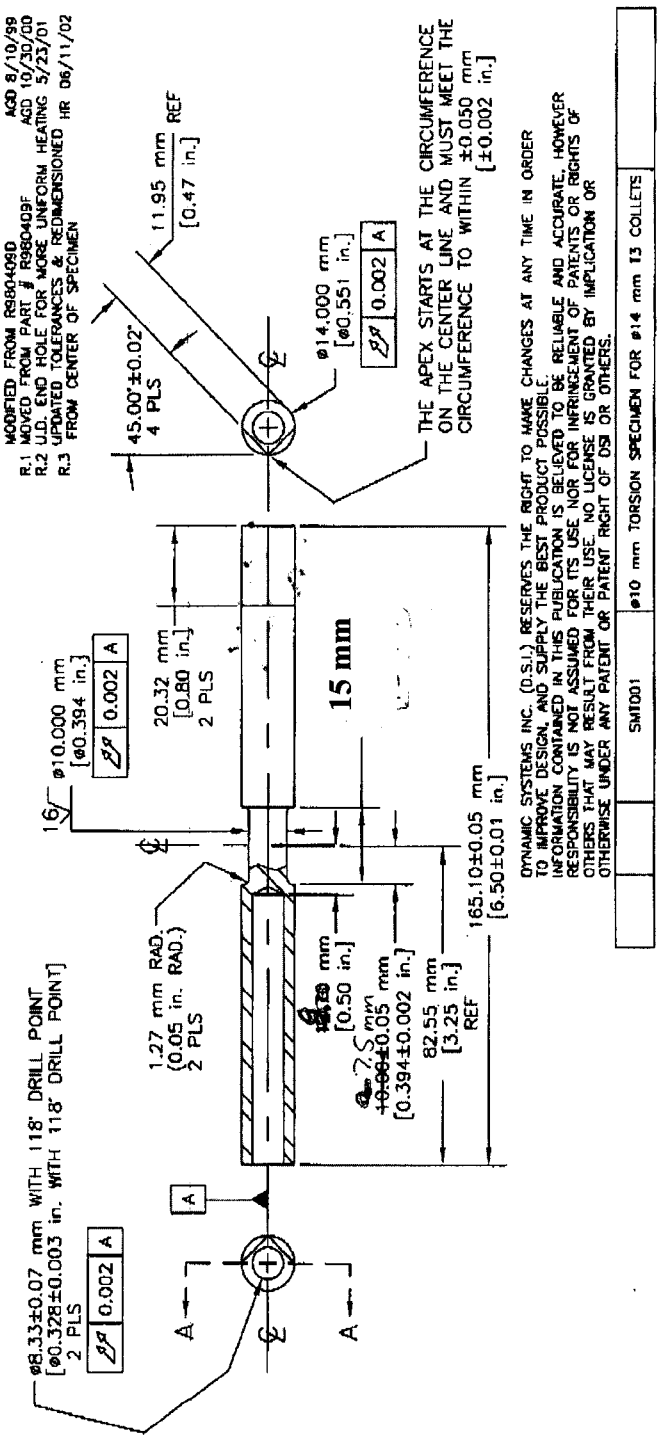

Figure 20: Dimensions of solid hot torsion samples used for testing.

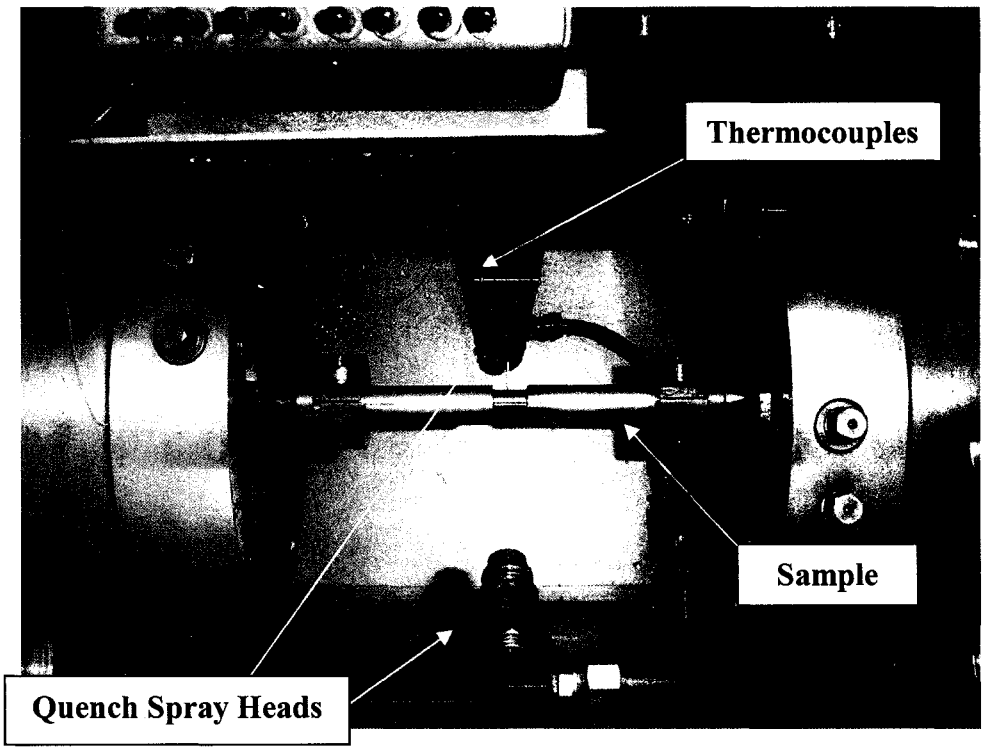

Figure 21: Photo of hot torsion testing setup.

Table VI: Sample conditions used in hot torsion testing.

Alloy	Deformation Temperature (°C)	Effective Strain	Strain rate (s^{-1})	Zener Hollomon Parameter, Z (s^{-1})
6061 Low Cr	400	1, 2.5, and 3.5	15	2.0×10^{13}
6061 Low Cr	400	1, 2.5, and 3.5	30	4.0×10^{13}
6061 Low Cr	482	1, 2.5, and 3.5	15	9.7×10^{11}
6061 Low Cr	482	1, 2.5, and 3.5	30	1.9×10^{12}
6061 High Cr	400	1 and 2.5	15	2.0×10^{13}
6061 High Cr	400	1 and 2.5	30	4.0×10^{13}
6061 High Cr	482	1 and 2.5	15	9.7×10^{11}
6061 High Cr	482	1 and 2.5	30	1.9×10^{12}

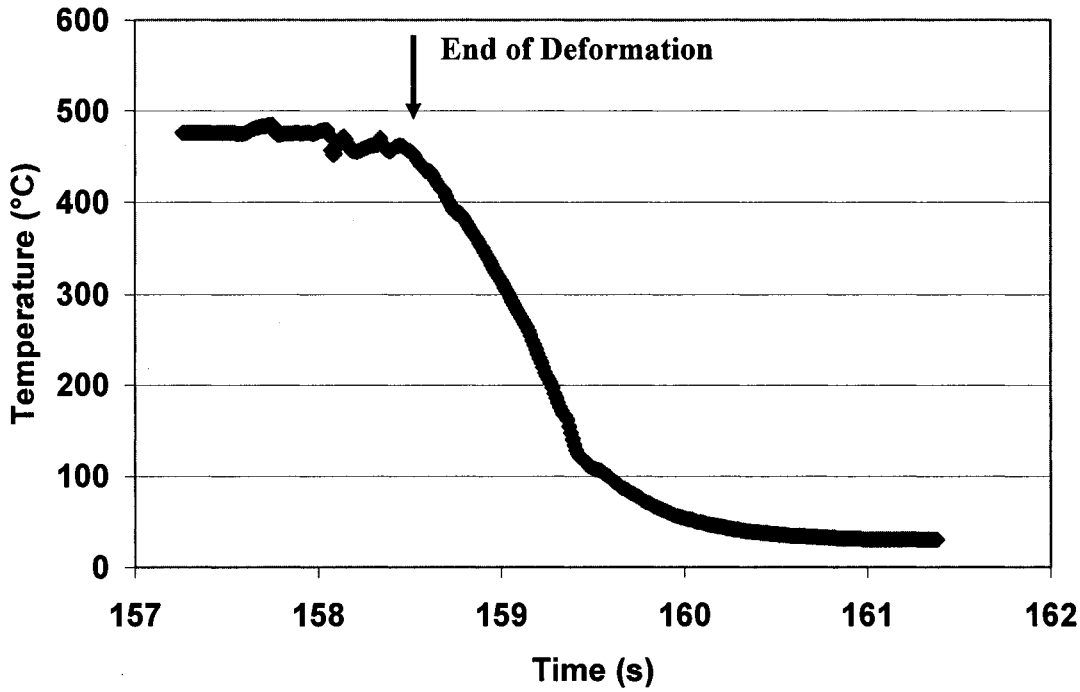

Figure 22: Temperature vs. time during torsion and subsequent water quenching. Notice that the temperature of the sample reached less than 100°C within 1 s after deformation ends.

4.5 Annealing Experiments

Samples from the small –scale extrusion experiments were annealed to investigate their annealing behavior at very short times. Samples were taken from each of the conditions listed in the results section for annealing experiments and annealed in a salt bath for 3, 6, and 9 seconds at 489° C using Liquid Heat 168 salt. However, first the heating profile of the samples had to be determined. A dummy sample with a thermocouple punched into it and attached to a temperature strip were used to simulate the annealing of a sample and determine the heating profile. At a pot temperature of 489° C the sample reached a temperature of 460° C in ten seconds and 350° C in three

seconds before being water quenched back to a temperature of 23° C. All samples from these annealing experiments were characterized using traditionally metallography and electroetching techniques described in Section 4.6.1.

4.6 Metallography and Microscopy

Samples from all physical simulation experiments were prepared for metallography. Additionally, samples from small – scale extrusion experiments were prepared for Electron Backscatter Diffraction (EBSD) characterization.

4.6.1 Light Optical Microscopy

Metallographic samples were prepared using traditional grinding and polishing techniques and were polished to a colloidal 0.5 μm SiO_2 finish. Samples used for metallographic analysis were electrolytically etched using a modified Barker's reagent at 30V for 5 minutes with an Al cathode. The modified Barker's reagent contained 217 mL of distilled H_2O, 7.5 mL of HBF_4, and 75 mL of Hydrogen Peroxide. Micrographs were taken on an Olympus BH2 using polarized light. A Nikon digital camera was interfaced with the Olympus microscope to take photographs of the microstructure. Digital photography equipment has gained popularity in recent years and its quality vs. cut film is still being debated. For the purposes of this investigation, it was decided that digital photography of microstructures produced a high enough quality image to perform qualitative comparisons. Additionally, for the most part, a procedure of producing collage images made up of several photographs was used. This enabled a

larger area of the extrusion discard or extrudate to be compared for analysis. Recrystallized depths for each extrudate were taken from half - length of the extrudate and measured using a LECO IA – 3001 Image Analysis system.

4.6.2 Scanning Electron Microscopy (SEM) and Electron Backscatter Diffraction (EBSD) Technique

Homogenized samples of the 6061 material were mounted and polished for chemical analysis in a JOEL 6300 Scanning Electron Microscope (SEM). An EDAX Energy Dispersive Spectroscopy system interfaced with the SEM equipment was used for X-ray chemical analysis of the Cr and Mn containing dispersoids.

Samples from small – scale extrusion experiments were taken for EBSD characterization. EBSD was performed using an EDAX/TSL Digiview Camera interfaced with a Philips XL-30 Environmental SEM. The SEM was equipped with a tungsten filament. The samples used for analysis were taken from the half – length of the extrudate as well as the extrusion discard, the remaining material after extrusion ceases. The discard represents roughly 25% of the original billet material.

Samples used for EBSD analysis were ground and polished to a colloidal 0.5 μm SiO_2 finish. The final polish is very important in order to minimize the deformation induced from sample preparation. In order to further minimize surface effects from mechanical preparation and to eliminate a relatively thick aluminum oxide at the surface, all samples were chemically polished within minutes before EBSD analysis. The chemical polish solution used was comprised of: 70% (H_3PO_4)

Phosphoric Acid, 25% (H_2SO_4) Sulfuric Acid, and 5% (HNO_3) Nitric Acid . The solution was heated to 85°C and the samples were dipped in the solution for approximately 20s. After polishing, the second phase intermetallics are left lying on the surface of the sample. Special care was taken to replicate this procedure for each sample of EBSD analysis. The importance of this repeatability will prove important when EBSD data is represented.

In order to quantify the grain and subgrain boundary misorientation and size, maps were taken from the center to the surface of the extrudates used in the analysis. From the sixteen extrudates that were analyzed using LOM, seven extrudates were used in EBSD analysis. The small – scale extrusion parameters of the extrudates used are shown in Table VII.

Table VII: Sample designations and small – scale extrusion conditions that were used for EBSD gradient analysis.

Sample	Extrusion ratio	Starting Temp. (°C)	Alloy	Ram Speed (mm/s)
EXT. 774	20	400	Low Cr	1.3
EXT. 775	20	400	High Cr	2.6
EXT. 776	20	400	Low Cr	2.6
EXT. 781	20	482	High Cr	1.3
EXT. 783	20	482	High Cr	2.6
EXT. 788	20	400	High Cr	1.3
EXT. 887*	20	400	High Cr	1.3

*sample supplied by Heather Browne

These 7 extrudates were chosen due to their low PCG depth. Extrudates that displayed a large PCG depth or ones that showed 100% PCG depth were ignored. This

is due to the fact that the PCG structure does not represent the original stored energy from the deformed state. Presumably, these grains are statically recrystallized and, therefore, do not represent deformed material.

Each scanned area was taken at a microscope magnification of 150X. The spot size used was 6 and the working distance was 20mm. At a spot size of 6, the measured beam size is 0.26 mm and the beam current ranges from 3.3 – 5.03 nA.[53] If the spot size exceeds 6, the area that generated the diffraction pattern may exceed the subgrain size of the material. The EBSD analysis software used was OIM Analysis 3.0. A schematic diagram of how EBSD data is formed into a map is shown in Figure 23. Each data point represents the solution from a pattern generated at each individual point. Each point has several characteristics of the pattern collected and saved. These characteristics include, but are not limited to: Euler angles (crystallographic orientation), image quality (strength of the diffracted signal), and confidence index (relationship between the calculated resolved orientation and the actual orientation). A map is then sequenced in a collage of hexagonal data points according to the scanned area. In the OIM software, the user can select a "step size" of the mapped area. The step size is the distance between the centers of each data point represented in Figure 23. Larger step sizes represent a lower resolution while a low step size will give high resolution. For example, a step size of 5 will collect a data point every 5 micrometers. In this analysis, the step size in each OIM map was 1, in order to include all subgrains in the data. Step sizes above 1 would also have eliminated subgrain data by essentially "jumping over" a subgrain. In this software, the collected data can be "cleaned" several

dilation tool automatically assigns it to a grain based on the crystallography of the surrounding points.

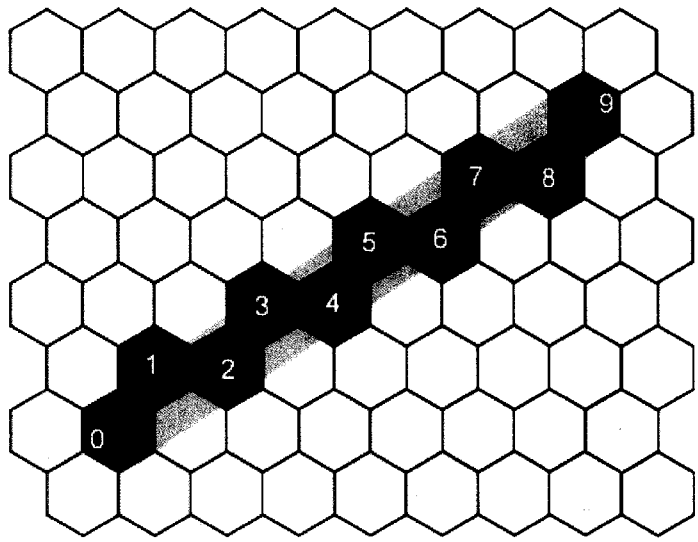

Figure 23: Schematic diagram showing the configuration of pixels in a generic OIM map. In this case, the map represents 72 pixels worth of data points.[54]

In Figure 23, the procedure of the point-to-point misorientation tool in the OIM software is demonstrated. The user can draw a line, in this case from point 0 to 9, and the software will automatically plot the point-to-point misorientations. This becomes important in this research due to the importance of grain boundary misorientation data collected.

5.0 PHYSICAL SIMULATION RESULTS AND DISCUSSION

5.1 Homogenized Material

5.1.1 Light Optical Microscopy

The as – cast and homogenized material was made up of relatively equiaxed grains of consistent average size. Light Optical Micrographs from the industrially homogenized (hot torsion samples) material are shown in Figure 24 for the high Cr 6061 and in Figure 25 for the low Cr 6061. It can be seen that there is an incomplete conversion of the β AlFeSi particles at the grain boundaries in both cases. This may be due to insufficient time or temperature during homogenization. Additionally, there appears to be a Precipitate Free Zone (PFZ) at the grain boundaries. It is not known whether this PFZ represents a lack of Mg_2Si precipitates, Al(Cr,Mn)Si dispersoids or some other second phase particles. The Abrams three – circle method was used to determine the average grain size of material homogenized at Cressona Engineered Products (used for hot torsion) and at Alcoa Technical Center (used for small – scale extrusion and hot rolling). The average grain size based on 10 fields per sample is shown in Table VIII.

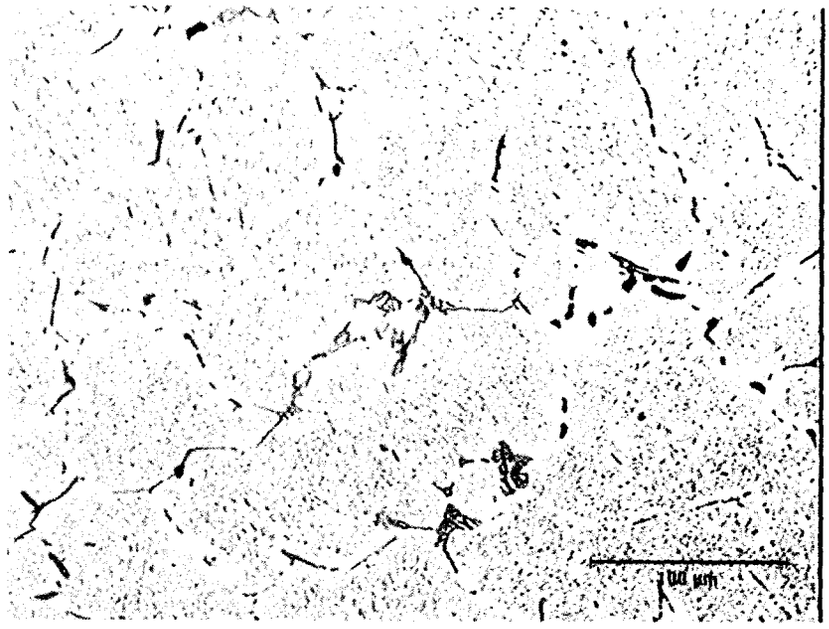

Figure 24: Light Optical Micrograph of as – cast and industrially homogenized high Cr 6061 alloy used in hot torsion testing.

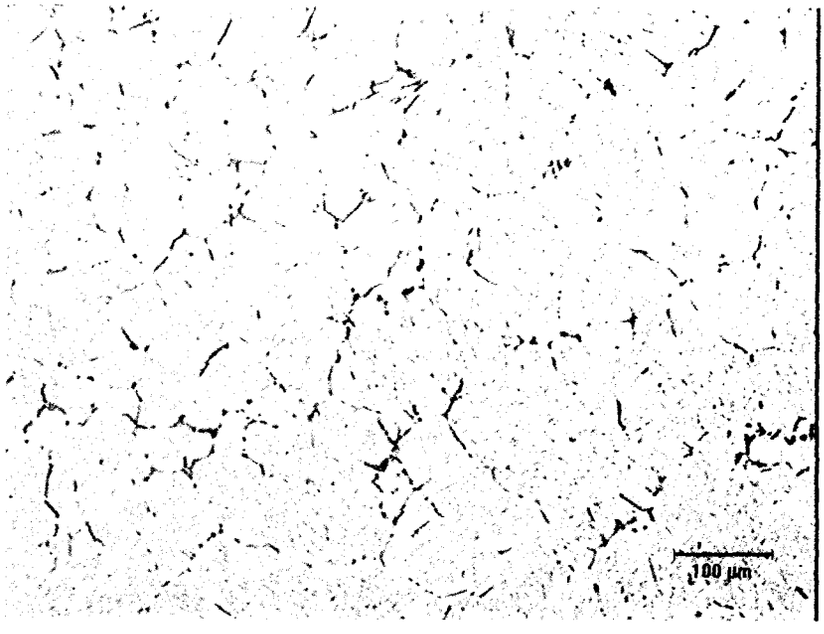

Figure 25: Light Optical Micrograph of as – cast and industrially homogenized low Cr 6061 alloy used in hot torsion testing.

Table VIII: Average grain size for each homogenized material used in physical simulation.

Homogenized Material	Average Grain Size (μm)
ATC (small – scale extrusion and hot rolling)	99.8
Cressona (hot torsion)	123.9

5.1.2 Electron Microscopy and Chemical Analysis

The homogenized material used for hot rolling and small – scale extrusion exhibited a microstructure resembling a typical 6061 alloy, however an incomplete conversion of β to α AlFeSi precipitates was again noticed. A typical microstructure of the homogenized 6061 material is shown in Figure 26.

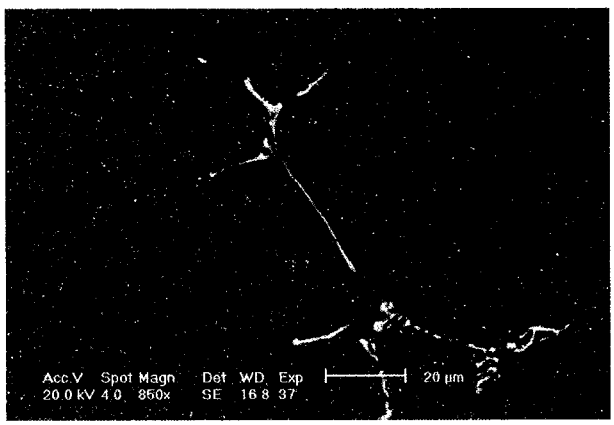

Figure 26: SEM micrograph of homogenized 6061 alloy showing an AlFeSi precipitate at a grain boundary. The dark holes are presumably from pullout of second phase particles during metallographic sample preparation.

The main difference between the two variations of the 6061 alloy (low Cr and high Cr) was the amount Al(Cr,Mn)Si dispersoids. These dispersoids are typically on the order of below 1μm in size and are evenly dispersed within the grains. A high

magnification image of a typical arrangement of these dispersoids in the low Cr 6061 alloy is shown in Figure 27 using backscatter electron contrast. It can be seen that the brighter particles are spherical or slightly elongated in shape and are generally less than 1μm in size. A higher amount of Cr/Mn dispersoids can be seen in Figure 28 for the high Cr 6061 alloy. A more detailed analysis of dispersoid characteristics and volume fraction for these specific alloys are given in the literature [55] In that paper, the volume fractions of Al(Cr,Mn)Si dispersoids for the high Cr and low Cr 6061 alloy were determined to be 0.2% and 0.5%, respectively.

Figure 27: High magnification Backscatter Electron SEM image of Al (Cr,Mn)Si dispersoids in the low Cr 6061 alloy. Light gray particles represent possible Cr/Mn dispersoids.

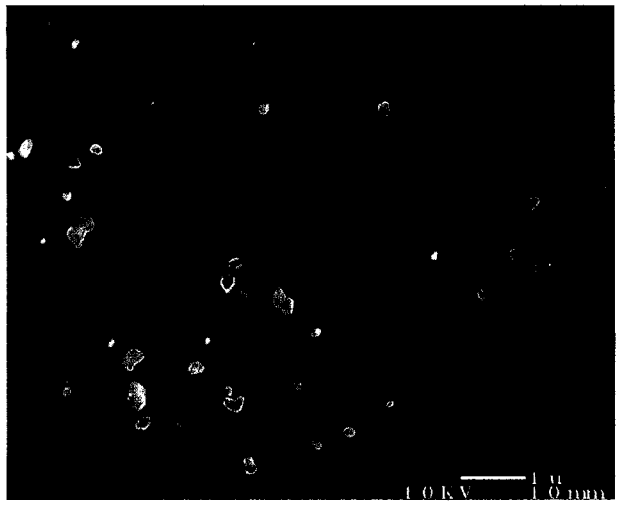

Figure 28: High magnification Backscatter Electron SEM image of Al (Cr,Mn)Si dispersoids in the high Cr 6061 alloy. Light gray particles represent possible Cr/Mn dispersoids.

Energy Dispersive Spectroscopy (EDS) was used to determine the chemical composition of particles in each 6061 alloy studied. There were two types of particles below 1 μm in size that were analyzed in the material by EDS. The first presented themselves as needles or rounded particles with an aspect ratio greater than 1. These particles were identified as most likely Mg_2Si precipitates based on the presence of Mg and Si in the EDS spectrum shown in Figure 29. Finer, more spherical particles were identified by backscatter electron imaging contrast. These particles were identified as most likely AlCrSi particles based on the presence of Cr in the EDS spectrum of Figure 30. The presence of AlMnSi particles was not confirmed or denied in this analysis. In general, Cr/Mn containing particles proved difficult to resolve due to the small size of the dispersoids (below 1μm in size) and the resolution of the EDS technique. It is suggested that Transmission Electron Microscopy be used to more accurately identify and quantify these dispersoids.

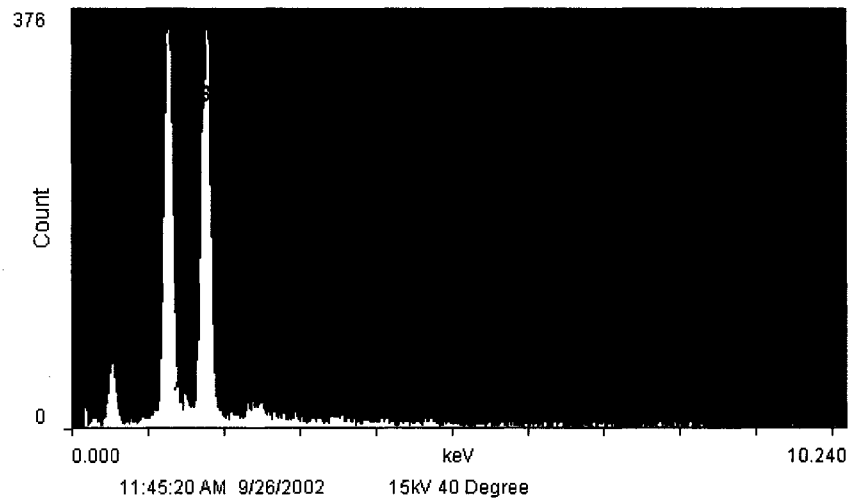

Figure 29: Energy Dispersive Spectroscopy (EDS) plot of Count vs. Energy confirming the presence of large Mg_2Si precipitates.

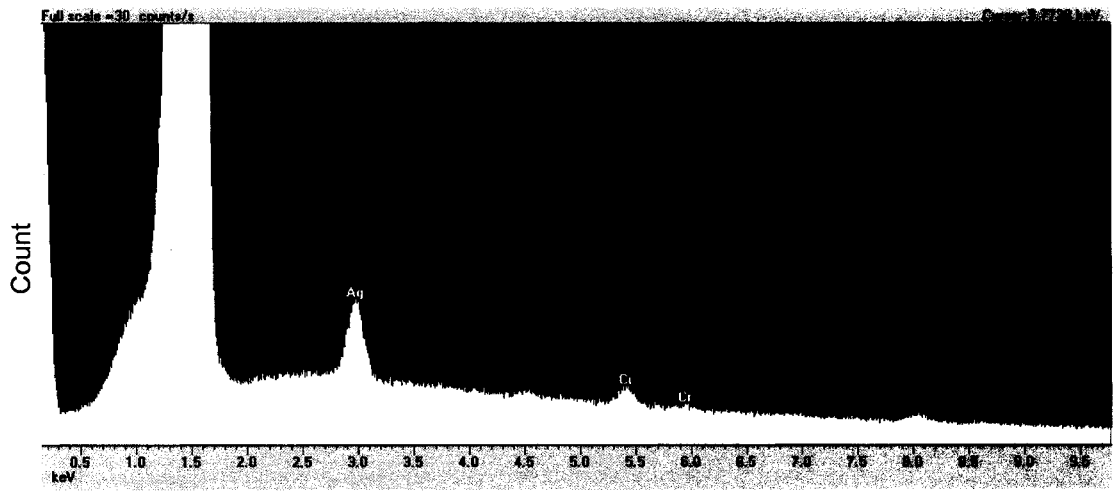

Figure 30: Energy Dispersive Spectroscopy (EDS) plot of Count vs. Energy confirming the presence of Cr containing particles. The Ag peak is most likely a false peak.

5.2 Small – Scale Extrusion

5.2.1 Extrudate Analysis

The material response for each alloy used in small – scale extrusion testing was noticeably different. This can be seen in Figure 31, which shows the breakthrough load for each extrusion condition used. The breakthrough load was determined by extracting the maximum load value before the extrudate begins to flow from the die orifice. It can be seen in Figure 31 that the high Cr alloy resulted in a consistently higher breakthrough load than the low Cr alloy. The breakthrough load increased with higher extrusion ratio, ram speed, and lower starting billet temperature. Additionally, the results show a very consistent mechanical behavior between each test, which shows that each test was free from any abnormal or unexpected behavior.

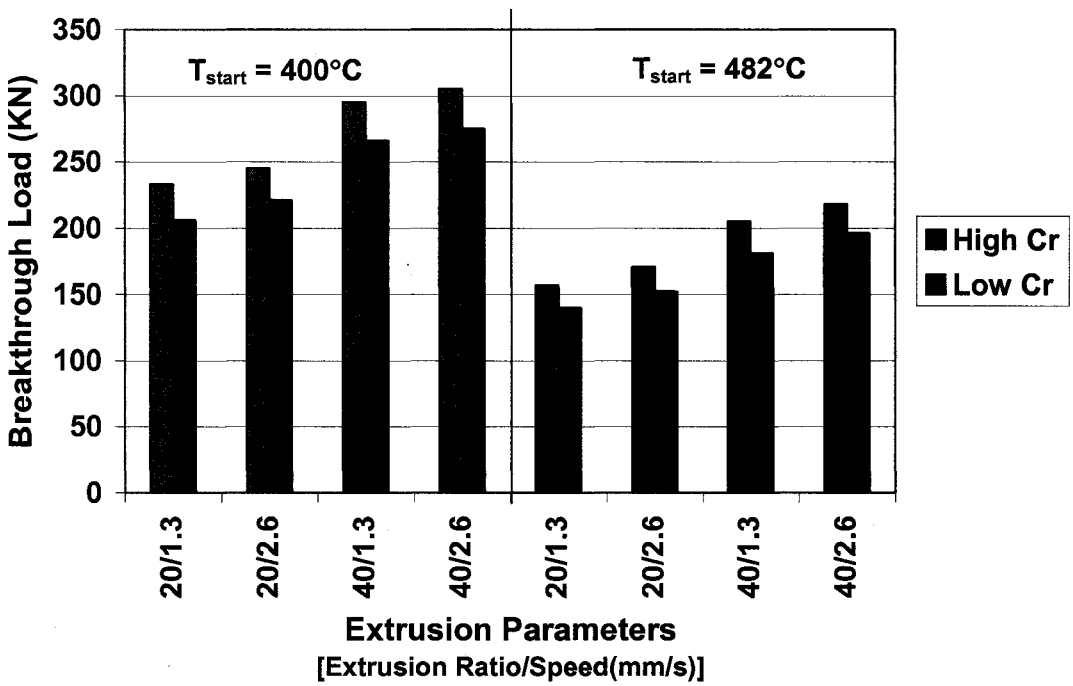

Figure 31: Breakthrough load comparison for High and Low Cr 6061 alloys at two billet starting temperatures, T_{start}. The extrusion parameters shown represent the ram speed (1.3 and 2.6 mm/s) and extrusion ratio (20 and 40).

5.2.1.1 Light Optical Microscopy

A composite picture of microstructures from all of the small – scale extrusion samples can be found in Figure 32 for extrusion ratio, R = 20, and in Figure 33 for R = 40. In each case the samples were sectioned from the mid – length of each extrudate. It can be seen that the recrystallized layer can be characterized as either highly delineated or as scattered recrystallized grains along an average depth. In some cases, lone recrystallized grains appear at the center of the extrudate, far away from the surface recrystallized region. In all extrusion conditions, the grains appear to increase in size from the surface to the center of the extrudate. Additionally, the grains have an aspect ratio greater than 1 and are rarely equiaxed in shape. Some grains appear very elongated in the extrusion direction, especially in the regions closer to the center of the extrudate. As can be seen in Tables IX and X, the depth of the PCG layer is lowest at 63 μm for the high alloy, low ram speed, low extrusion ratio, and low start temperature. A fully recrystallized extrudate (2mm in radius for R = 40) is found in the low alloy, high ram speed, high extrusion ratio, and high start temperature. A range of values therefore coincides with the chemistry and extrusion parameters of billet temperatures, extrusion ratio, and ram speed.

Figures 34 and 35 show plots of the recrystallized depth as a percentage of the extrudate radius for each extrusion ratio according to the extrusion condition. Note that the depths are arranged in increasing value for each extrusion parameter. It can be seen that the recrystallized depth increases with increasing extrusion ratio, ram speed and billet temperature. Additionally, the high Cr 6061 alloy had a consistently lower

recrystallized depth than the low Cr 6061 alloy. In both alloys extruded with an extrusion ratio of 40, the recrystallized depth seems to be larger than expected for the case of the lower billet temperature and higher ram speed. This may be explained by the fact that the extrudate, due to the higher extrusion ratio, had a faster exit speed, whereby the quenching effectiveness would not be as high as other conditions.

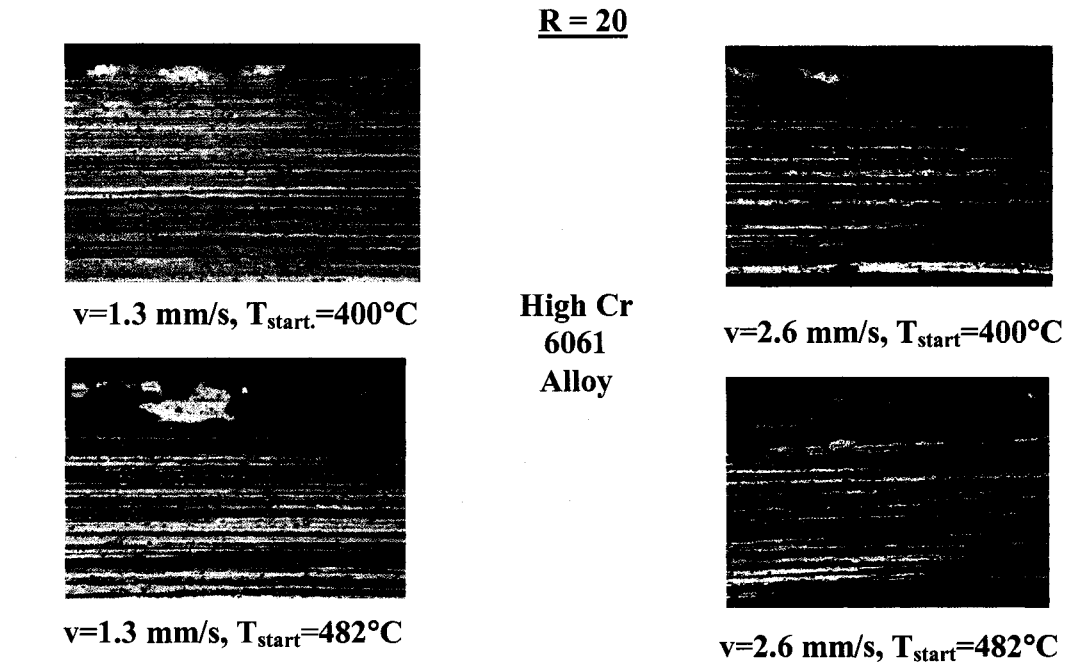

Figure 32: Light Optical Micrographs from half – length of the extrudates showing the surface recrystallized depths for each ram speed, v (mm/s), starting billet temperature, T_{start} and extrusion ratio, R = 20.

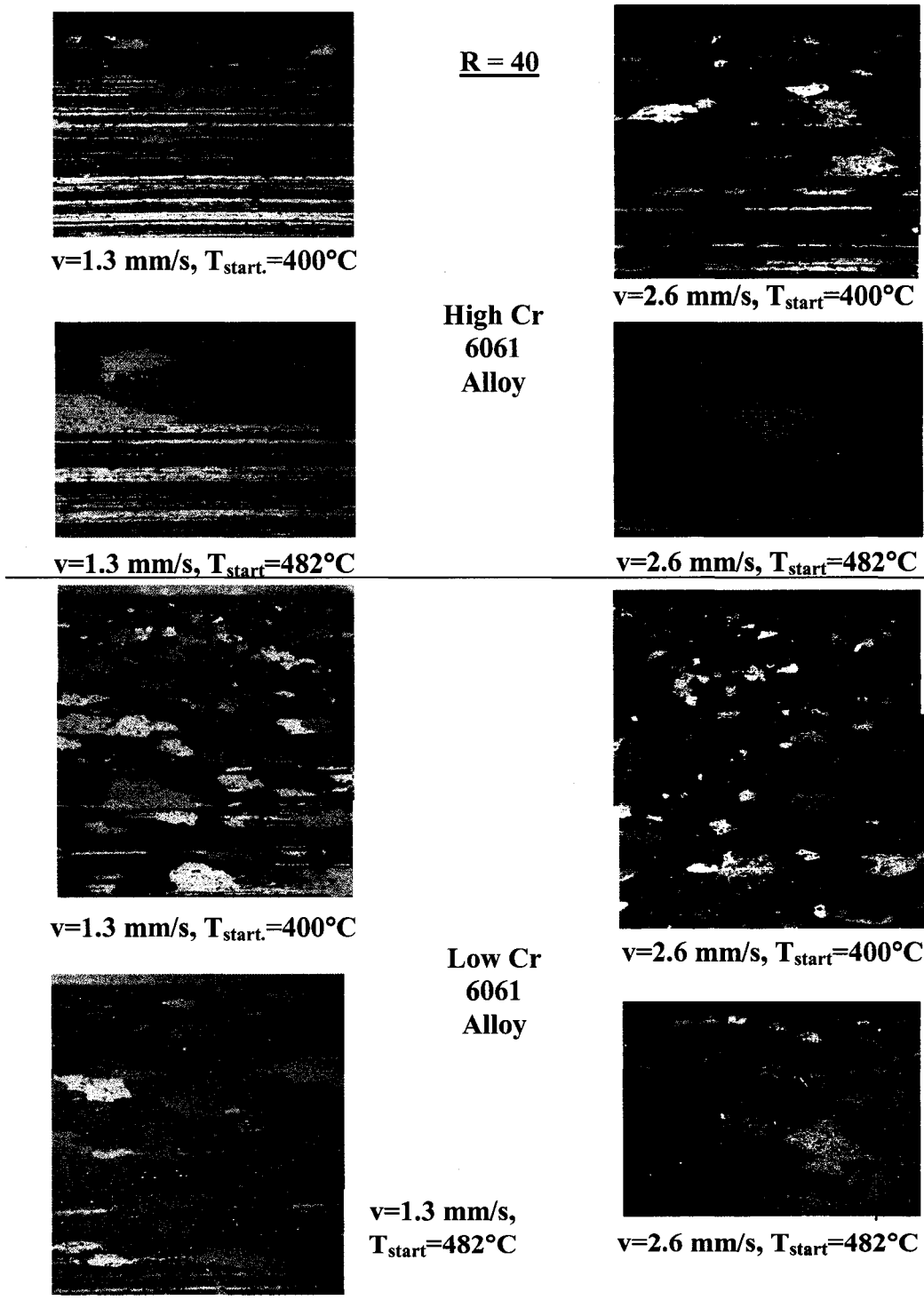

Figure 33: Light Optical Micrographs from half – length of the extrudates showing the surface recrystallized depths for each ram speed, v (mm/s), starting billet temperature, T_{start} and extrusion ratio, R = 40.

Table IX: Depth of recrystallized layer in an extrudate of radius 3.4 cm for each extrusion parameters, R = 20.

Material	Ram speed (mm/s)	T_{start} °C (°F)	Recrystallization Depth (μm)
High Cr Alloy	1.3	400 (752)	63.0
High Cr Alloy	2.6	400 (752)	128.6
High Cr Alloy	1.3	482 (900)	166.5
High Cr Alloy	2.6	482 (900)	300.2
Low Cr Alloy	1.3	400 (752)	334.0
Low Cr Alloy	2.6	400 (752)	700.8
Low Cr Alloy	1.3	482 (900)	752.0
Low Cr Alloy	2.6	482 (900)	1181.0

Table X: Depth of recrystallized layer in an extrudate of radius 2.4 cm for each extrusion parameters, R = 40.

Material	Ram speed (mm/s)	T_{start} °C (°F)	Recrystallization Depth (μm)
High Cr Alloy	1.3	400 (752)	277.5
High Cr Alloy	2.6	400 (752)	805.6
High Cr Alloy	1.3	482 (900)	367.2
High Cr Alloy	2.6	482 (900)	689.5
Low Cr Alloy	1.3	400 (752)	1113.5
Low Cr Alloy	2.6	400 (752)	2 mm (all Rx)
Low Cr Alloy	1.3	482 (900)	1386.0
Low Cr Alloy	2.6	482 (900)	2mm (all Rx)

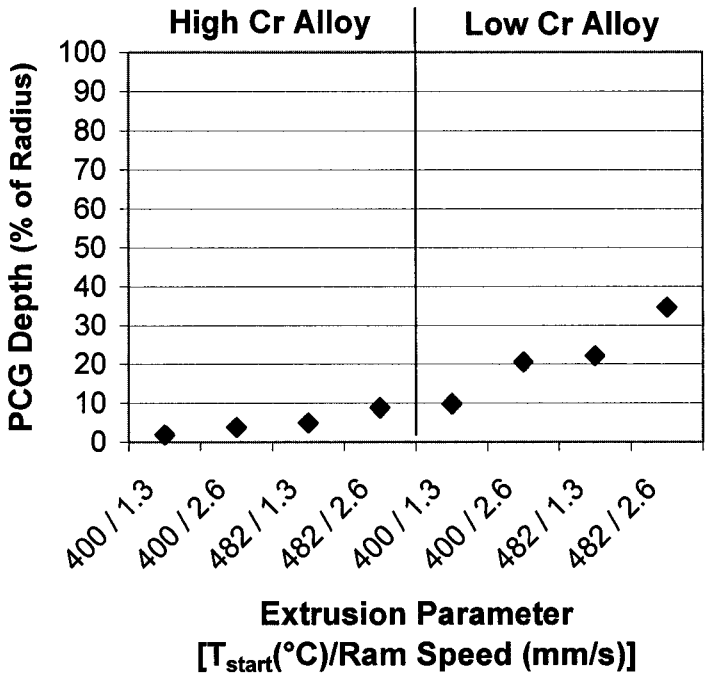

Figure 34: Depth of Peripheral Coarse Grain (PCG) structure in small scale extrusion samples with extrusion ratio, R = 20.

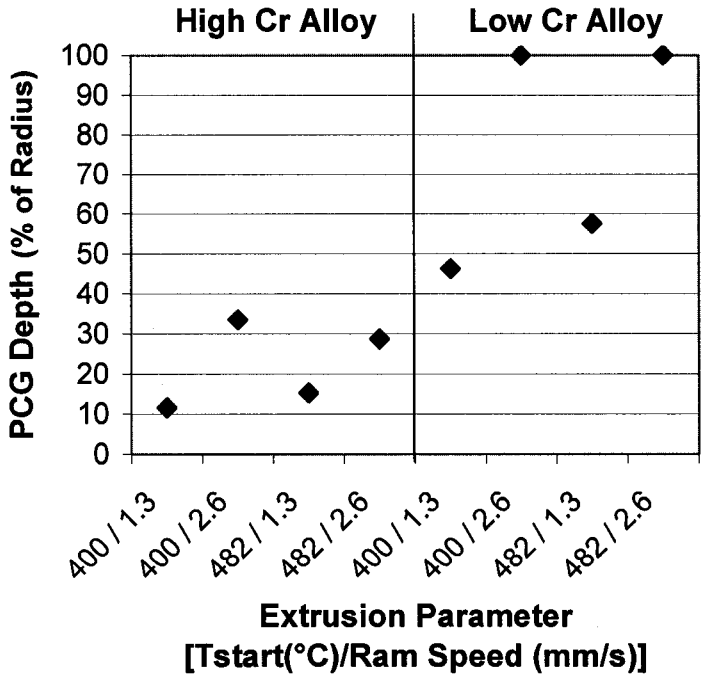

Figure 35: Depth of Peripheral Coarse Grain (PCG) structure in small – scale extrusion samples with extrusion ratio, R = 40.

In order to understand the kinetics of the coarse grain recrystallized region, samples from water quenched small – scale extrudates [56] were used for salt bath annealing experiments. The sample designations and corresponding extrusion conditions are shown in Table XI. Figure 36 shows the results of the annealing experiments, which were performed with a bath temperature of 490°C for 3, 6, and 9s. Also plotted on the graph separately are the PCG depth results from small – scale extrudates that underwent a slightly slower forced air cool. It is interesting to see that the PCG depth increases with time up to 9 seconds of annealing time. When the depth at 9 seconds is compared to that of the air cooled samples, there is a diversion in the kinetics between the low extrusion ratio samples (samples 887 and 883) and the high extrusion ratio samples (samples 886 and 881). The samples with lower extrusion ratio reach their PCG depths at 9 seconds and do not increase substantially to whatever time it takes to cool via air cooling. Conversely, the samples with higher extrusion ratio had a PCG depth that continues to increase substantially beyond the 9s to the point where it is air cooled. The kinetics beyond the air cooling are not known, but it can be assumed that recrystallization of the surface and center will continue with longer time to allow further nucleation and growth of the center region.

Table XI: Sample designations corresponding to extrusion parameters of extrudates used in salt bath annealing experiments.

Sample	Alloy	Extrusion Ratio	Billet Start T (°C)	Ram Speed (mm/s)
881	High Cr 6061	40	400	2.6
886	High Cr 6061	40	400	1.3
883	High Cr 6061	20	400	2.6
887	High Cr 6061	20	400	1.3

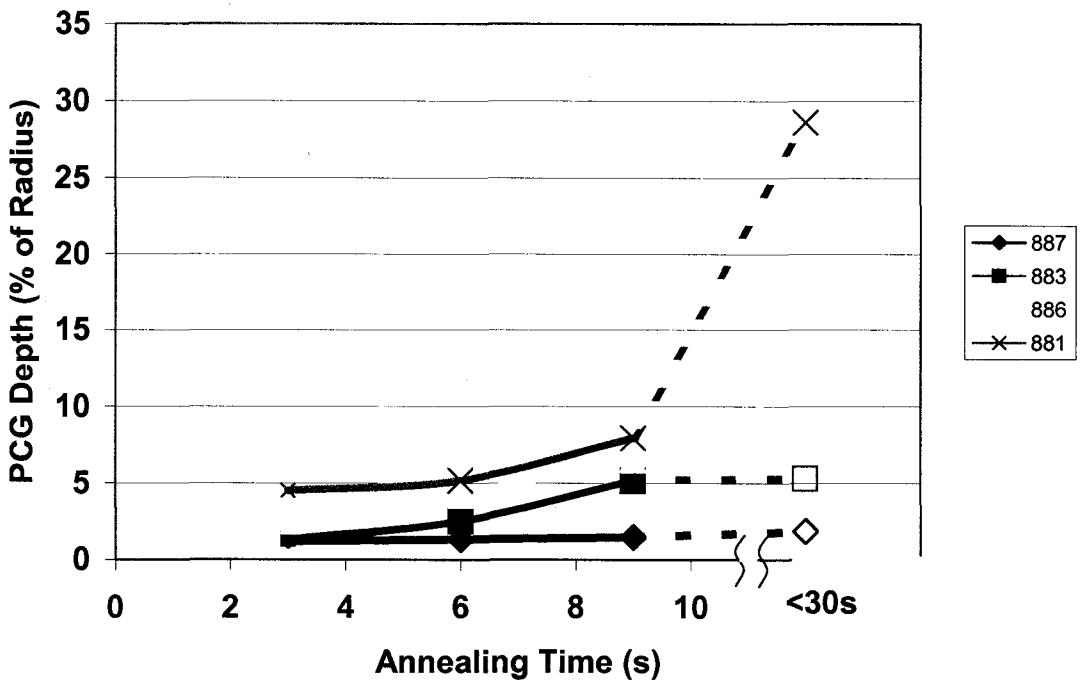

Figure 36: Water – quenched extrudate PCG Depths as a function of annealing time in a salt bath heated to 490°C. The open circles correspond to as – extruded depths using air quenching.

Since the main parameter difference between the two sets of samples is the extrusion ratio, the strain seems to play a dominant role in the annealing behavior of the extrudate surface. However, since a higher extrusion ratio also may increase the effective strain rate and temperature at the surface, a direct correlation between the strain and the annealing kinetics alone cannot be made.

5.2.1.2 Orientation Imaging Microscopy

From the sixteen small – scale extrusion tests that were performed, seven were chosen for their low PCG depth in order to further characterize the deformed structure by electron microscopy. In each case, EBSD maps were collected from the center of the extrudate to the surface, until the coarse recrystallized grains were encountered. The results of EBSD scans from the seven extrudates are shown in Figures 37 – 43. In each Figure, three collages of EBSD maps are shown, each corresponding to the same area scanned within each sample. The top collage represents the orientation maps, each color representing specific textures as defined by the inverse pole figure. The center collage represents the maps of boundaries with misorientations of 1 - 5°, 5 - 15°, and 15° and higher, corresponding to the color key. The colored boundaries are overlayed onto an image quality map. Image quality maps represent the strength of the signal from each diffracted pattern. Therefore, highly deformed grains will appear darker due to the effect of dislocation density on the quality of the pattern. Conversely, statically recrystallized grains will appear brighter due to the deformation free crystal producing a higher pattern signal. Finally, the lower collage represents the maps showing only boundaries with misorientations of 15° and higher. Pole figures for each extrusion condition analyzed by EBSD were created to determine the deformation textures present. A typical example of pole figures from the center to the surface of an extrudate is shown in Figure 44 for the case of sample 887. This sample has been taken from previous work on small – scale extrusion that had been water quenched.[55]

In each sample, there is consistently a microstructure of banded or fibrous

structure. The width of these bands decreases from the center to the surface, corresponding to the strain induced on the material. The bands correspond to alternating textures between {110} <111> or {121} <111> (blue) and {101}<010> or {100} <010> (red) are seen in Figures 37 - 43. Within each banded region, there are subgrains, which can be identified by the red and green boundaries, corresponding to orientations below 15°. In each case, the textures designated in blue did not exhibit grain boundary misorientations higher than 15°. Each texture corresponded to a specific type of microstructure. The textures designated in blue were characterized as long bands with substructure. Conversely, the textures designated in red correspond to a microstructure comprised of broken up grains that were frequently equiaxed in nature. Towards the surface of each sample, the structure of the extrudate gradually changes to one that is comprised mostly of fine, equiaxed grains. Some low angle misorientations were observed, but only in relatively low amounts. Additionally, the texture of these grains at the surface no longer represents that of the banded/fibrous grains, but is instead a copper texture that has been sheared in the ND direction. These grains represent a {332} <353> texture as can be seen in the pole figure in Figure 44 - Surface. The origin of this texture will be explained in Section 5.2.2.2.

The presence of coarse, recrystallized grains within the center of the extrudate can be seen in Figures 37 and 39. In Figure 39, the recrystallized grains generally have an aspect ratio greater than 1 and are growing in the extrusion direction. Upon further inspection of this region, one can notice that these grains are sometimes bounded by the high angle grain boundaries separating each deformation band.

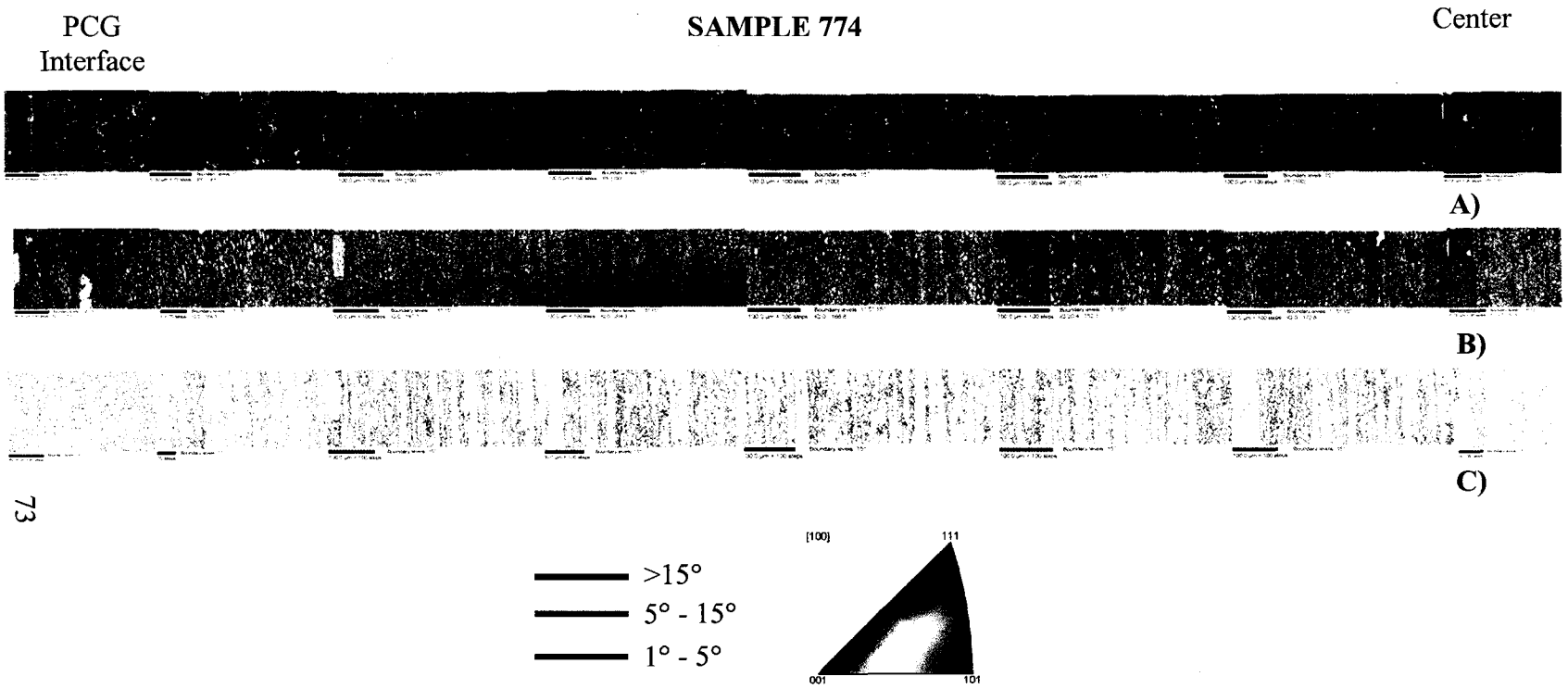

Figure 37: Collage of EBSD maps representing A) Crystallographic orientation of the grains, B) Boundary Misorientations, and C) Boundary misorientations above 15°.

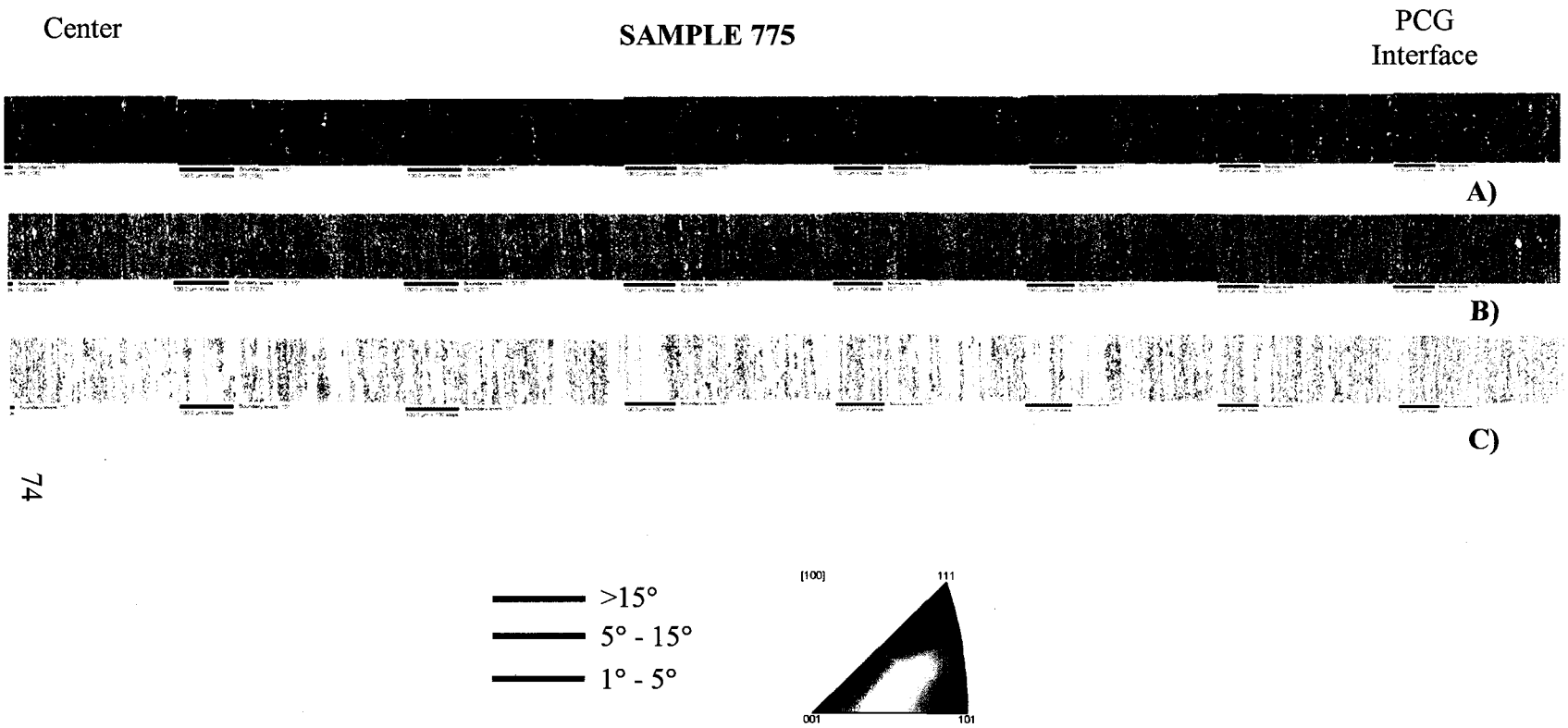

Figure 38: Collage of EBSD maps representing A) Crystallographic orientation of the grains, B) Boundary Misorientations, and C) Boundary misorientations above 15°.

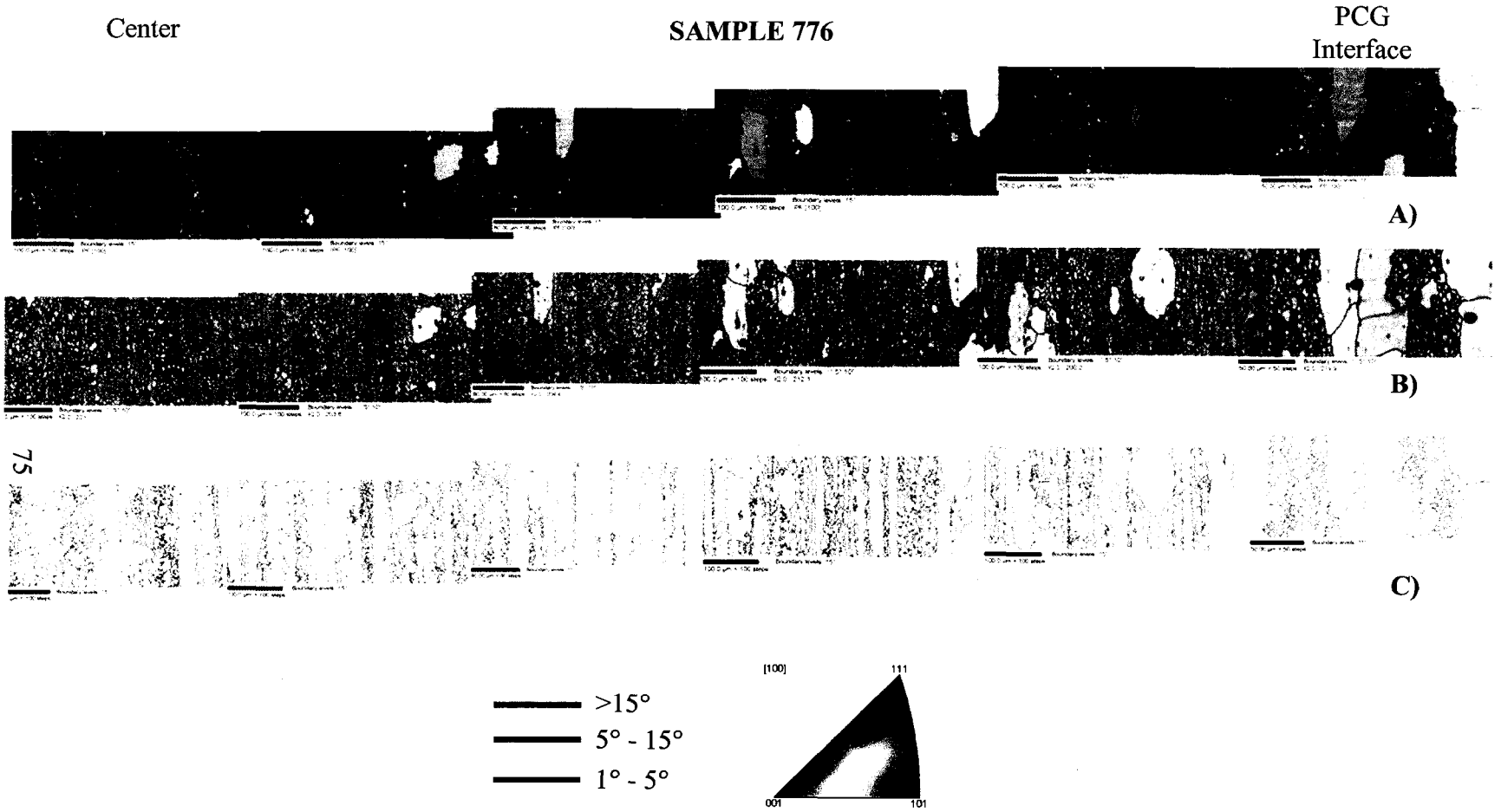

Figure 39: Collage of EBSD maps representing A) Crystallographic orientation of the grains, B) Boundary Misorientations, and C) Boundary misorientations above 15°.

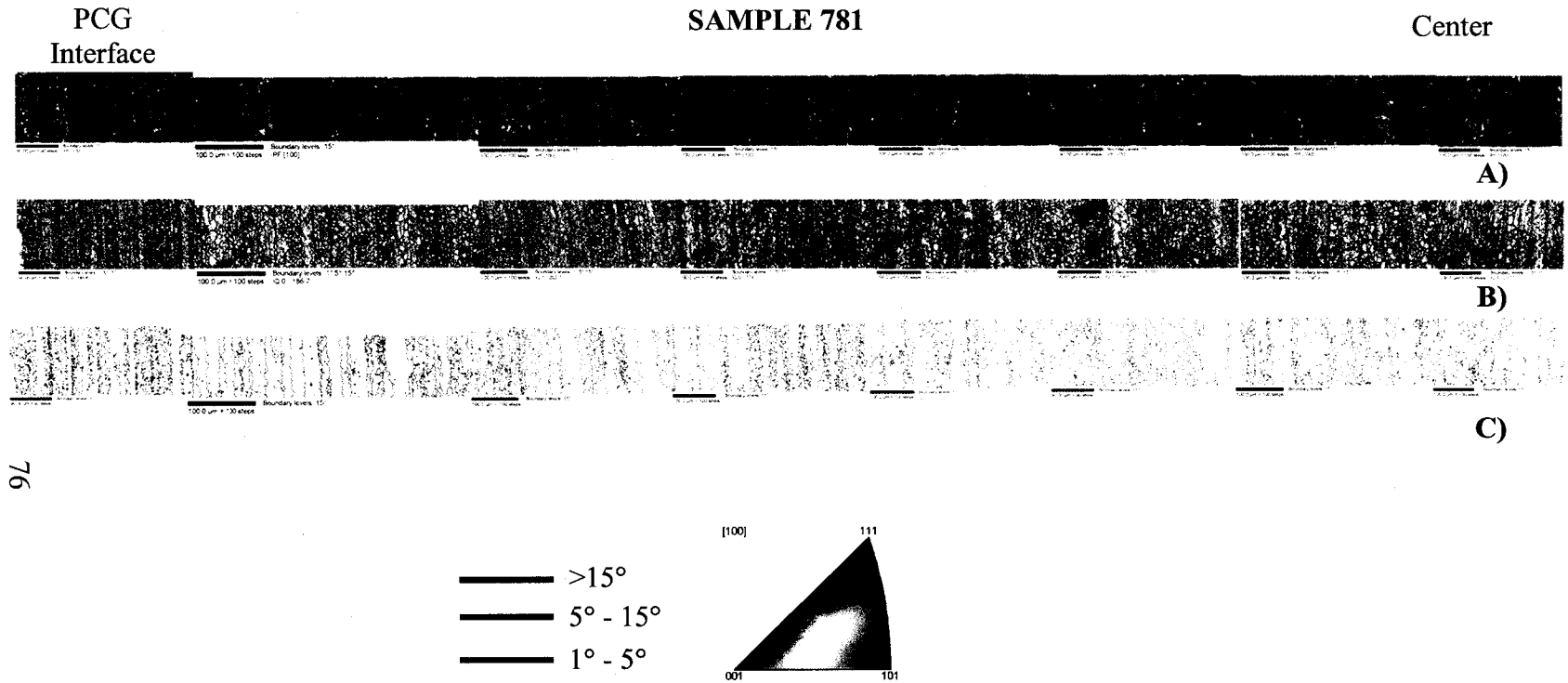

Figure 40: Collage of EBSD maps representing A) Crystallographic orientation of the grains, B) Boundary Misorientations, and C) Boundary misorientations above 15°.

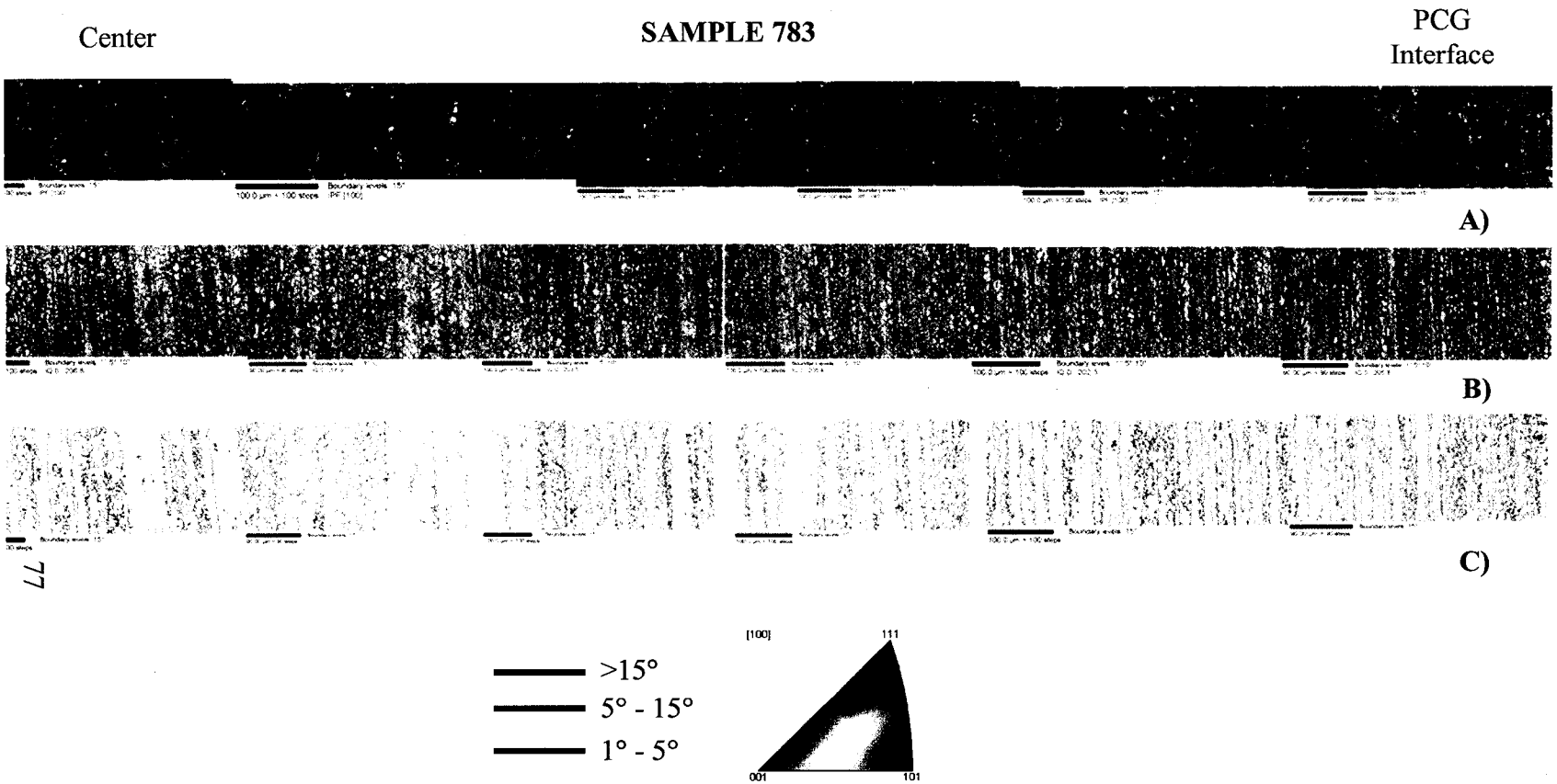

Figure 41: Collage of EBSD maps representing A) Crystallographic orientation of the grains, B) Boundary Misorientations, and C) Boundary misorientations above 15°.

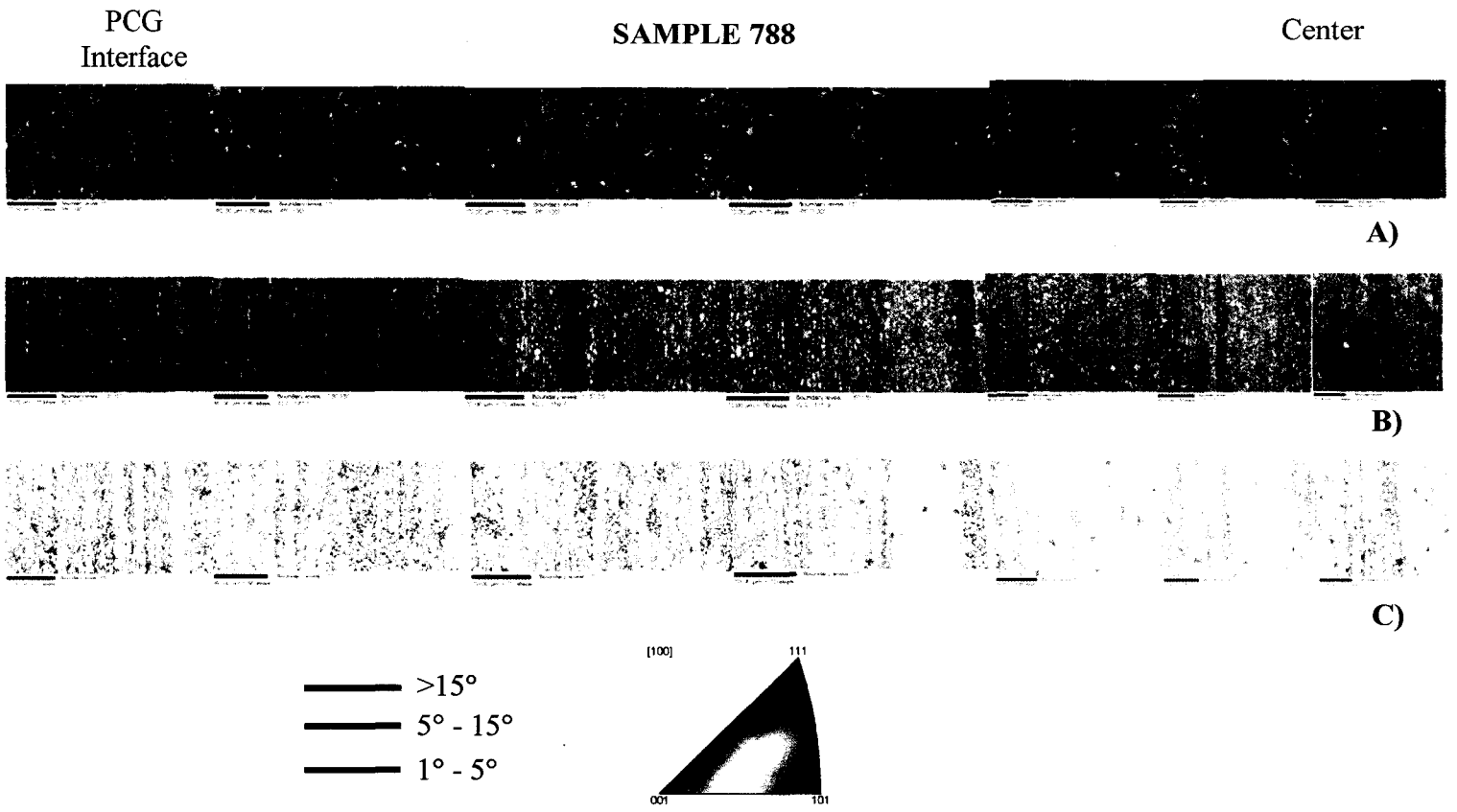

Figure 42: Collage of EBSD maps representing A) Crystallographic orientation of the grains, B) Boundary Misorientations, and C) Boundary misorientations above 15°.

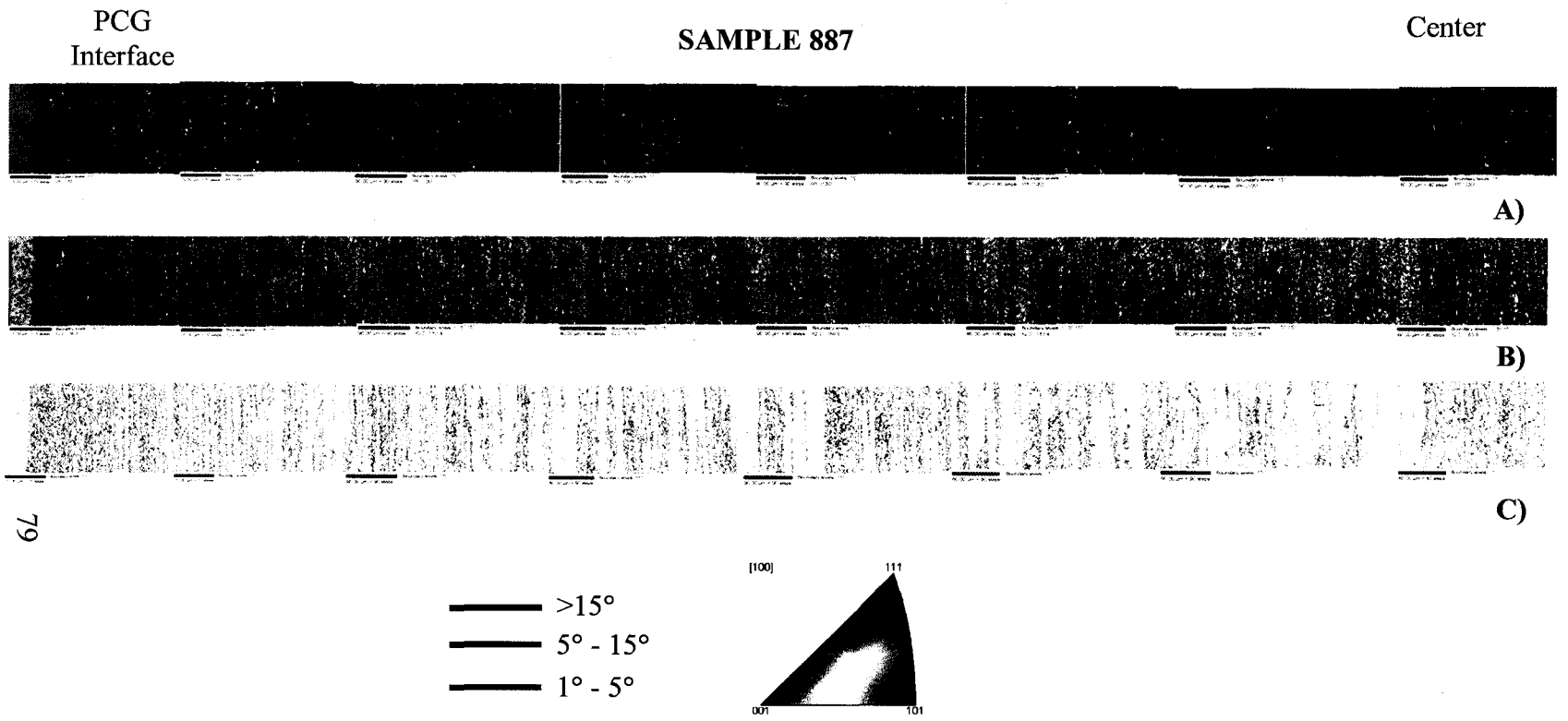

Figure 43: Collage of EBSD maps representing A) Crystallographic orientation of the grains, B) Boundary Misorientations, and C) Boundary misorientations above 15°.

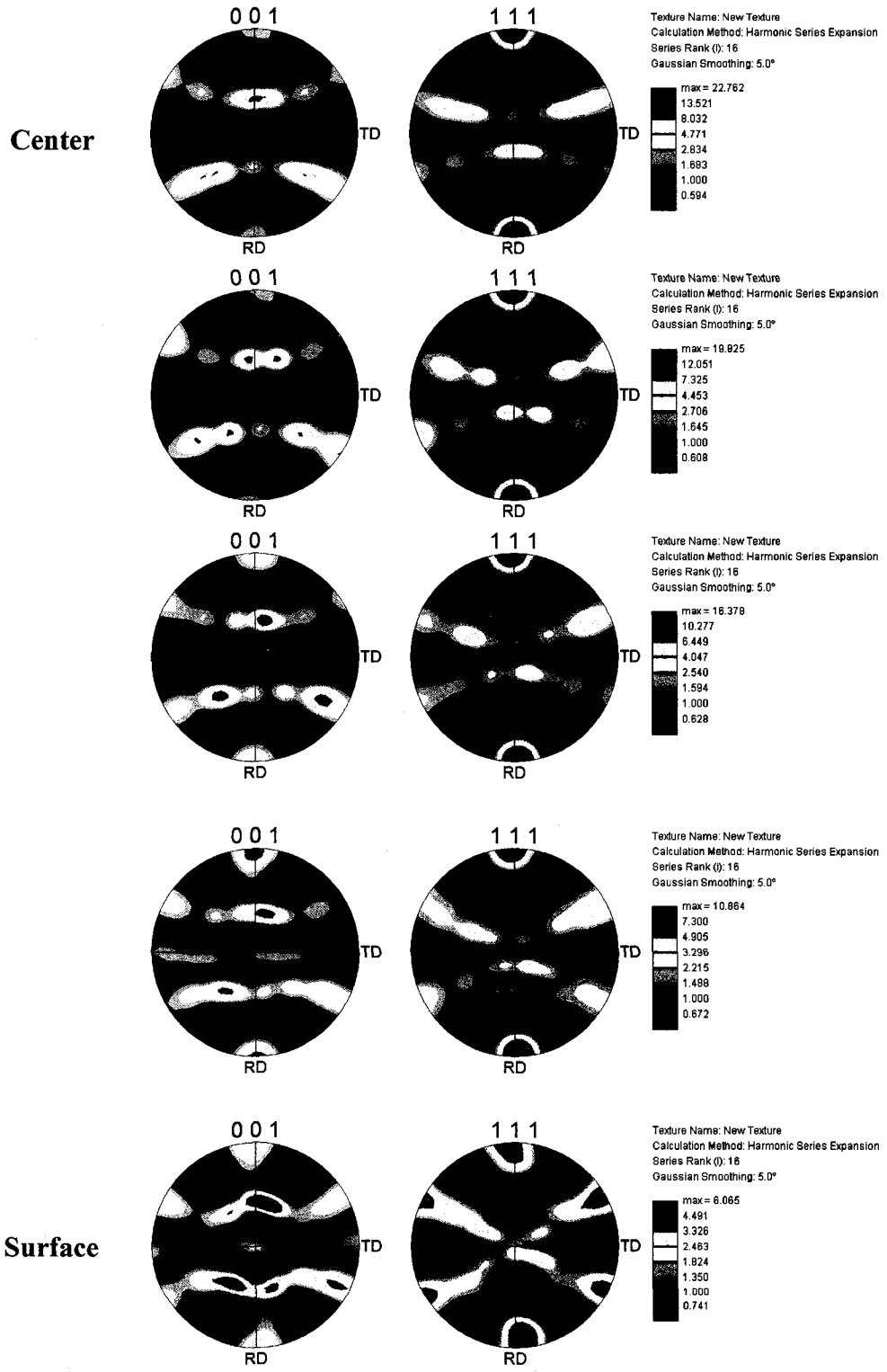

Figure 44: Experimental texture results from the center to the surface extrudate from separate experiments [55] with water quenching after extrusion.

In order to quantify the structure of the extrudate from the center to the surface, information relating to the grain size and misorientation were extracted from the EBSD scans. In this analysis, a grain in the OIM software has been defined as having boundary misorientation greater than 15°. In Figure 45, the quantity of grains with diameters between 2 and 10 μm per 1000 μm of area has been plotted as a function of the distance from the surface of the extrudate. In general, the quantity of these grains increased from the center to the surface of the extrudate. In the case of sample 887, which represents an extrudate cooled by water quenching, the quantity of small grains is noticeably higher than all other conditions. The sinuous nature of the trend can be related to the alternating presence and lack of the {100}<001> and {110}<001> bands. Again, it was in these bands that small, equiaxed grains were found. Within the bands of {110} <111> or {121} <111>, there was rarely any presence of grains less than 10 μm in diameter.

Due to the variation in grain sizes in the extrudate, it can be reasonably expected that the average misorientation of grains will be different between the center and surface of extrudate. The frequency of boundary misorientations at the center, mid – radius, and surface of sample 887 can be seen in Figures 46 – 48. It can be seen that the population of low angle boundaries decrease from the center to the surface. At the surface, there is a broadening of grain boundary misorientation with a higher population of misorientations between 10 and 40°. This same effect was noticed in all seven extrudates analyzed by EBSD.

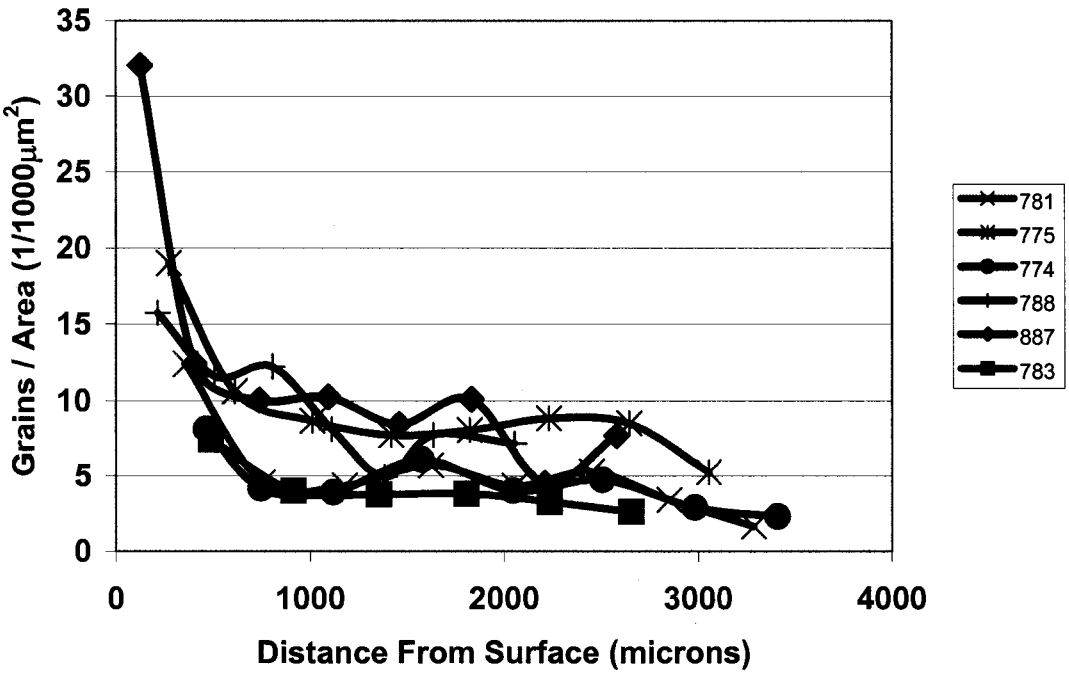

Figure 45: Population of grains with a grain diameter between 2 and 10 μm as a function of distance from the extrudate surface.

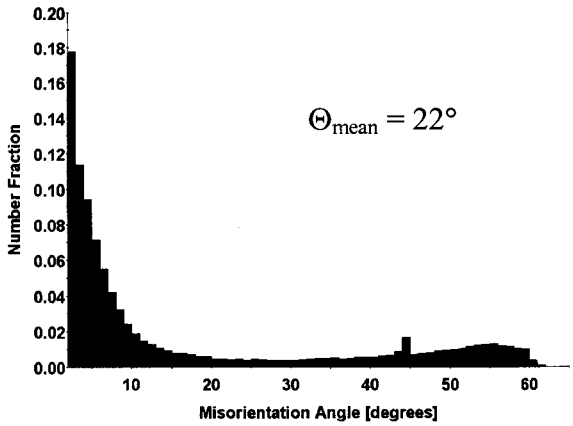

Figure 46: Number fraction of grain boundary misorientations from the center of sample 887.

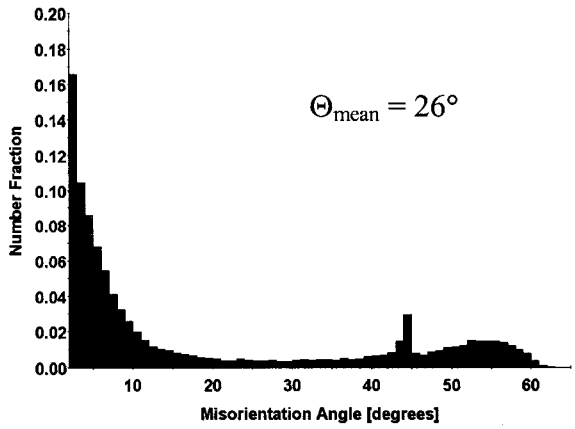

Figure 47: Number fraction of grain boundary misorientations from the mid - radius of sample 887.

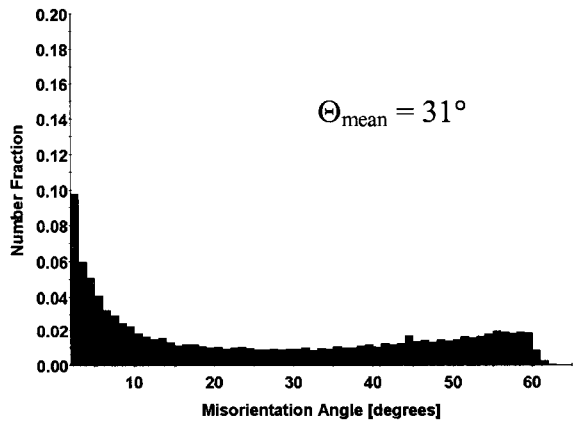

Figure 48: Number fraction of grain boundary misorientations from the surface of sample 887.

The resultant orientation maps from the coarse grain PCG region are shown in Figures 49 A and B. It can be seen that these recrystallized grains also have an aspect ratio greater than 1, but are generally closer to an equiaxed shape than that of grains within the center of the extrudate. Remnants of the deformed structure can also be noticed and are marked by arrows. The large, recrystallized grains present at the surface of the extrudate and within the center of the sample were identified as having a weak cube {100} <001> texture at the surface. However, there were many instances where coarse recrystallized grains exhibited a crystallographic orientation similar to the Copper texture rotated about the Normal Direction (ND) as well as other deformation textures. The lack of a random texture signifies that Particle Stimulated Nucleation does not play a dominant role in the nucleation of the PCG grains.

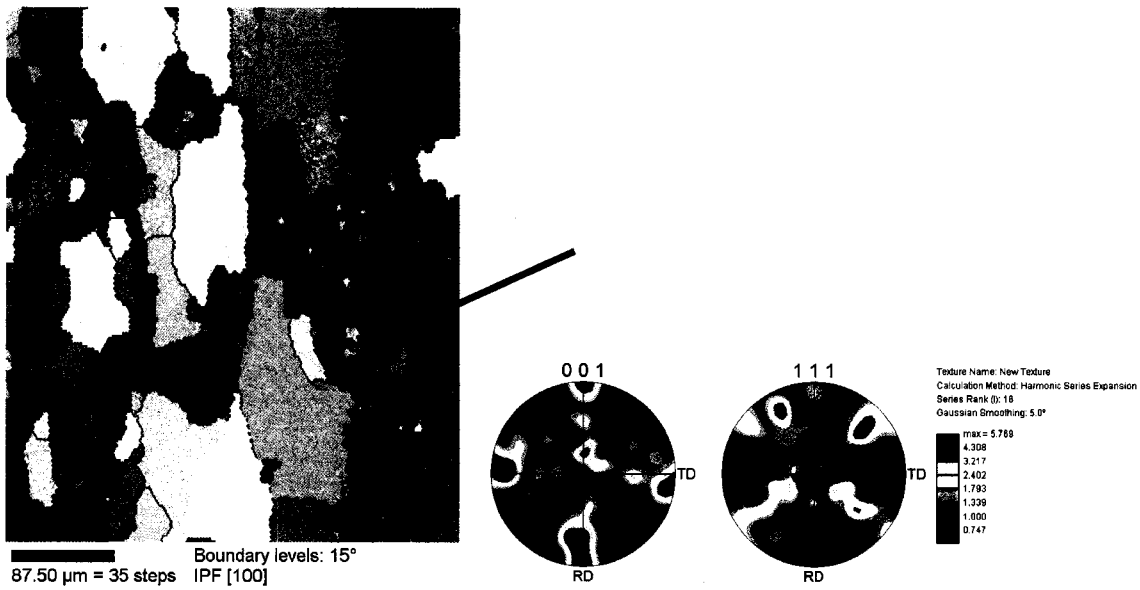

A)

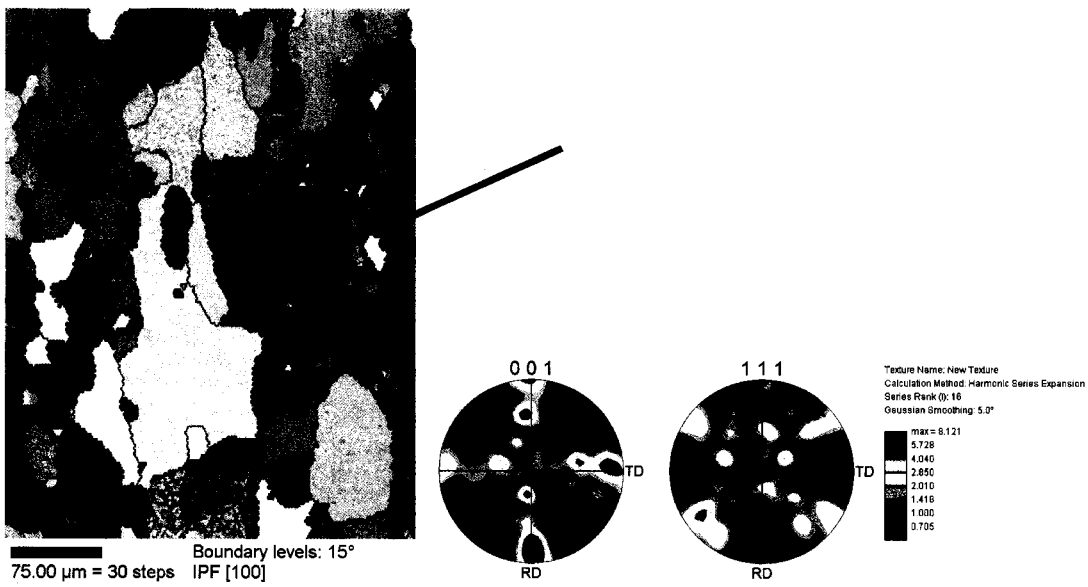

B)

Figure 49: EBSD orientation maps of PCG structures and their resultant pole figures for two extrusion cases. A) R = 40, B) R = 20. Remnants of the deformed structure are marked by arrows.

5.2.2 Billet Discard Analysis

5.2.2.1 Billet Discard – Light Optical Microscopy

In order to further understand the microstructural evolution of the billet and extrudate, the billet discard was examined for each small – scale extrusion case. It was found that in each billet discard, a DMZ developed along the face of the die. A collage of LOM micrographs from one half of a billet discard after 75% completion along the billet/die interface is shown in Figure 50. It can be seen that there is a distinct region of the DMZ in a hemispherical shape along the die/billet interface. Surprisingly, within this region, very small (<10μm) grains were observed. By using traditional electroetching procedures, the fine detail of this DMZ was not very clear using polarized light optical microscopy, especially at higher magnification. Therefore, SEM characterization needed to be performed to further analyze the grains in this region (see Section 5.2.2.2).

Further into the partially extruded billet, beyond the DMZ, the microstructure resembled a "banded" or "fibrous" appearance with elongated grains flowing into the die exit. The effect of processing conditions on the microstructure of the DMZ region is shown in Figure 51 for three extrusion cases. It should be noted here that the microstructures shown in the figures of this section were all left in the billet container for approximately 60 seconds after extrusion was completed. Therefore, it should be assumed that some post – deformation annealing would occur in these billets. With an increase in exit speed and starting billet temperature, the quantity of very large,

recrystallized grains increased. It can be seen in Figure 51 A that there is no presence of large recrystallized grain formation at the surface of the extrudate. In Figures 51 B and C there are very large grains that have grown at the extrudate surface and within the DMZ after extrusion (only in Figure 51C). The coarse grains within the DMZ have grown away from the die/billet interface and appear to have grown along the DMZ / fibrous region interface instead. Each of the samples shown in Figure 51 represent the high Cr alloy and were extruded with an extrusion ratio, R, of 20. With the exception of the high extrusion temperature and ram speed (Figure 51C), all of the high Cr alloys did not exhibit coarse grain formation within the DMZ. In contrast, all of the low Cr alloy billets had evidence of coarse grain formation in the DMZ. More precise dimensions of this region and the location of the DMZ / Fibrous region interface are discussed in another work [55].

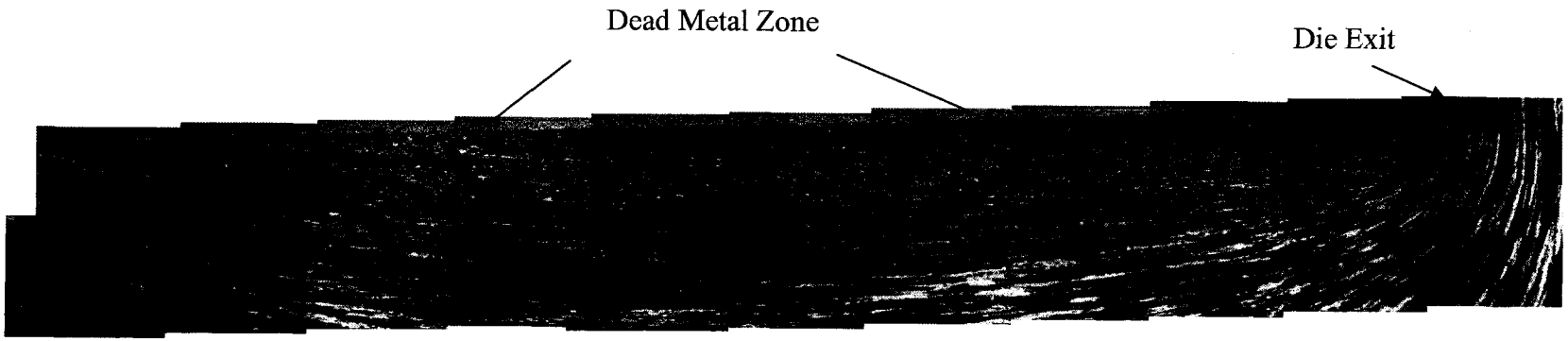

Figure 50: Collage of Light Optical Micrographs taken from the DMZ of a partially extruded small – scale extrusion billet 783. The extrusion direction is upwards.

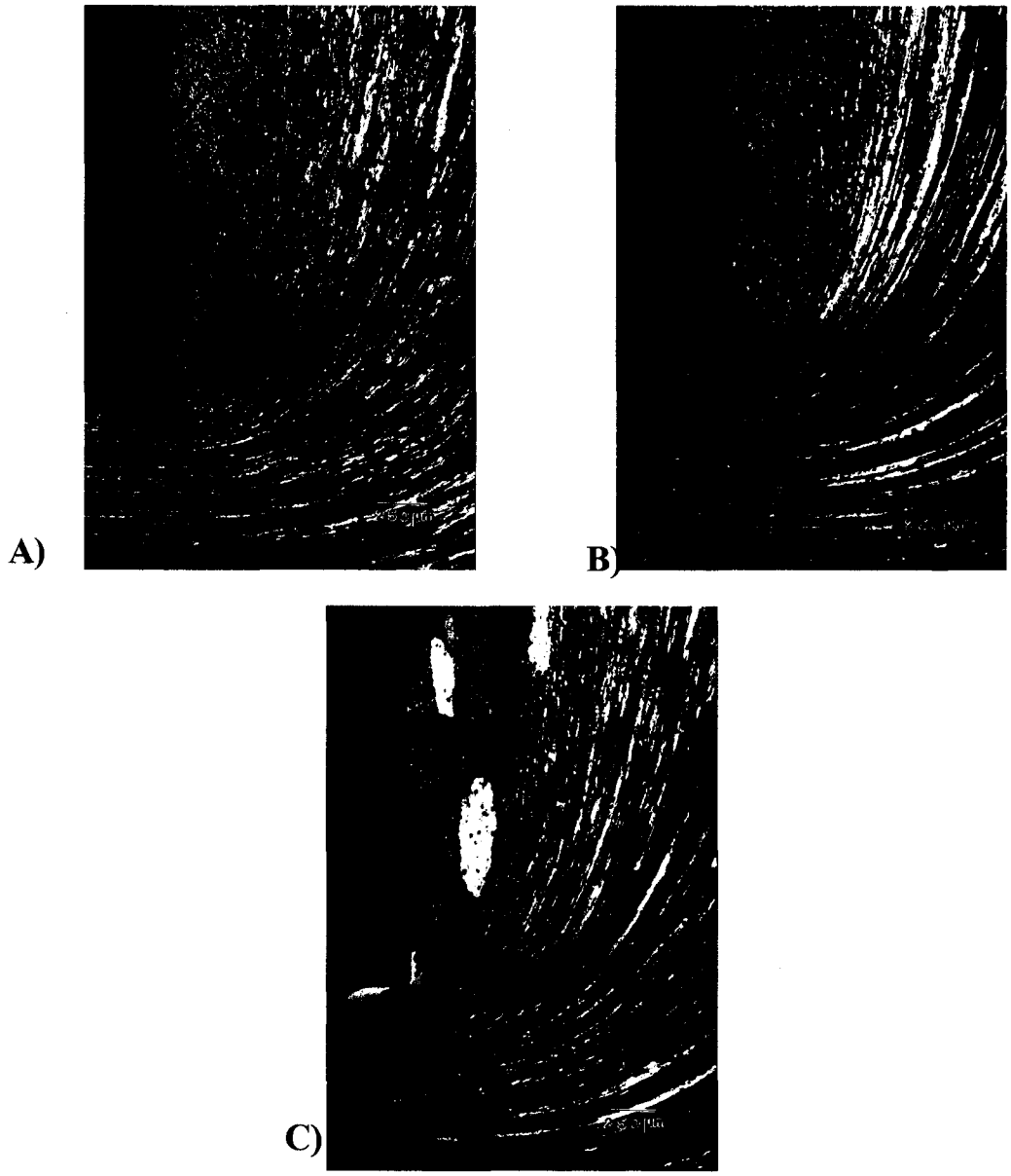

Figure 51: Light Optical Micrographs of partially extruded billets at the die exit. A) v = 1.3 mm/s, T_{start} = 400°C, B) v = 1.3 mm/s, T_{start} = 482°C, C) v = 2.6 mm/s, T_{start} = 482°C. The extrusion ratio is the same for all three cases at R = 20. The extrusion direction is to the left.

Upon further inspection of the die exit region, it was noticed, in most extrusion conditions tested, that large recrystallized grains were present at the surface of the extrudate as it exits the die. As can be seen in Figure 52 A and B, the PCG structure similar to the extrudate microstructures appears to be formed at the die exit. Additionally, at higher magnification (Figure 52B), it appears that these large recrystallized grains are growing into the region of DMZ within the billet. The jagged nature of the growing grains suggests some preferential growth. Fortuitously, in 3 cases out of the 16 extrusion conditions tested, there was no presence of large recrystallized grains at the die exit. The sample conditions that resulted in no large, recrystallized grain formation are listed in Table XII.

Table XII: Extrusion conditions from samples containing no coarse grain formation on the extrudate surface at the die exit.

Sample Designation	Alloy	Ram Speed (mm/s)	T_{start} (°C)	Extrusion ratio, R
788	High Cr 6061	1.3	400	20
775	High Cr 6061	2.6	400	20
791	High Cr 6061	1.3	400	40

An example of a case where no large recrystallized grains were present at the surface of the extrudate can be seen in Figure 53, which is a collage of LOM images of the die exit and beginning of the extrudate. In each of the 3 cases in Table XII, a region of fine, equiaxed grains was present in the DMZ region, and then extending into the

surface of the extrudate. At approximately 1.5 mm from the die exit, large, recrystallized grains appear to have formed. It can be reasonably assumed from this Figure that large recrystallized grains have not formed until after the die exit. Therefore, the formation of the coarse grains has not occurred within the deformation region and has taken place after the material exits the die. The likely mechanism for this coarse grain formation is, therefore, a result of a static process. However, since the small, equiaxed grains were observed in both the DMZ and the extrudate surface, the mechanism of their development cannot be concluded based on small – scale extrusion tests alone. A continuous dynamic recrystallization process, possibly geometric dynamic recrystallization (gDRX) likely produces these grains. However, it cannot be ruled out that these smaller equiaxed grains are themselves not statically recrystallized grains formed while the billet remains in the container after extrusion. Additionally, further testing beyond small – scale extrusion tests needed to be performed in order to determine the nature of small, equiaxed grain development in the regions observed. The occurrence of this grain structure during deformation will be further addressed in Sections 5.5 and 6.1.

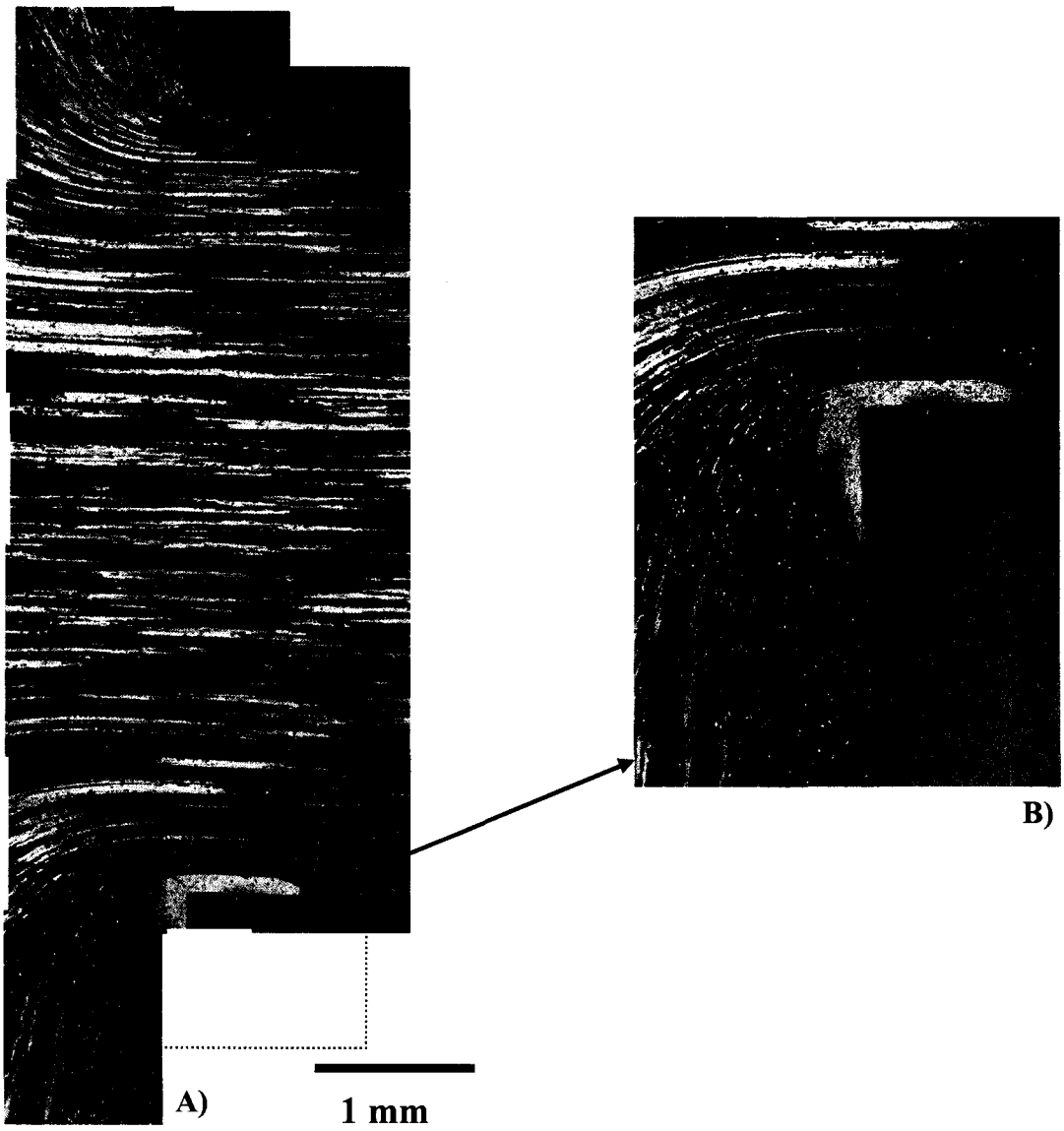

Figure 52: A) Light Optical Micrograph collage of the die exit from small – scale indirect extrusion experiments. B) Magnified view of recrystallized grain at the corner of the die exit growing into the DMZ. The extrusion direction is to the right.

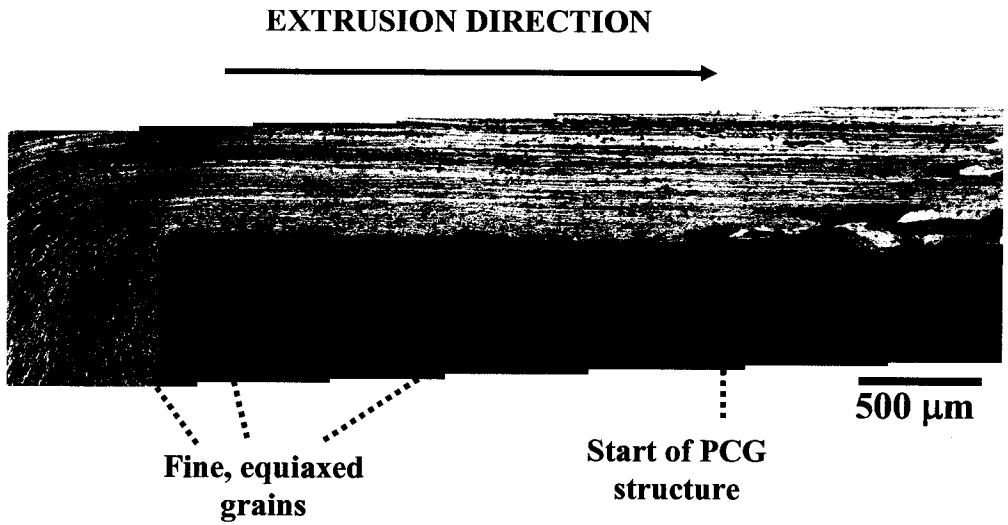

Figure 53: Collage of Light Optical Micrographs taken from the die orifice of partially extruded small – scale extrusion billet 791 with the following extrusion conditions: High Cr 6061 alloy, ram speed = 1.3 mm/s, T_{start} = 400°C, R = 20.

5.2.2.2 Billet Discard – Orientation Imaging Microscopy

In order to characterize the crystallographic texture and provide higher resolution images of the microstructure, EBSD was performed on the billet discard material. There were several distinct regions in the billet discard that are of interest in this investigation. The first is the DMZ adjacent to the face of the die. The resultant orientation and misorientation boundary maps from EBSD performed in this region are shown in Figures 54 A and B. Additionally, the approximate location of the EBSD maps in relation to the partially extruded billet is shown in Figure 54C. The orientation map reveals a highly textured structure in the DMZ made up of relatively small, equiaxed grains. The average grain size within this map of the DMZ was 3.6 μm. The boundary misorientation map also reveals that the region is made up of grains with boundary misorientations higher than 15° and relatively constant size.

EBSD orientation and boundary maps were also generated from the die exit of a partially extruded billet and are shown in Figures 55 A and B. The approximate location of these maps is also shown schematically in Figure 55 C. It can be seen that the small grains from the edge of the DMZ are being pulled into the surface of the extruded product at the die exit. These grains remain relatively equiaxed in shape and are also relatively small, on the order of 2 to 10 microns. The color distribution in the orientation map in Figure 55A suggests that there is progressive change in the crystallographic texture of grains as they are being pulled into the extrudate surface. Further analysis of these different zones of orientation is shown in Figure 56.

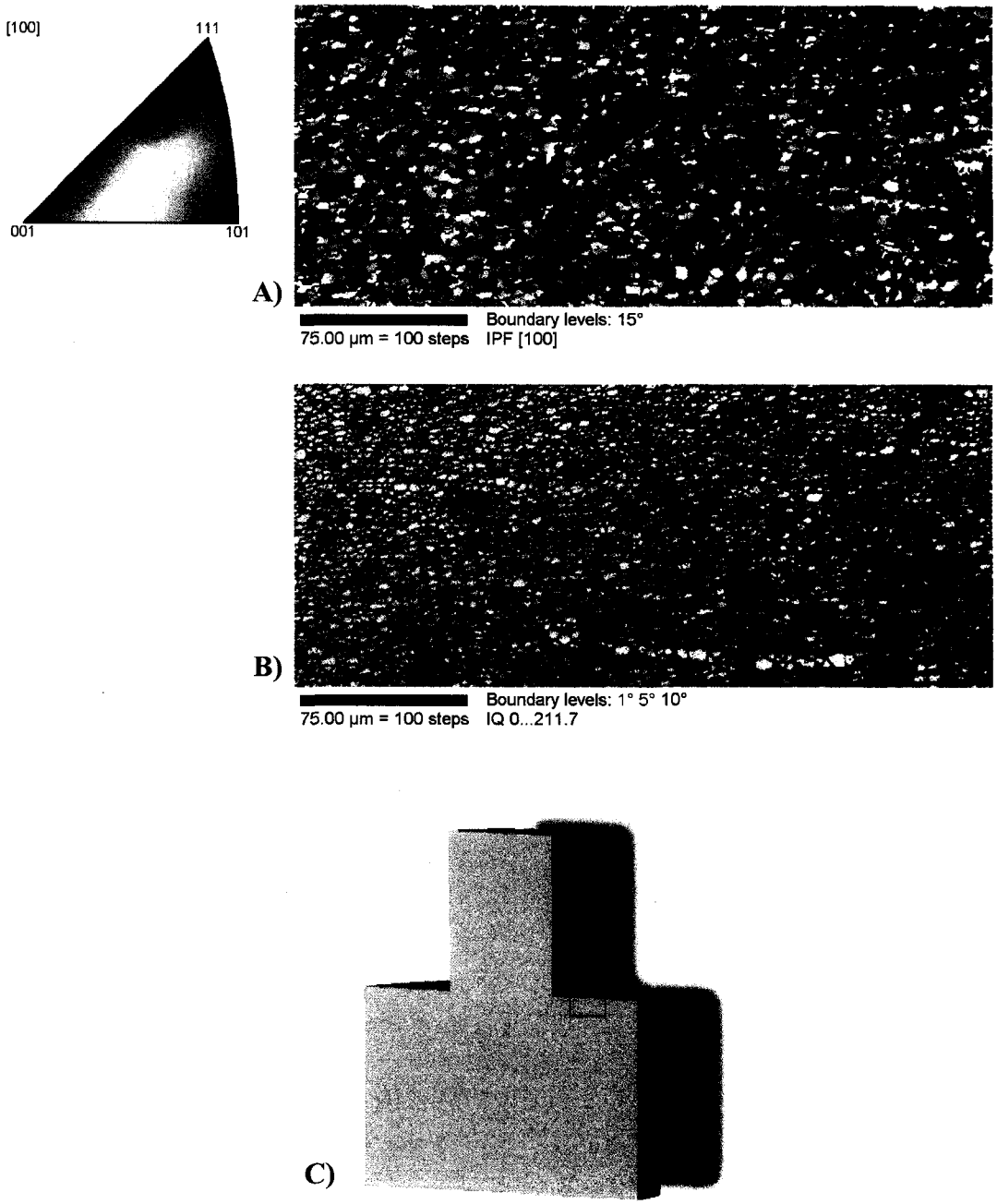

Figure 54: A) EBSD orientation map from the DMZ of partially extruded billet 788. The average grain size is 3.6 µm B) Boundary misorientation map from the same area as A. C) Approximate location within the billet of maps shown in A and B.

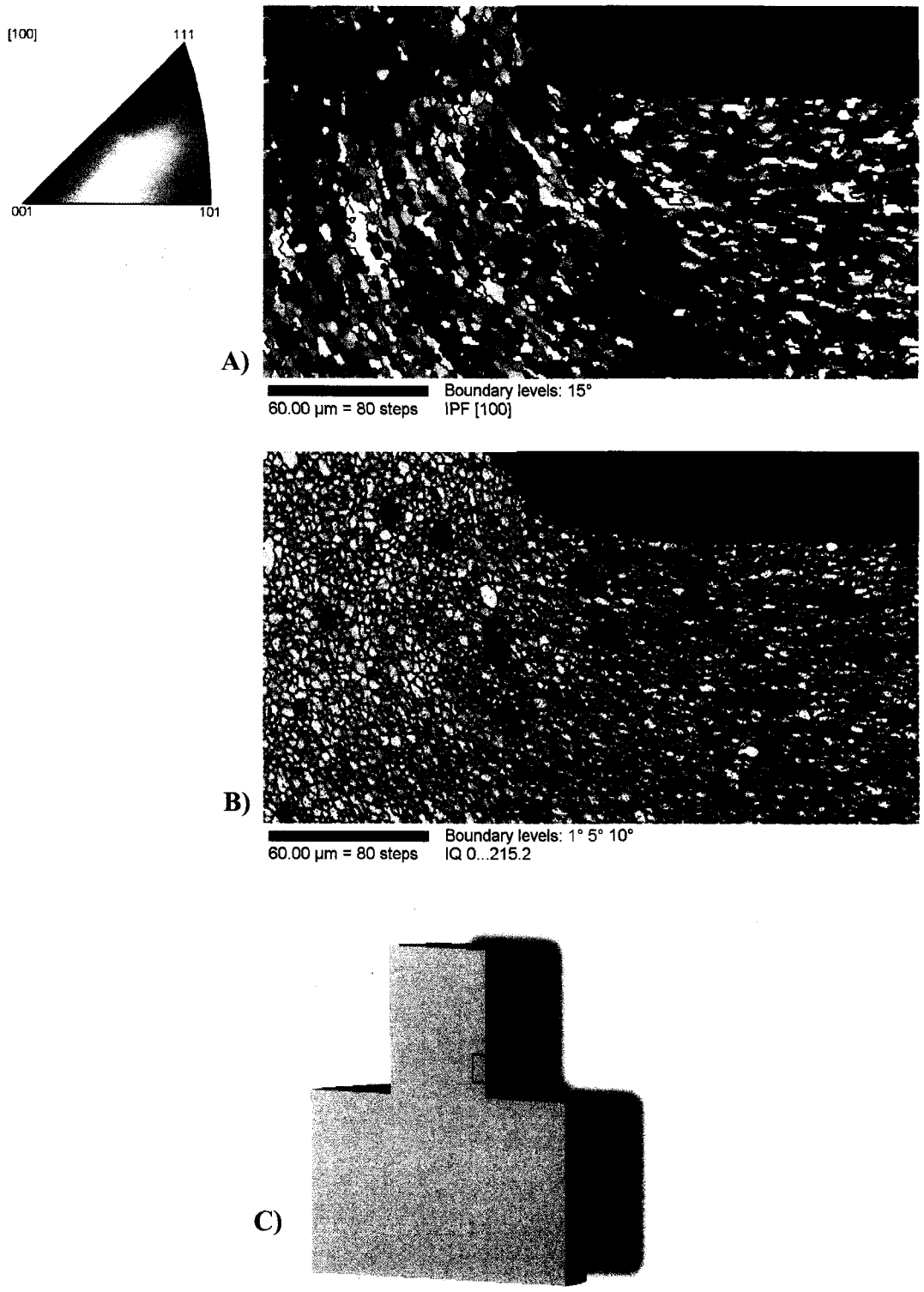

Figure 55: A) EBSD orientation map from die exit of partially extruded billet 788. B) Boundary misorientation map from the same area as A. C) Approximate location within the billet of maps shown in A and B.

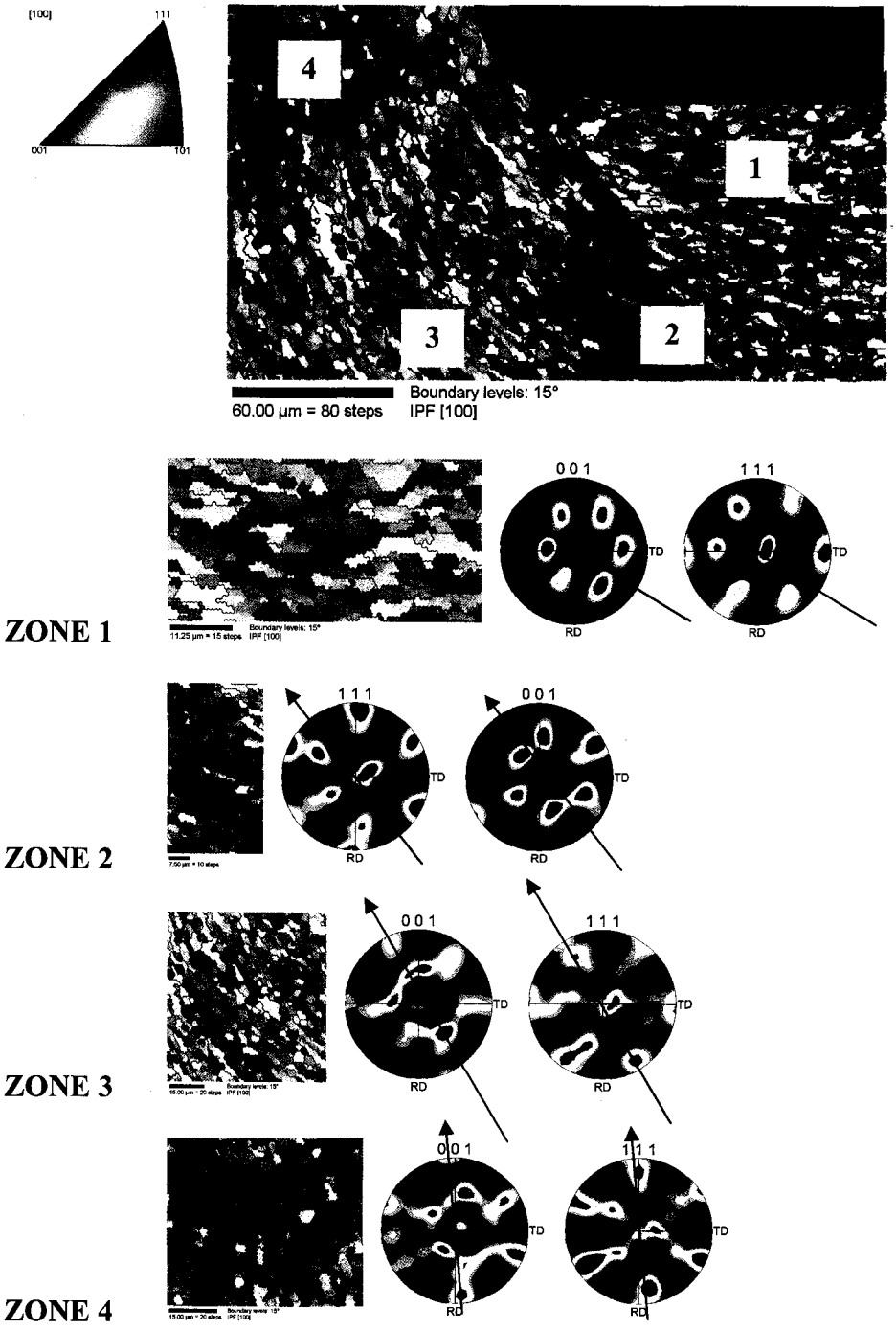

Figure 56: Top – EBSD Orientation map from the extrusion discard of sample 788 showing four distinct zones of crystallographic orientation of the grains. The resultant orientation maps from each zone and their respective pole figures are displayed below it. The orientations of the grains as they are moving into the extrudate surface appear to be rotating to accommodate the extensive shear imposing on them.

As the grains are being deformed in the vicinity of the die exit, it can be assumed that a significant amount of shear will be imposed on these grains. The different zones of crystallographic orientation maps and their resultant pole figures show that the orientation of the grains is gradually rotating around the die exit. In Zones 1 –3, there is a lattice rotation as well as an increase in the strength of the {112}<111> component. When the grains have entered the extrudate surface (Zone 4), they possess a similar texture to those seen at the surface of the extrudates analyzed (Figure 44 – Surface). The Orientation Distribution Function (ODF) in Figure 57 of this surface region confirms that the texture of these grains is Copper {112}<111> type orientation rotated about the Normal Direction (ND). In other words, the {112}<111> type grains have been rotated by approximately 45° about the ND in order to accommodate the large amount of shear stress being imposed on them. The ODF in Figure 57 shows two distinct textures, the first (marked A) has Euler angles of ϕ_1= 55, Φ=27, ϕ_2=45, and the second (marked B) has Euler angles of ϕ_1= 45, Φ=90, ϕ_2=45. These correspond to orientations of {332}<353> and {112}<111>, respectively. Again, it can be reasonably assumed here that the {332}<353> can be characterized as a 45° ND rotated Copper orientation. This orientation makes up a majority of the surface texture in the small – scale extrusion extrudates as well. Evidence of weak Cube {100}<001> and Goss {110}<001> orientations are also seen in the deformed surface texture. The presence of these textures was also found to be the predominant orientations in the coarse grain recrystallized region of the extrudate, characterized in Section 5.2.1.2.

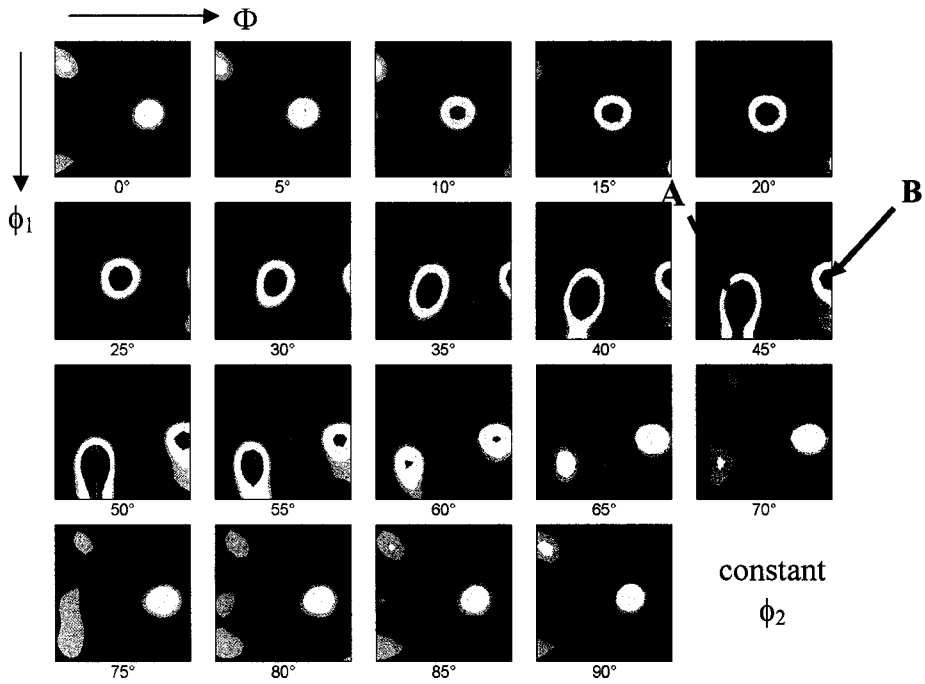

Figure 57: Orientation Distribution Function from the surface of the extrudate of Sample 788. Two main texture components present are A) {332}<353> and B) {112}<111>. Weak Cube {100}<001> and Goss {110}<001> textures also present.

The microstructure of the extrudate beyond the die exit in the small – scale extrusion tests was also characterized via EBSD. In each case of small – scale extrusion tests, the billet discard contained approximately 2 cm of the extrudate. In three cases out of the sixteen small – scale extrusion tests, no PCG was present at the extrudate surface until approximately 1.5 mm from the die exit. Before the PCG structure begins in the extrudate, a relatively homogeneous distribution of small equiaxed grains are also present at the surface of the extrudate (Figure 58). EBSD maps were taken in this region where the material exited the die. The fine, equiaxed nature of these grains provides a large amount of stored energy in the form of high angle grain boundaries.

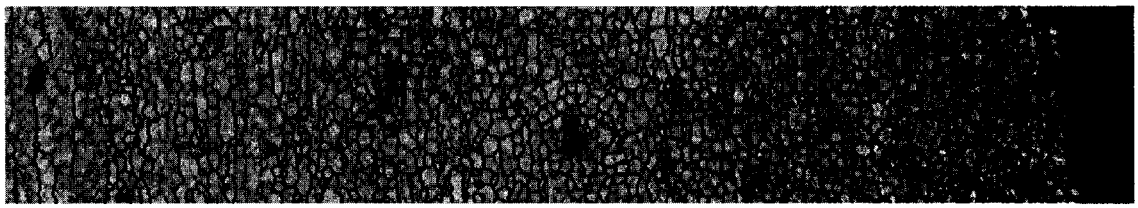

Figure 58: EBSD boundary map at the surface of an extrudate just after exists the die. Notice the collection of small, equiaxed grains at the surface to the right of the figure.

Figure 59 A shows an orientation map from the surface of an extrudate where the PCG grain structure first develops. Figure 59 B is the same area showing boundary orientations of 15° or higher. It can be seen that at the vicinity of the PCG structure, there are small, relatively equiaxed grains. The coarse PCG grain marked 1 here is highly oriented in the extrusion direction, while a few of the equiaxed grains (marked 2) are situated within the larger grain. It can be assumed that the grain marked 1 is all one grain due to the lack of low or high angle grain boundaries separating the orientation.

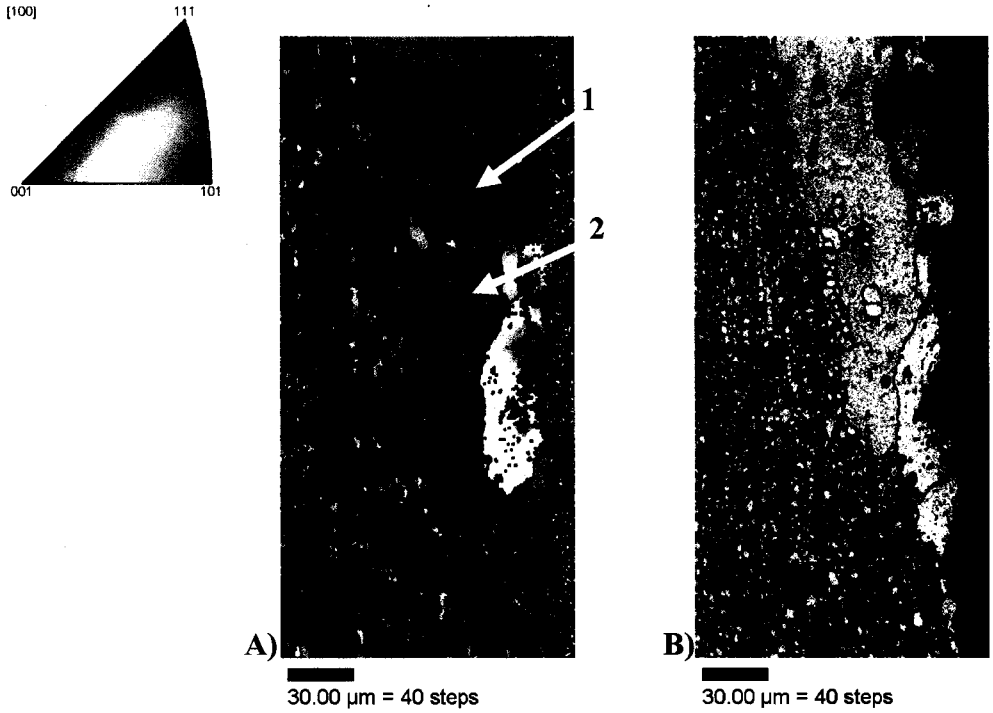

Figure 59: A) Orientation map from the start of the PCG structure in one of three extrudates where the PCG started away from the die exit. Arrows indictate 1) coarse grain highly oriented in the extrusion direction and 2) collection of equiaxed grains surrounded by grain marked 1. B) Same region as A showing boundary misorientations of 15° or higher.

5.3 Industrial – Scale Extrusion

Extrudate material from each industrial extrusion trial was inspected for PCG structure. Only material from each end (front and back) of the extrudate was available for investigation. The locations of sample regions analyzed and dimensions from each end are shown in Figure 60.

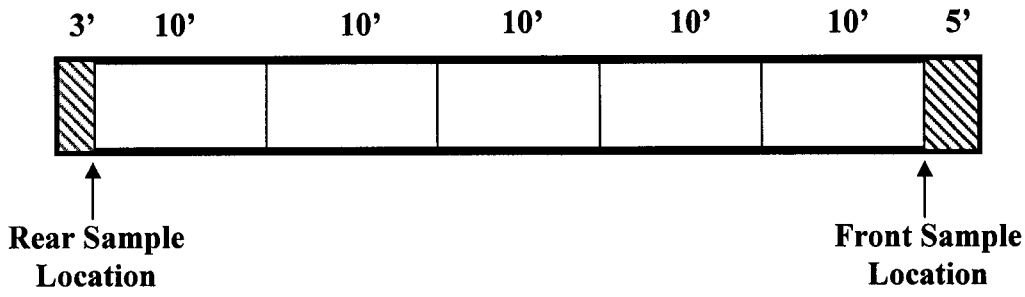

Figure 60: Schematic diagram showing locations of sampled regions and dimensions of each section from the extrudate that are sawed on the run – out table.

LOM micrographs from the front and back of the 12 inch billet's extrudate are shown in Figure 61 A - D. It can be seen that a PCG structure develops at the surface of each extrudate. Additionally, the same increase in grain size from the surface to the center existed as was seen in the small – scale extrusion samples. The grains at the center of the sample had grown to larger than one millimeter in size, as in the case of Figures 61 B and D.

The depths of the PCG structure for different extrusion conditions are shown in Figure 62. In general, the size of the PCG depth increased from the front of the extrudate to the rear. The PCG depth was also larger for the low Cr alloy and 12 inch starting billet size as compared to the high Cr and 8 inch starting billet size. This same effect of chemistry was also seen in small – scale extrusion results as well.

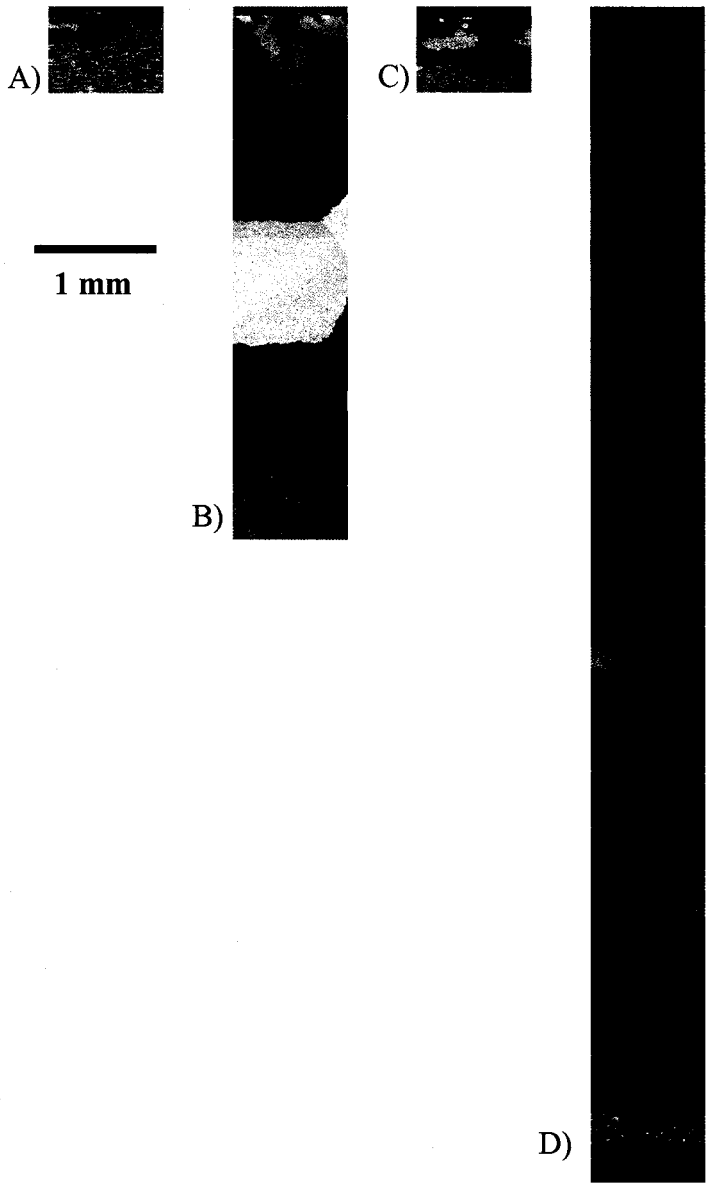

Figure 61: LOM micrographs of the PCG structure for 12" billet industrial extrusion for A) High Cr 6061 front, B) High Cr 6061 Rear, C) Low Cr 6061 Front, and D) Low Cr 6061 Back.

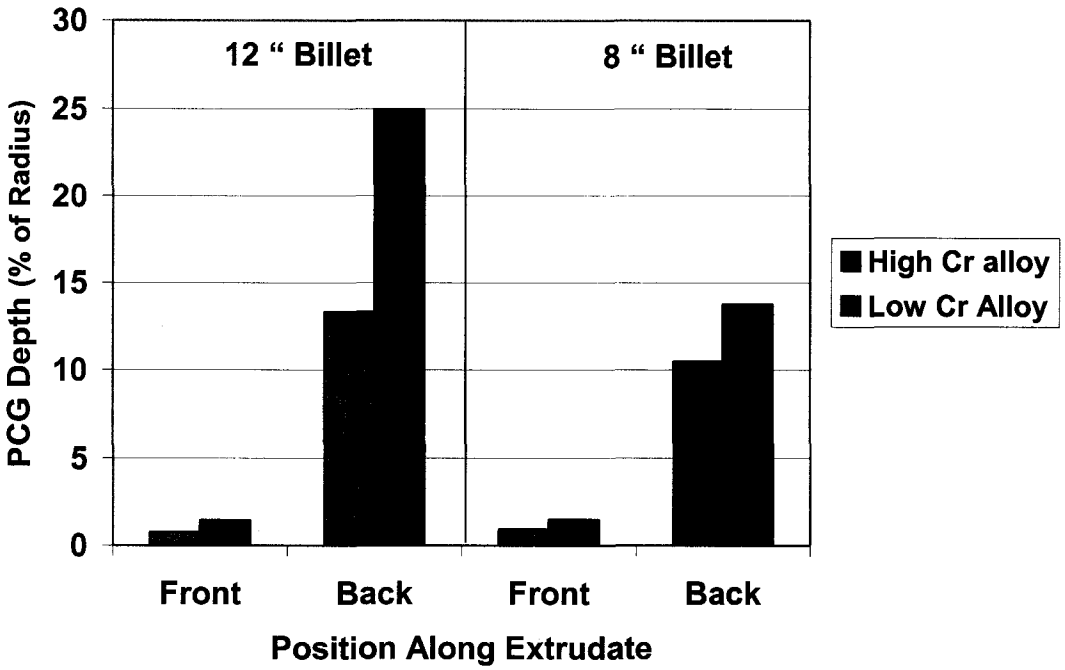

Figure 62: Plot of PCG depth as a percentage of the radius vs. the position along the extrudate for the two alloys studied (6061 High and Low Cr).

While the results do show that there is a distinct difference in the PCG between the two starting billet sizes of the same alloy, the interpretation can be made in many ways. First, the 8 inch starting billet size will result in a smaller diameter extrudate given the same extrusion ratio as the 12 inch starting billet size. Therefore, the quenching effectiveness may have been higher in the 8 inch billet's extrudate and therefore result in a lower PCG depth. Additionally, the extrudates were air cooled for approximately 2 minutes before being quenched in a water bath. Therefore it is difficult to make a direct comparison with the recrystallization kinetics of small – scale extrusion. The negative effect of the shell zone on the depth of the PCG structure cannot be confirmed or denied.

5.4 Numerical Simulation

In order to quantify the extrusion parameters (strain and strain rate) based on small – scale extrusion conditions, Alcoa Technical Center personnel produced numerical simulations. These numerical simulations were produced using the proprietary Finite Element Model (FEM) code FIDAP. A point tracking method was used to determine the evolution of strain and strain rate through the center fiber and surface fiber of case from small – scale extrusion. The conditions used for numerical results are shown in Table XIII. The results from FEM flow analysis are shown in Figures 63 and 64. Figures 63 A and B show the strain at the center and surface fiber. The results of the strain rate are shown in Figures 64 A and B for the center and surface fiber.

Based on these numerical results, it can be seen that the maximum strain can reach close to 3 at the center and above 15 at the surface. The strain rate gradient is even more dramatic, with predicted values of $8s^{-1}$ at the center and close to $40s^{-1}$ at the surface.

Table XIII: Extrusion conditions used in numerical results.

Fiber Location	Temperature (°C)	Extrusion Ratio, R	Ram Speed
Surface	400	40	1.3
Surface	482	40	1.3
Center	400	40	1.3
Center	482	40	1.3

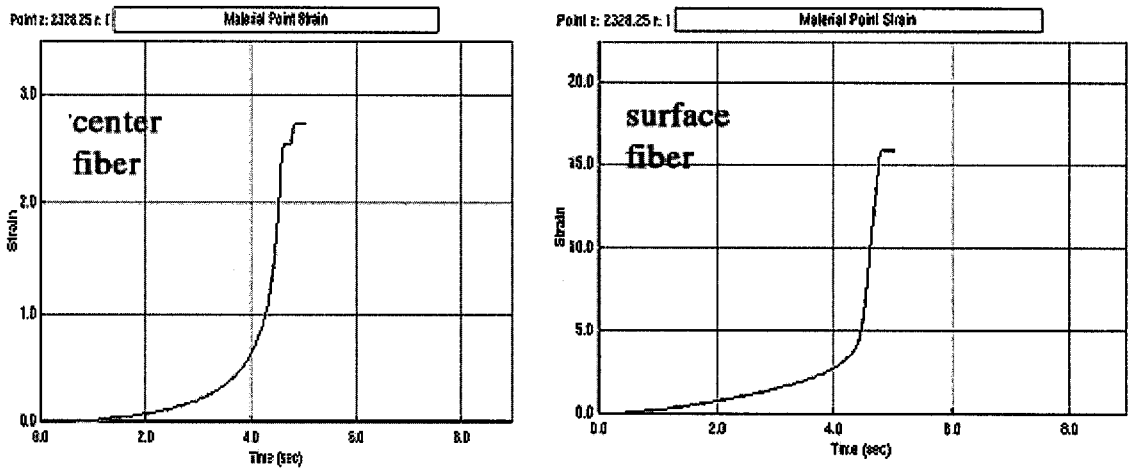

Figure 63: Finite Element Modeling results from Alcoa numerical simulation for the strain at the A) center and B) surface of a small – scale extrusion extrudate [57].

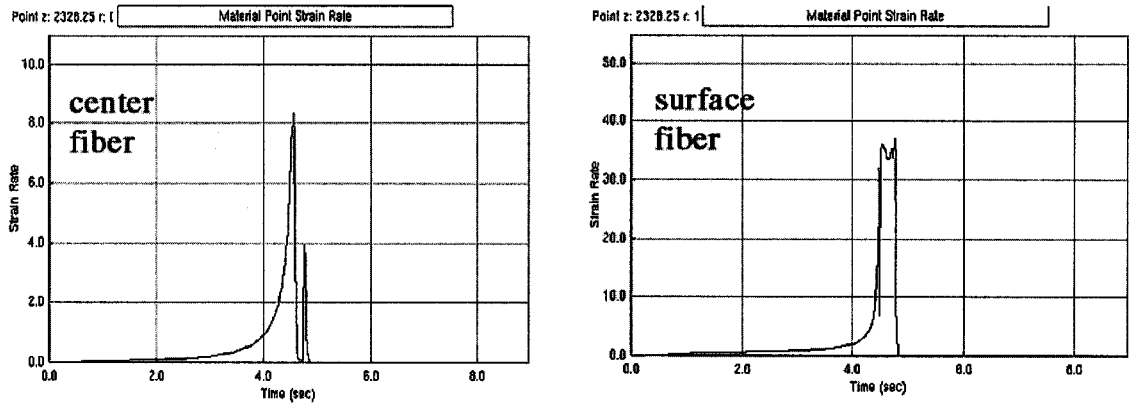

Figure 64: Finite Element Modeling results from Alcoa numerical simulation for the strain rate at the A) center and B) surface of a small – scale extrusion extrudate [57].

5.5 Hot Torsion

5.5.1 Hot Torsion Experimental Trials

A series of experimental hot torsion tests were performed in order to optimize the testing parameters. The material used in these initial experiments was a 6063 aluminum alloy and the material was deformed to $\varepsilon_{eff.} = 5$, $T_{def.} = 482°C$ and strain rate = 20. In order to preserve the deformed structure, the samples were water quenched by spray heads immediately after deformation. It was found that at these deformation conditions, an interesting microstructure resulted. A collage of LOM micrographs from the center (left) to the surface (right) of this sample is shown in Figure 65. Higher magnification images of the center region show deformed grains that have serrated grain boundaries (Figure 66A). At the surface (Figure 66B) the fine, equiaxed grain structure is revealed.

Based on these experimental trials, it was determined that the quenching effectiveness was adequate for the 6061 torsion tests to proceed. However, the maximum strain rate based on the gauge length of 20 mm used in these trials was $20s^{-1}$. Based on the values of maximum strain rate at the surface of the extrudate from numerical simulation results in section 5.4, it was decided that the gauge length should be decreased to 15 mm in order to achieve a maximum strain rate of $30s^{-1}$.

Figure 65: Collage of LOM micrographs from the center to the surface of a 6063 aluminum alloy hot torsion sample. The deformation parameters were $\varepsilon_{eff.} = 5$, $T_{def.} = 482°C$, and strain rate = $20\ s^{-1}$.

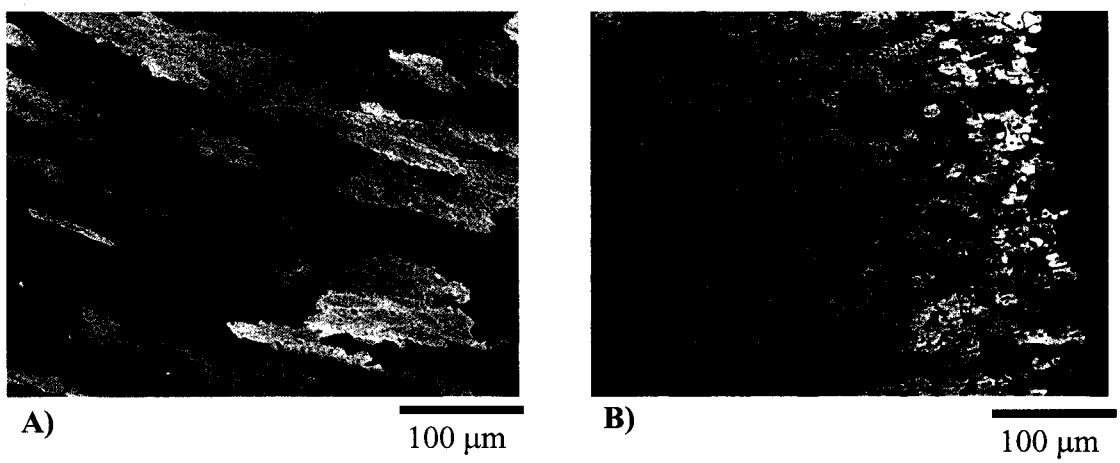

Figure 66: LOM micrographs from the A) center and B) surface of a 6063 aluminum alloy deformed to $\varepsilon_{eff.} = 5$, $T_{def.} = 482°C$, and strain rate = $20s^{-1}$ and water quenched within 1 s of deformation. Notice once again presence of serrated grain boundary structure in the center of the sample and a fine, equiaxed grain structure at the surface.

5.5.2 High and Low Cr 6061

In order to increase the maximum strain rate of the tests, gauge lengths of the hot torsion sample were decreased to 15 mm. The results presented in this section represent the high and low Cr 6061 alloy with the reduced gauge length. Values of torque vs. torsion representing material deformed to $\varepsilon_{eff.} = 2.5$ have been plotted in Figure 67 for the high Cr 6061 alloy and in Figure 68 for the low Cr 6061 alloy. It can be seen that with increasing temperature compensated strain rate, Z, the flow stress increased. Additionally, in Figure 67, the samples deformed at lower values of Z fractured before the strain of 2.5 was reached. The value of Z was determined using equation 3 where values of Q were determined using the flow stress at different strain rates. In each torque vs. torsion plot, a peak flow stress was achieved, followed by a region of flow stress softening. The low Cr 6061 alloy consistently showed lower flow stress values than the high Cr 6061 alloy. This is consistent with the behavior seen in small – scale extrusion tests. The ductility of the two alloys was also markedly different where the maximum effective strain achieved before fracture was 2.75 for the high Cr 6061 alloy and 3.85 for the low Cr 6061 aluminum alloy. The values of maximum effective strain for each alloy were surprisingly low, and it was thought this might be due to poor homogenization. After torsion testing of the same material after further homogenization, similar values for maximum strain were achieved. It is possible that the low strain values are due to the geometry of the torsion sample. The lower fracture strain of the high Cr 6061 alloy also suggests that its ductility is lower than the low Cr 6061 alloy.

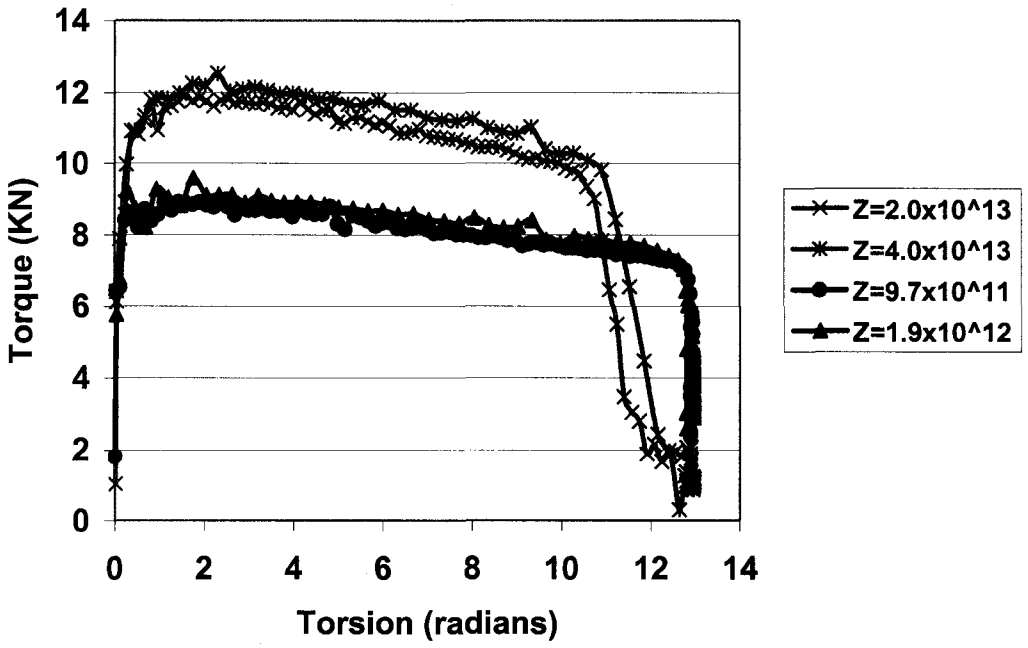

Figure 67: Torque vs. Torsion curves for high Cr 6061 alloy deformed in torsion to an effective strain, $\varepsilon_{eff.}$= 2.5. The deformation temperatures were $T_{def.}$ = 400°C and 482°C and strain rates = 15 and 30. Notice the premature fracture in the tests at high Z.

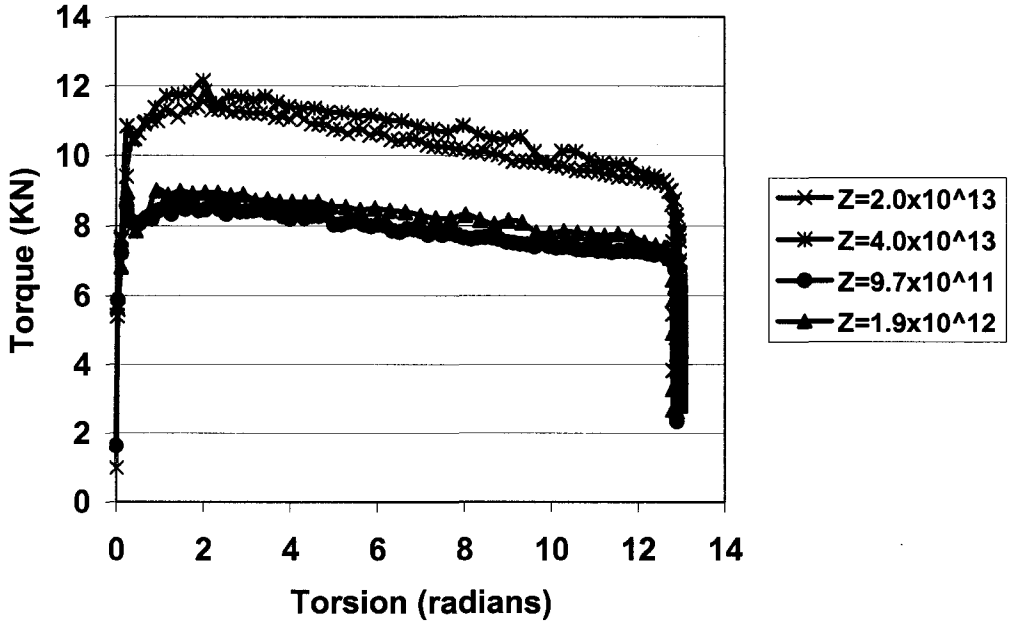

Figure 68: Torque vs. Torsion curves for low Cr 6061 alloy deformed in torsion to an effective strain, $\varepsilon_{eff.}$= 2.5. The deformation temperatures were $T_{def.}$ = 400°C and 482°C and strain rates = 15 and 30.

5.5.2.1 Light Optical Microscopy

Samples from hot torsion were sectioned along the cross – section in order to observe the microstructure at different torsion conditions. A typical case for a sample deformed above an effective strain of 3.5 is shown in Figure 69. A schematic summary of the microstructural features in this sample is shown in Figure 70. In general, it was observed that there were three zones of distinct microstructural features at this strain. At each end of the sample, the grains are relatively undeformed and resemble the original cast and homogenized grains. This region extends inward toward the center of the sample. This is likely due to the constraint between the gauge length material and the remainder of the torsion bar sample. At the surface of the sample, the microstructure was made up of small, equiaxed grains. The shape of this region resembles a hemisphere, where the depth increases from one sample end towards the mid – length of the gauge length. Wedged in between the two regions of small, equiaxed grains is a region of crescent shaped grains. These grains are deformed in the shear direction approximately 45° to the torsion axis. The different regions of the microstructure are relatively symmetrical along the centerline as well as the mid – length. A schematic diagram showing the location of LOM micrographs taken is shown in Figure 71. The R and Z direction have been designated here as the radial and torsion axis, respectively. Figures 72 – 81 represent collages of micrographs from the center to the surface of the sample for each condition.

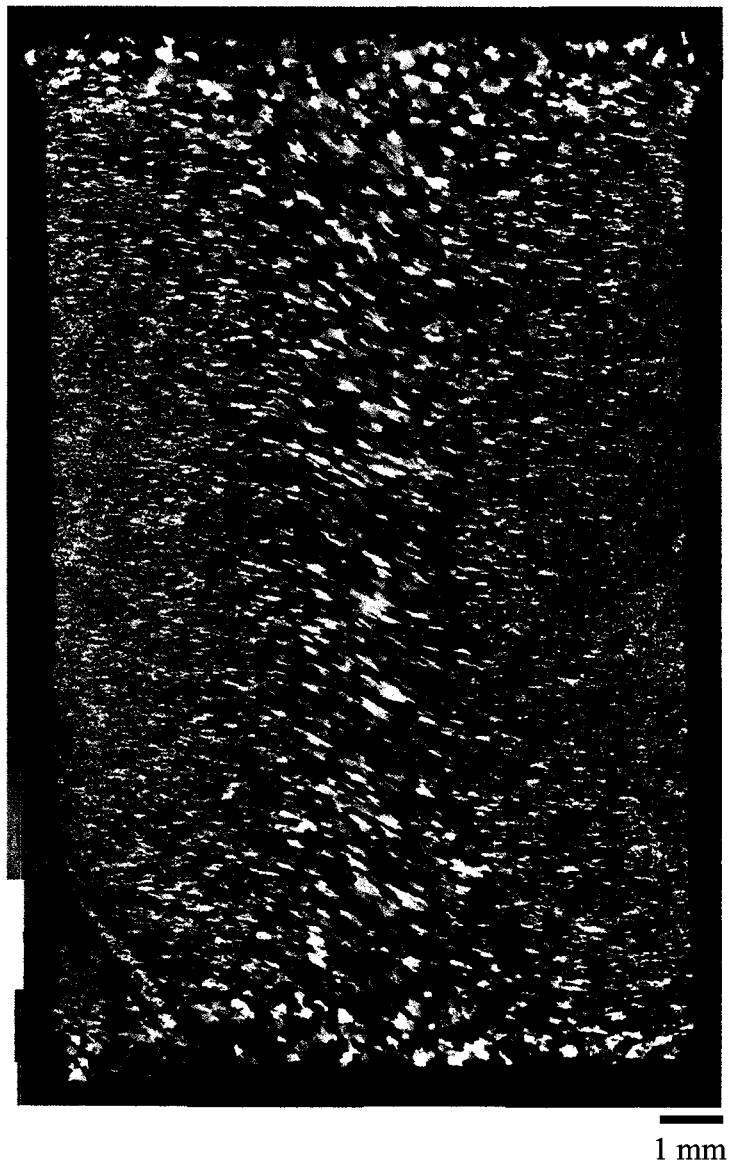

Figure 69: Collage of LOM micrographs from the cross section of a hot torsion sample after deformation. The material and deformation conditions are as follows: 6061 (low Cr), $\varepsilon_{eff.} = 3.5$, and $Z = 9.72 \times 10^{11}$. The scratch at the bottom left of the sample is from the electroetching anode contact.

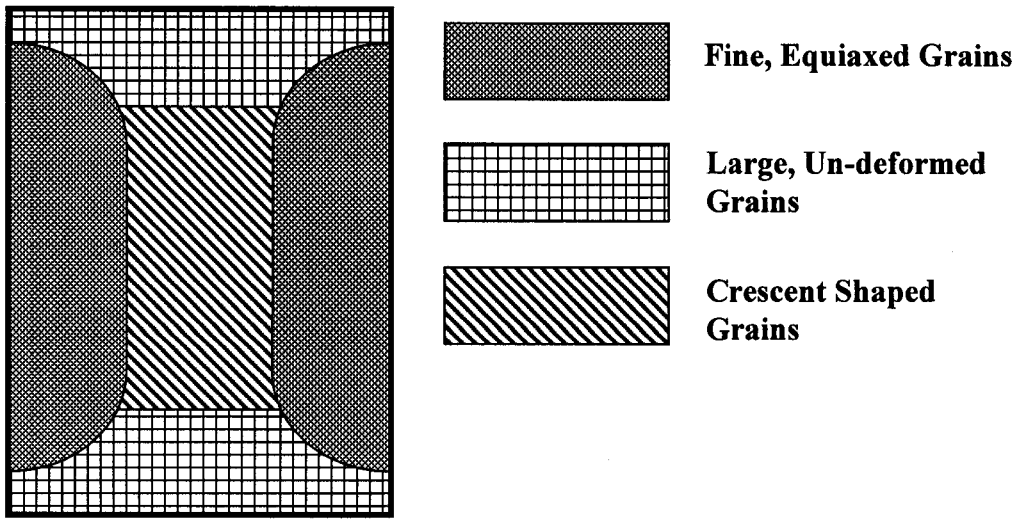

Figure 70: Schematic diagram summarizing three distinct microstructural features in a torsion sample deformed to $\varepsilon_{eff.}$ greater than 3.5.

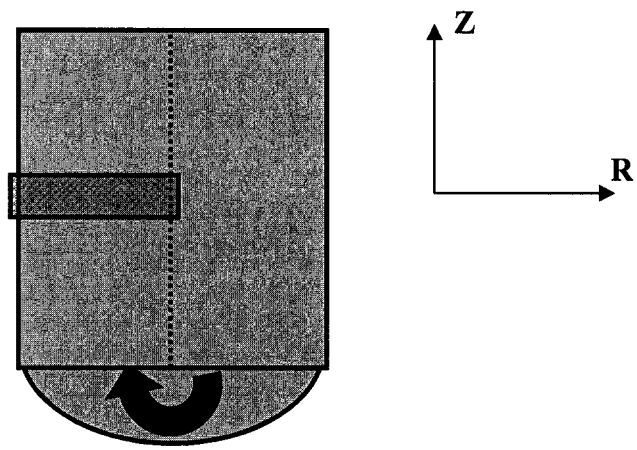

Figure 71: Schematic diagram showing approximate location (shaded box) of micrographs taken from the center to the surface.

Figure 72: 6061 Low Cr hot torsion samples deformed to $\varepsilon_{eff.} = 1$, $T_{def.} = 400°C$, and strain rate of A) 15 and B) 30.

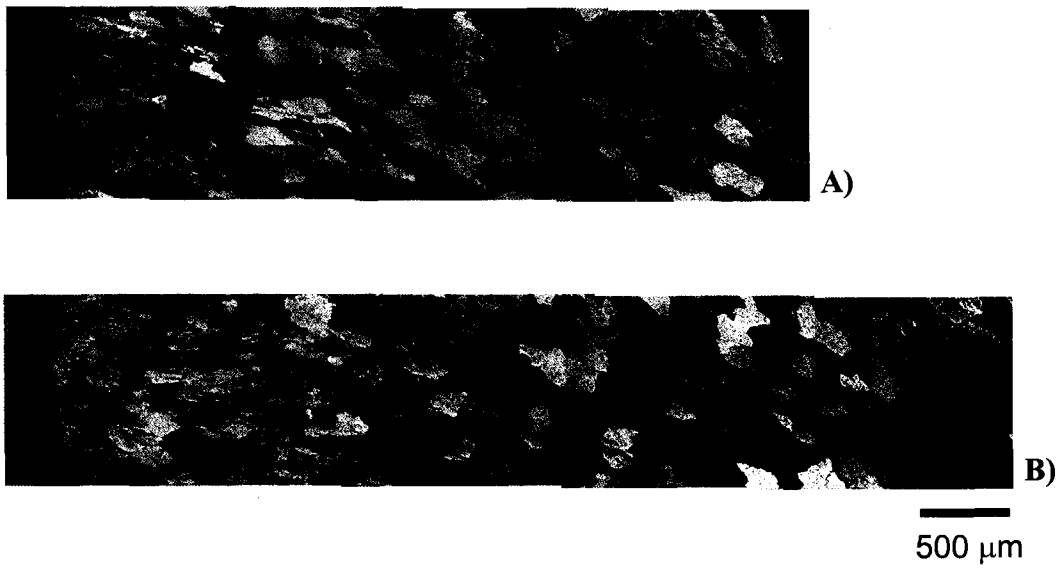

Figure 73: 6061 Low Cr hot torsion samples deformed to $\varepsilon_{eff.} = 1$, $T_{def.} = 482°C$, and strain rate of A) 15 and B) 30.

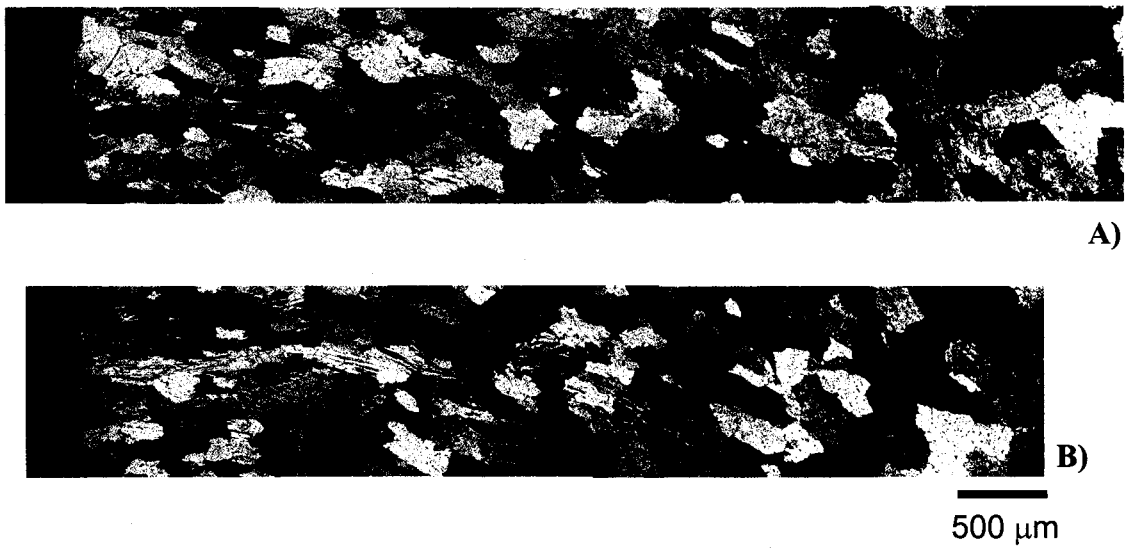

Figure 74: 6061 High Cr hot torsion samples deformed to $\varepsilon_{eff.} = 1$, $T_{def.} = 400°C$, and strain rate of A) 15 and B) 30.

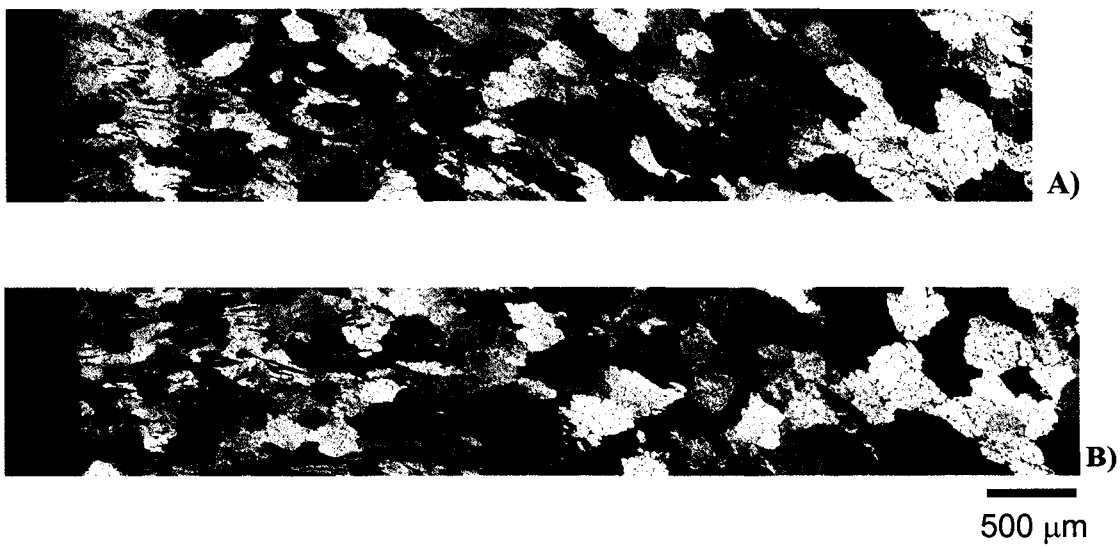

Figure 75: 6061 High Cr hot torsion samples deformed to $\varepsilon_{eff.} = 1$, $T_{def.} = 482°C$, and strain rate of A) 15 and B) 30.

Figure 76: 6061 Low Cr hot torsion samples deformed to $\varepsilon_{eff.} = 2.5$, $T_{def.} = 400°C$, and strain rate of A) 15 and B) 30.

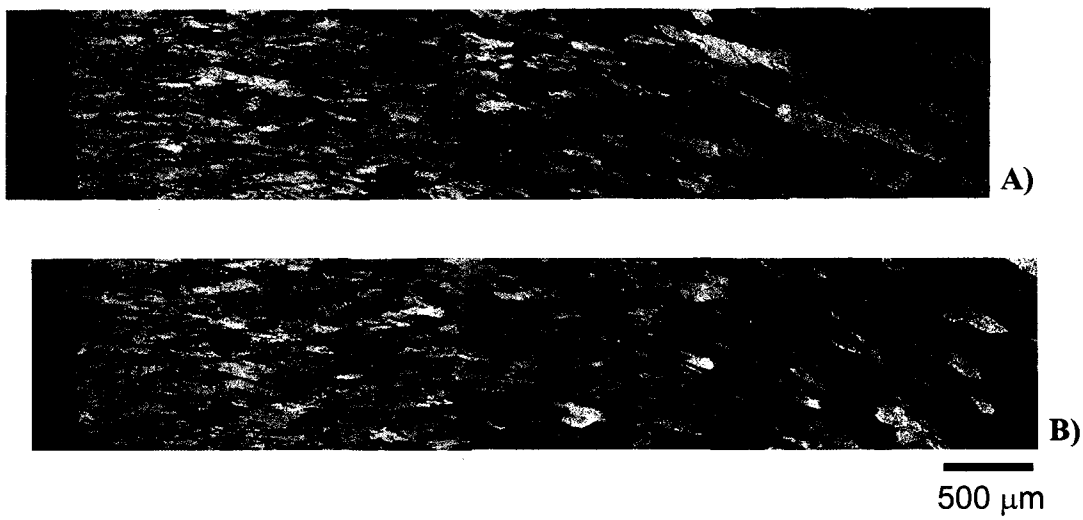

Figure 77: 6061 Low Cr hot torsion samples deformed to $\varepsilon_{eff.} = 2.5$, $T_{def.} = 482°C$, and strain rate of A) 15 and B) 30.

Figure 78: 6061 High Cr hot torsion samples deformed to $\varepsilon_{eff.} = 2.5$, $T_{def.} = 400°C$, and strain rate of A) 15 and B) 30.

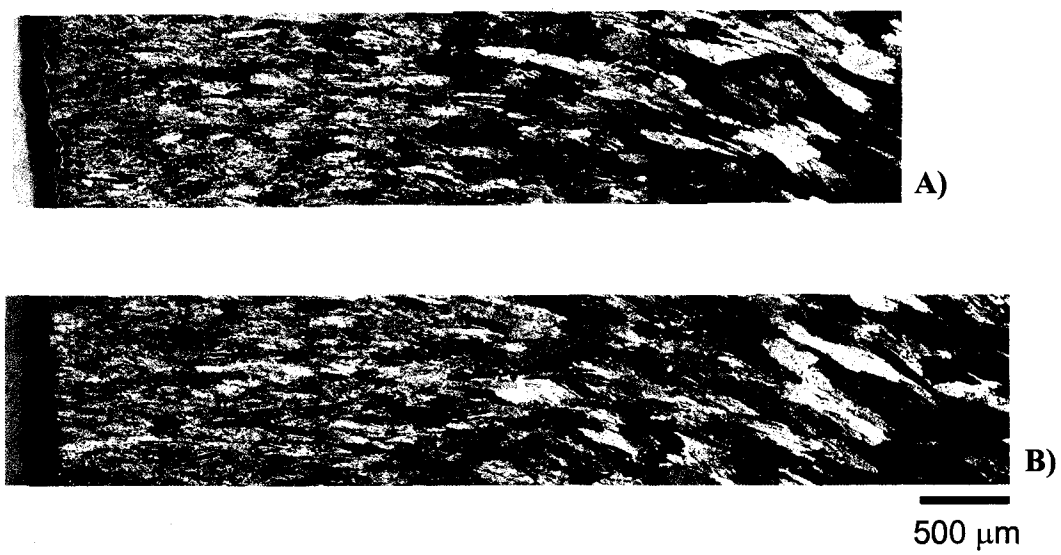

Figure 79: 6061 High Cr hot torsion samples deformed to $\varepsilon_{eff.} = 2.5$, $T_{def.} = 482°C$, and strain rate of A) 15 and B) 30.

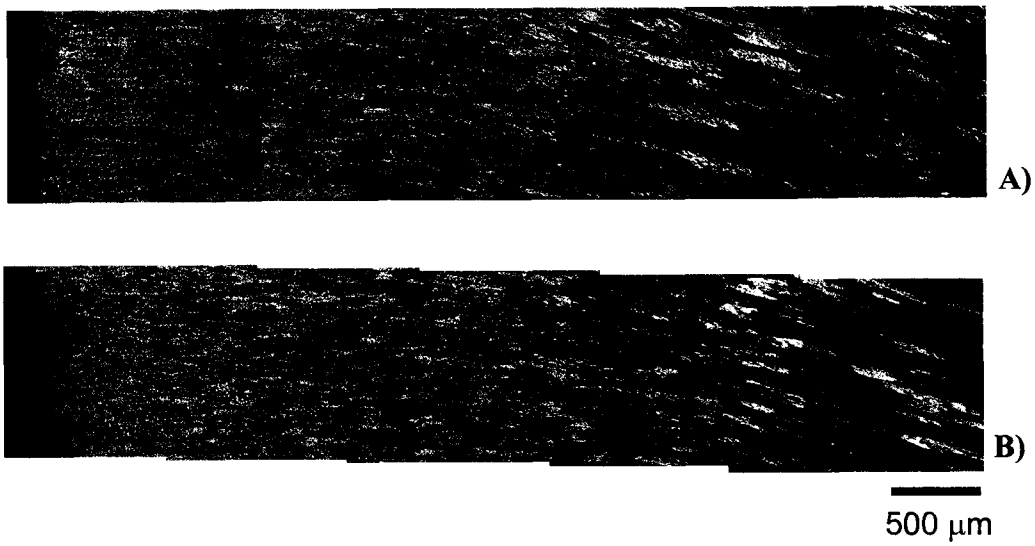

Figure 80: 6061 Low Cr hot torsion samples deformed to $\varepsilon_{eff.} = 3.5$, $T_{def.} = 400°C$, and strain rate of A) 15 and B) 30.

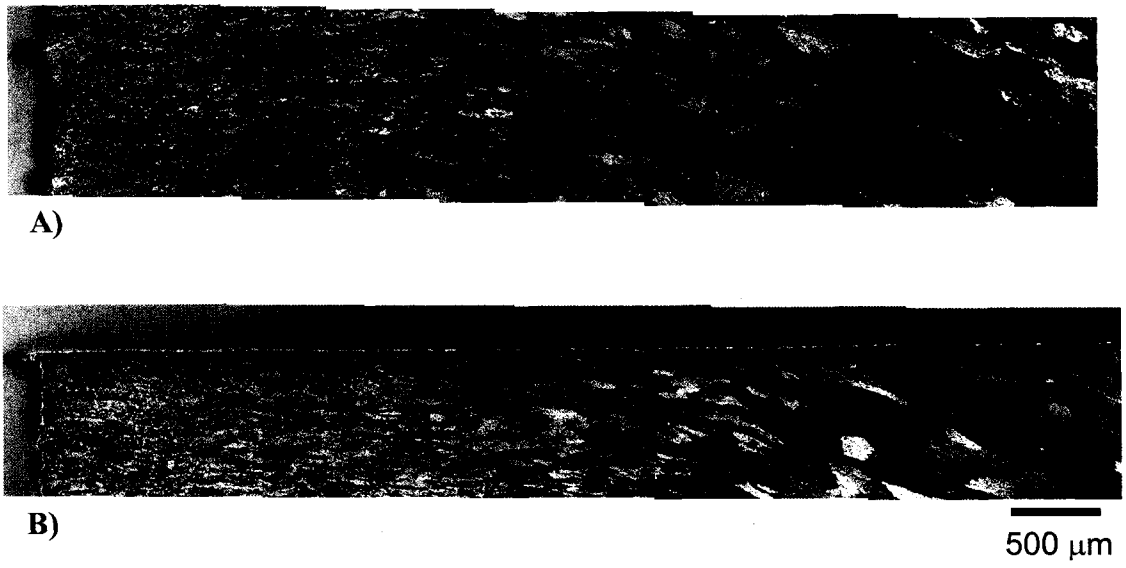

Figure 81: 6061 Low Cr hot torsion samples deformed to $\varepsilon_{eff.} = 3.5$, $T_{def.} = 482°C$, and strain rate of A) 15 and B) 30.

The microstructural results from torsion testing have been summarized in graphical form in Figure 82 for the High Cr alloy and in Figure 83 for the low Cr alloy. The results have been plotted as log Z versus the effective strain. The Z value for each testing condition has been calculated using equation 2. Torsion testing is unique in the sense that high strains can be achieved without the presence of friction. The strain in torsion of a solid bar, however, is not uniform and the microstructural results from this investigation reveal this. For the purposes of this investigation, the microstructure at the surface of the torsion sample at the mid – length is the most important. This is where the maximum strain will be achieved. It should be noted here that, theoretically, the strain along the Z axis of the sample should be zero. However, due to accommodation of the surrounding grains, the grains in the center are being pulled around the torsion axis. Therefore, the central regions appear crescent shaped, rather than simply equiaxed.

Nevertheless, at an effective strain of 1, the grains at the surface of the sample appear moderately deformed with evidence of grain partitioning, especially in the high Cr 6061 alloy (Figures 72 – 73). Grain partitioning can be characterized as long shear bands within a grain that appear to cut it in two. At a higher strain of 2.5, evidence of extensive grain serration and formation of a small, equiaxed grain structure at the surface was noticed (Figures 74 – 75). There was a difference in the characteristics of the grain structure, but both alloys did exhibit a partial fine grain equiaxed structure. The main difference between the two alloys' microstructure was the more diffuse nature of the grain boundaries in the high Cr alloy. Conversely, the low Cr alloy

exhibited a much more structured, yet serrated grain boundary characteristic. Figure 82 shows a plot of the microstructure encountered at the Zener Hollomon parameter vs. maximum strain reached at the surface of the high Cr torsion sample. The maximum strain before fracture was 2.75 in all cases of the high Cr alloy. Therefore, only data for the case of $\varepsilon_{eff.} = 3.5$ are shown for the low Cr alloy in Figure 83. In all of the cases of $\varepsilon_{eff.} = 3.5$, fine, equiaxed grains were present at the surface of the torsion sample. The results suggest that the critical strain in torsion for fine, equiaxed grain formation in these alloys is greater than 2.5.

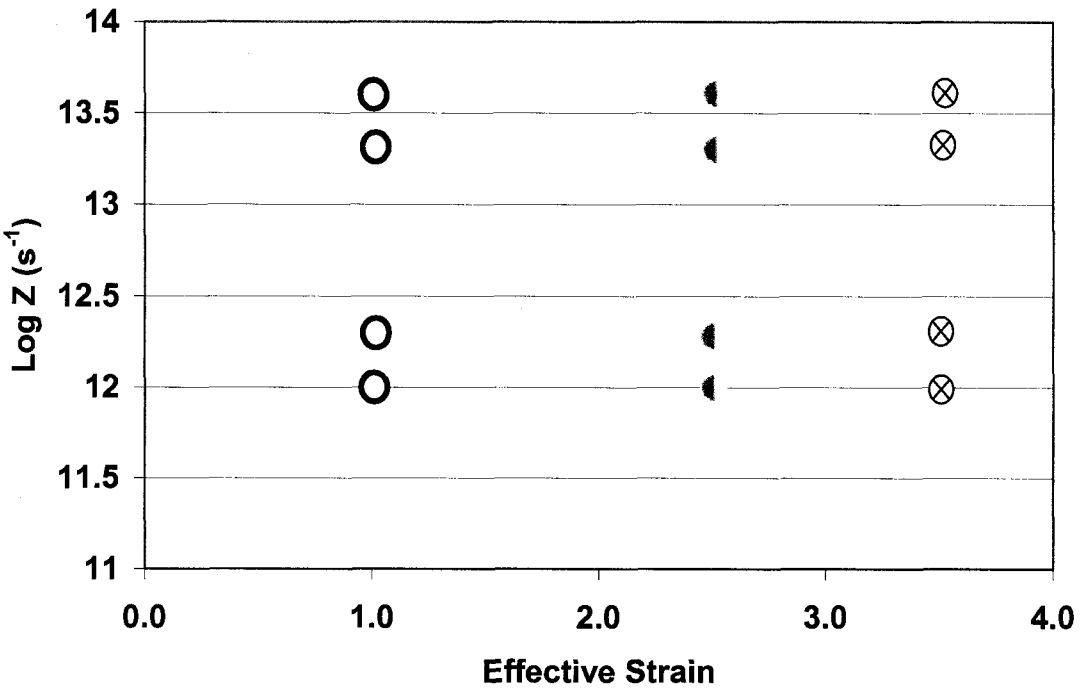

Figure 82: Ln Z vs. Strain for surface of 6061 (High Cr) alloy hot torsion samples. O–No gDRX grains present, ◖ - Partial gDRX development, ⊗ – Sample was fractured.

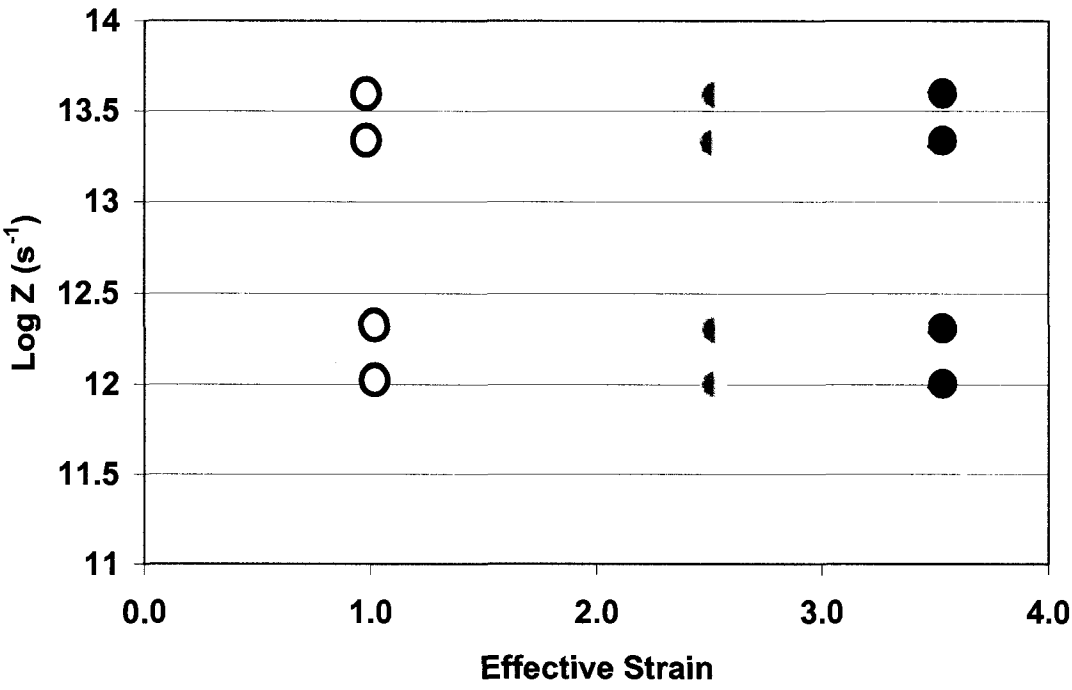

Figure 83: Log Z vs. Strain for surface of 6061 (Low Cr) alloy hot torsion samples. O–No gDRX grains present, ◖ - Partial gDRX development, ● - Complete gDRX development.

While the hot torsion results in this section do provide insight into the critical strain to produce a fine, equiaxed structure, the results cannot be directly compared to small – scale extrusion results at the surface. In Section 5.4, the results of numerical simulation showed that the maximum strain at the center of the extrudate could approach 4 for the case of extrusion ratio 40. Yet, in the case of small – scale extrusion experiments, only minimal fine, equiaxed grains were present at the center fiber. This may be explained by the fact that in torsion, the state of stress at the surface is simple shear. In extrusion, there is a complex combination of plain strain compression and shear that exists.

5.5.2.2 Hot Torsion Orientation Imaging Microscopy

EBSD mapping was performed on two hot torsion samples that represented the highest attainable strain, 3.5, for the low Cr 6061 alloy at a strain rate of 15 s^{-1}. Figures 84 – 85 represent maps from samples deformed at 482°C and Figures 86 – 89 for a deformation temperature of 400°C. Based on the LOM results for these samples (Section 5.5.2.1, Figures 80 – 81), it was determined that a very fine grain structure was present at the surface of both torsion samples, especially at the mid – gauge length. Traditional LOM characterization was not adequate, even at higher magnification, to discern the microstructure. The EBSD maps reveal that in both conditions, $T_{def.}$ = 400°C and $T_{def.}$ = 482°C, that very fine grains are present at the surface. In each figure, the actual surface of the sample is within 20 μm of the right hand side of the scan.

In Figure 84 ($T_{def.}$ = 482°C), the microstructure shown is made of fine, equiaxed grains, as well as two or three grains with substructure, but no high angle boundaries. This lack of high angle grain boundaries can be seen in Figure 85, which is the same mapped region as Figure 84, but only showing boundaries with misorientations of 15° and higher. The grain boundaries also appear to be well defined. The fact that grains with an aspect ratio greater than 1 and contain no high angle grain boundaries, suggests that although gDRX has begun and has consumed a majority of the surface, there still remains some grains that have not undergone enough strain to be classified as gDRX grains. The grain size distribution for this scan is shown in Figure 90.

At the lower deformation temperature ($T_{def.}$ = 400°C), the grain structure is

markedly different, both in size and distribution of the grains (Figures 86 – 89). The grain size is noticeably smaller (Figure 91), and the grains appear much more broken up and serrated than in Figures 84 and 85. The lower temperature of deformation seems to have aided in the restriction of high angle grain boundary movement, thereby creating a higher density of high angle grain boundaries at the same strain as the material deformed at the higher temperature. Finally, Figures 92 and 93 show EBSD Orientation and Boundary maps from the mid – radius of the sample deformed to 400°C. It can be seen that there is an intensive fragmentation of the grain, both at the grain boundaries and within the grains themselves. Here, grains are loosely defined as regions of similar texture, due to the disappearance of a well – defined grain regions. EBSD Orientation and Boundary maps of the mid – radius of the same alloy and deformation conditions are shown in Figures 94 and 95 for the case of deformation temperature of 482°C. It can be seen that the structure is much less diffuse and has more uniform grain boundaries, i.e., less broken up.

In general, it appears that certain crystallographic orientations have developed high angle grain boundaries within them before other orientations given the same strain. Further analysis needs to be performed in order to understand the effect of texture on the deformation characteristics of individual grains.

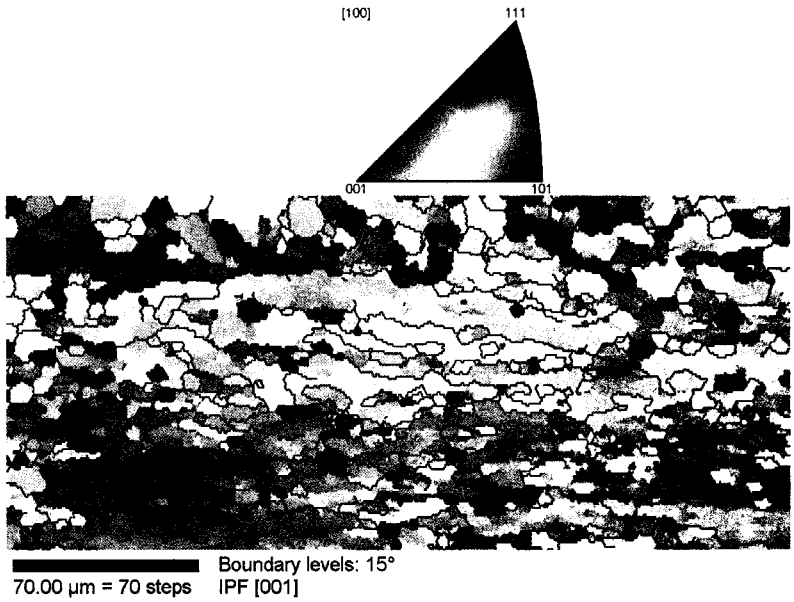

Figure 84: EBSD Orientation map at the surface of the mid – length of the hot torsion sample. The testing parameters were: $\varepsilon = 3.5$, $Z = 9.72 \times 10^{11}$.

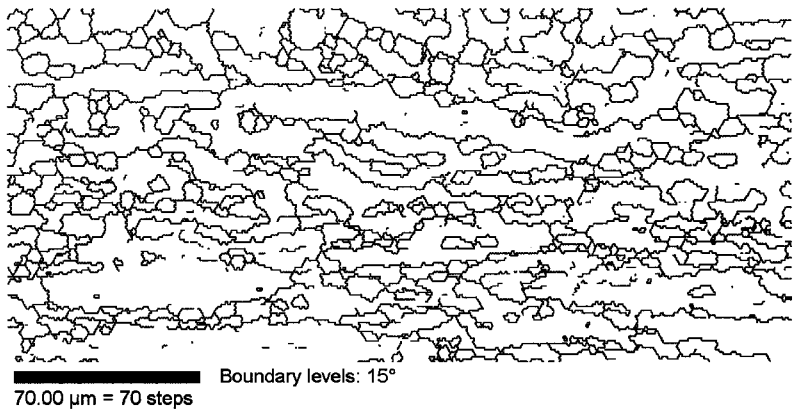

Figure 85: EBSD Boundary map of the same region as Figure 84. The dark lines represent misorientations above 15°.

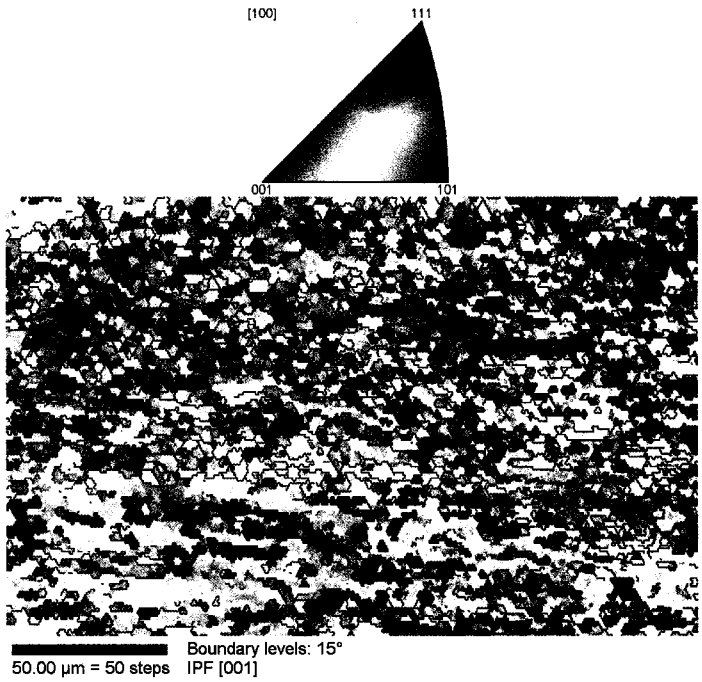

Figure 86: EBSD Orientation map at the surface of the mid – length of the hot torsion sample. The testing parameters were: $\varepsilon = 3.5$, $Z = 2.01 \times 10^{13}$.

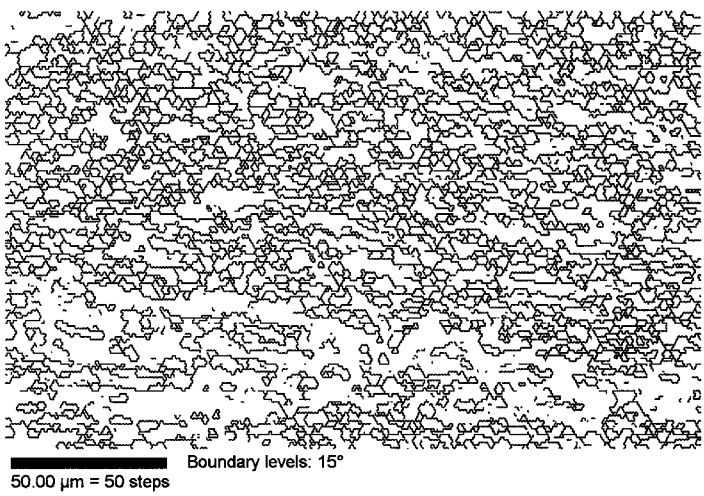

Figure 87: EBSD Boundary map of the same region as Figure 86. The dark lines represent misorientations above 15°.

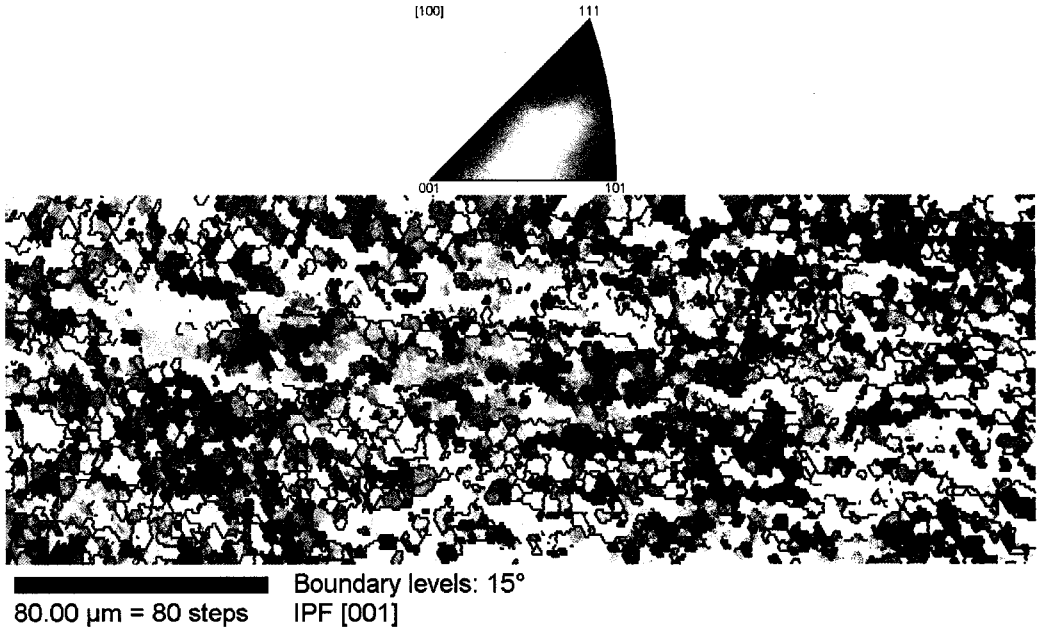

Figure 88: EBSD Orientation map at the surface of the mid – length of the hot torsion sample. The testing parameters were: $\varepsilon_{eff.} = 3.5$, $Z = 2.01 \times 10^{13}$.

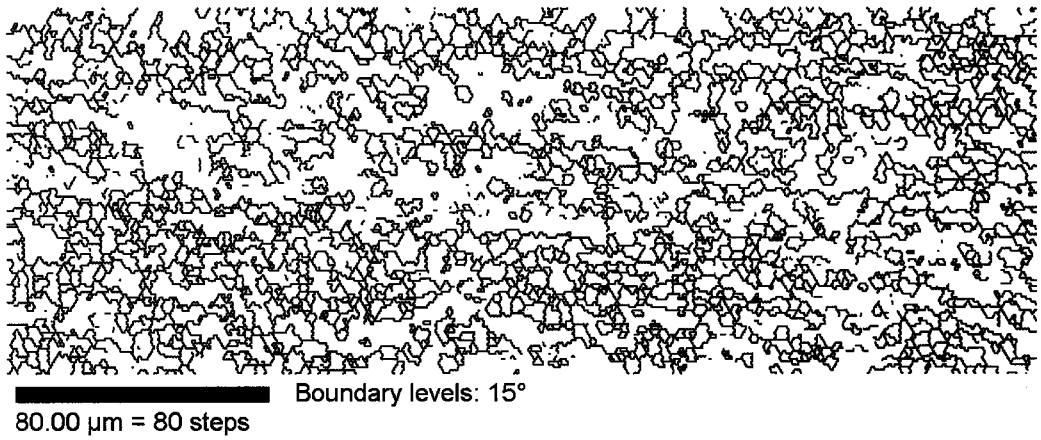

Figure 89: EBSD Boundary map of the same region as Figure 88. The dark lines represent misorientations above 15°.

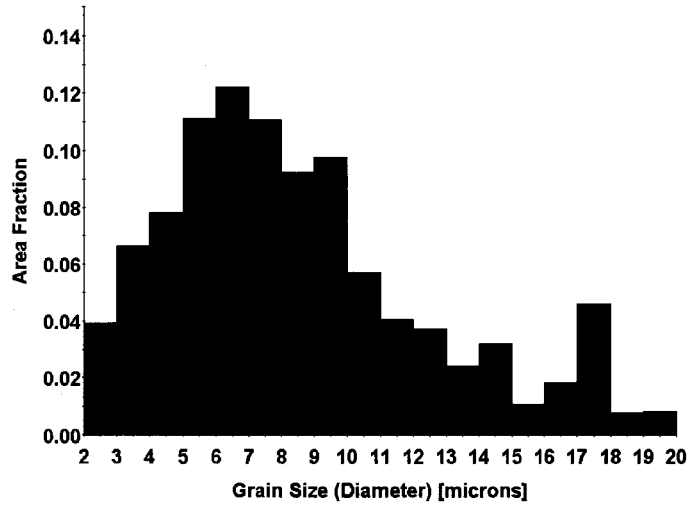

Figure 90: Area fraction of grain size for hot torsion sample deformed to $\varepsilon_{eff.} = 3.5$, Z $= 9.72 \times 10^{11}$. The average grain size for this sample was 6.04 μm.

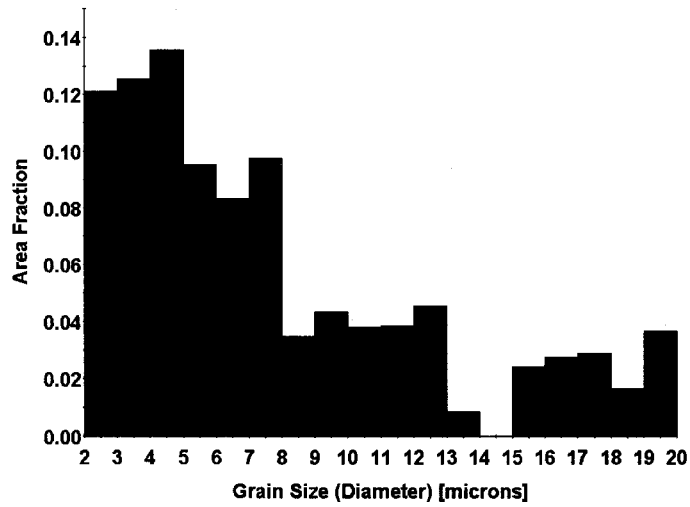

Figure 91: Area fraction of grain size for hot torsion sample deformed to $\varepsilon_{eff.}$, Z $= 2.01 \times 10^{13}$. The average grain size for this sample was 3.78 μm.

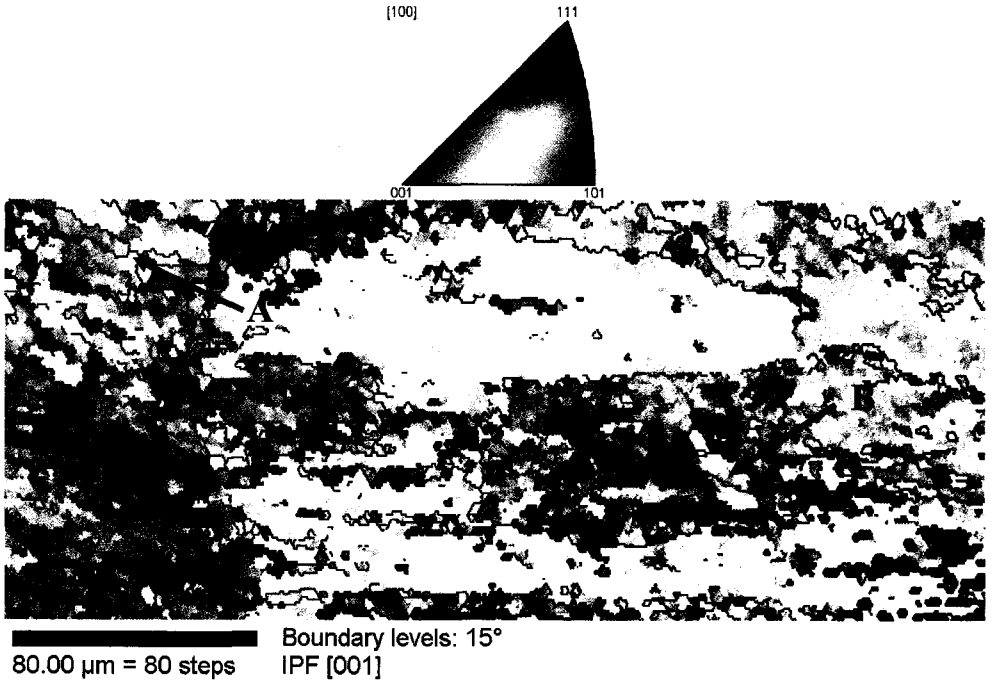

Figure 92: EBSD Orientation map at the mid radius and mid – length of the hot torsion sample. The testing parameters were: $\varepsilon = 3.5$, $Z = 2.01 \times 10^{13}$. Notice the fragmentation of the grains, especially in regions marked A and B.

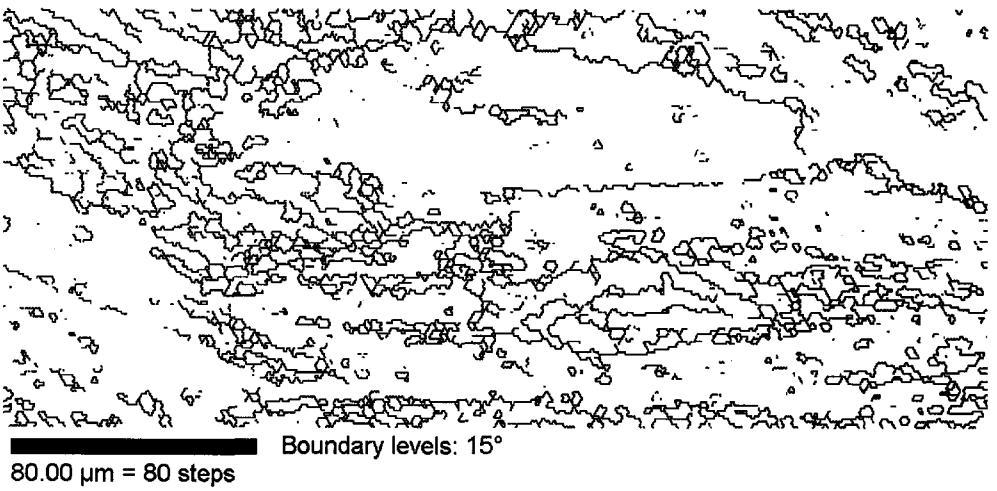

Figure 93: EBSD Boundary map at the mid radius and mid – length of the hot torsion sample. The testing parameters were: $\varepsilon = 3.5$, $Z = 2.01 \times 10^{13}$. Notice the fragmentation of the grains, especially in regions marked A and B.

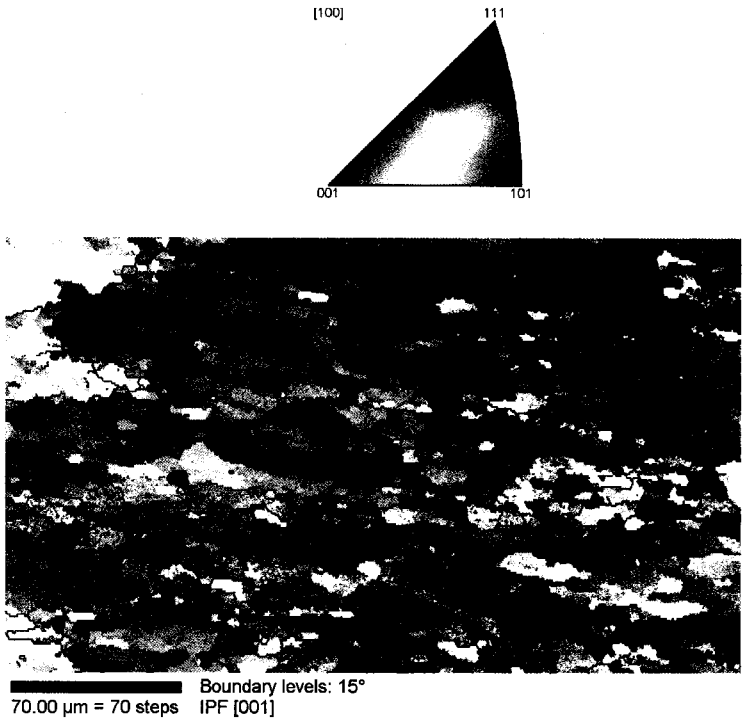

Figure 94: EBSD Orientation map at the mid radius and mid – length of the hot torsion sample. The testing parameters were: $\varepsilon = 3.5$, $Z = 9.72 \times 10^{11}$.

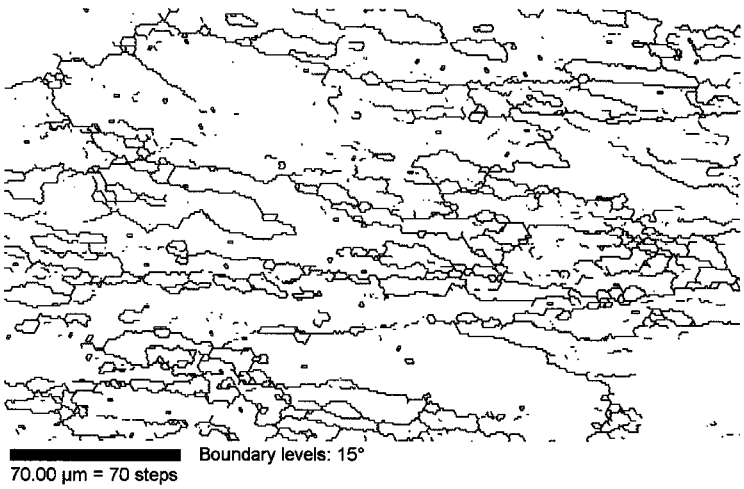

Figure 95: EBSD Orientation map at the mid radius and mid – length of the hot torsion sample. The testing parameters were: $\varepsilon = 3.5$, $Z = 9.72 \times 10^{11}$.

6.0 PROPOSED THEORY OF SURFACE RECRYSTALLIZATION IN EXTRUSION

6.1 As – Deformed Microstructure Following Extrusion and Hot Torsion

Based on the characterization results from small – scale extrusion experiments as well as hot torsion tests, it was seen that there is a presence of large microstructural gradients within the as – deformed material. In both of these tests, a collection of very fine (<10 μm), relatively equiaxed grains was present in specific regions of the microstructure. In small – scale extrusion, these fine grains presented themselves at the surface of the extrudate and within the location of the DMZ region of the partially extruded billet in the absence of coarse recrystallized grains. After performing hot torsion tests to large strains, these fine grains were present along the surface and subsurface at the mid – length of the torsion sample. The nature of this fine grain development has been heavily debated and the exact mechanism and conditions whereby they develop are still unknown [33-36]. Despite the contested mechanism by which these grains are formed, the general appearance of these grains most likely can be attributed to a Continuous Dynamic Recrystallization (cDRX) process. The term continuous is used due to the fact that it appears no nucleation and growth of new high misorientation angle grains has occurred. Instead, a continuous mechanism results in the development of new, high angle misorientation grains. The process known as Geometric Dynamic Recrystallization (gDRX) is one subset in the theory of continuous recrystallization mechanisms. The fundamental theory behind the development of this

structure is slightly different than that of cDRX and has been given in Section 2.2.3.2. In gDRX, the exact mechanism is the development of new, equiaxed grains, not from the progressive increase in the subgrain misorientation, but rather simply the impingement of high angle grain boundaries on the order of the subgrain size. In each case where gDRX grains were encountered, the structure contained very fine grains that were relatively equiaxed in nature. Given the quenching conditions in small – scale extrusion, the presence of fine, equiaxed grains as a result of static recrystallization could not be ruled out without further characterization by Transmission Electron Microscopy (TEM). However, given the rapid quenching technique devised for hot torsion experiments, the likelihood of this fine, equiaxed nature of the grains being produced by a static process is doubtful.

The gDRX theory suggests that there is a critical strain whereby high angle grain boundaries originating from the starting grain structure will become serrated during hot deformation and will pinch off to form new grains. As was shown in Section 2.2.3.2, this critical strain has been related to the Zener Hollomon parameter, Z and expressed as:

$$\varepsilon_c = \ln (Z^{1/m} * D_o) + K \qquad (20)$$

where:
m = strain rate sensitivity exponent
D_0 = original grain size
K = constant

Equation 20 suggests that an increase in Z (decrease in $T_{def.}$) results in a higher critical strain for gDRX to start. This is because the subgrain size at the lower deformation

temperature is smaller, and a higher strain would need to exist before grain boundary impingement occurs. However, there is likely to be a difference in strain rate sensitivity exponent, m, between the two alloys investigated due to the pinning of grain boundaries during deformation in the high Cr 6061 alloy.

The situation becomes complex when one considers that there is little difference between the mechanisms of cDRX and gDRX. For example, in hot torsion, the finer grain structure was present at the lower deformation temperature, $T_{def.}$ = 400°C. It is known that at lower deformation temperatures, cDRX can occur and results in the continuous development of fine, equiaxed grains within a prior high misorientation angle grain. In other words, grain boundary impingement does not need to occur before high angle grains can be produced. Additionally, due to the lower deformation temperature, the subgrain size is much lower than at the high temperature. As the subgrains develop into grains, the final grain size is much lower than at the high temperature. This is in good agreement with the results from hot torsion when the grain size at two different Z parameters are compared in Figures 90 and 91. At the higher deformation temperature (lower Z), a gDRX structure appears to have formed, which results in a higher average grain diameter.

In summary, it appears that the general mechanism of cDRX is in place during deformation of the alloys studied here. This can be stated because new, relatively equiaxed, grains have been formed after deformation to large strains. The exact mechanism, as defined in the literature, appears to be cDRX at low deformation temperatures (high Z) and gDRX at higher temperatures (low Z). This is likely due to

the larger amount of dynamic recovery taking place at the higher deformation temperature. It stands to follow that the same relationship will exist in the low Cr 6061 and high Cr 6061 alloys given the same deformation conditions. The higher Cr content would inhibit high angle boundary movement during deformation and thereby cause the critical strain for gDRX to increase. While this behavior is likely, it could not be confirmed because a uniform presence of gDRX grains could not be compared with the low Cr alloy due to the fracture before $\varepsilon_{eff.} = 3.5$ was reached in torsion testing. Due to the uncertainty in the exact mechanism for fine, equiaxed grain development, the precise equation to determine the critical strain for their development will likely be different than equation 20.

6.2 Abnormal Grain Growth Following Hot Deformation

Throughout the course of this research, there has been evidence that suggests abnormal grain growth has occurred following hot deformation. The key indication of abnormal grain growth is the existence of grain size distributions that appear bimodal. For example, in Figure 96, the as – deformed microstructure following hot torsion of a 6063 aluminum alloy is shown. The material used in this testing was quenched with water at a rate of greater than 380°C/s following deformation, so it can be reasonably assumed that minimal, if any, post – deformation recovery or recrystallization occurred. The microstructure is made up of very fine, equiaxed deformed grains, presumably formed by a cDRX or gDRX mechanism. In Figure 97, the same 6063 alloy at the same location within the deformed torsion sample is shown after deformation without

water quenching, but rather slowly cooled at a rate of approximately 6.5°C/s. The exact cooling rate is not known because the thermocouple was lost due to the high strain rate imposed.

The fine, equiaxed grain structure can still be seen, and is being consumed by very large, irregularly shaped grains. It is assumed here that the mechanism by which the larger grains have formed is via an abnormal grain growth process.

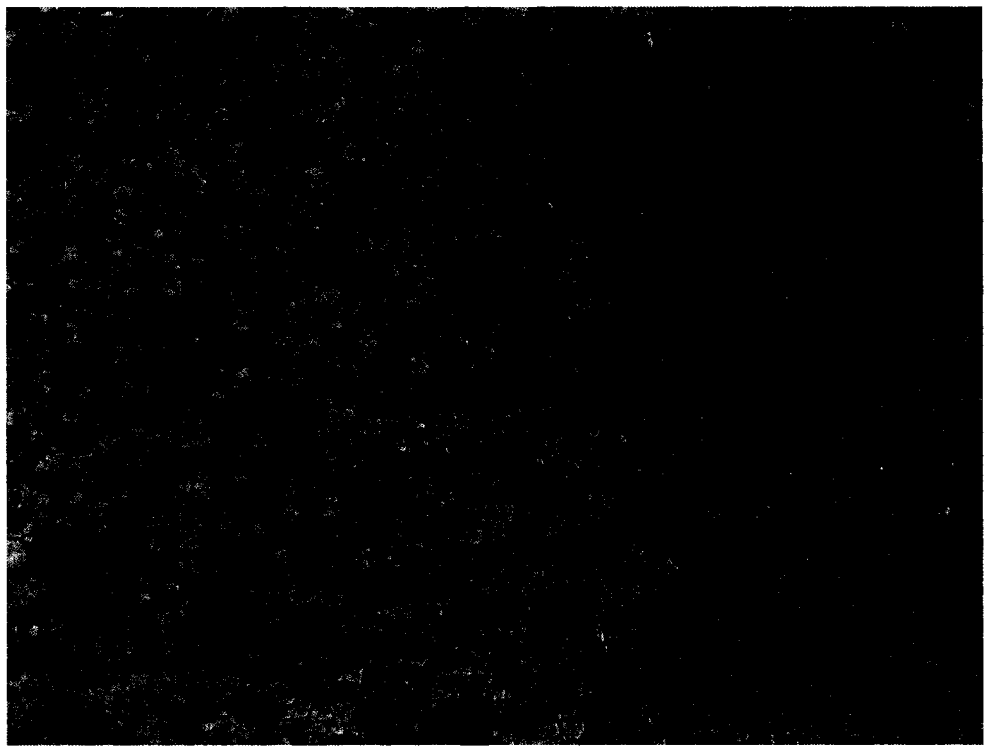

Figure 96: LOM micrograph at the subsurface of a 6063 aluminum torsion sample that was water quenched. The cooling rate was approximately 380°C/s.

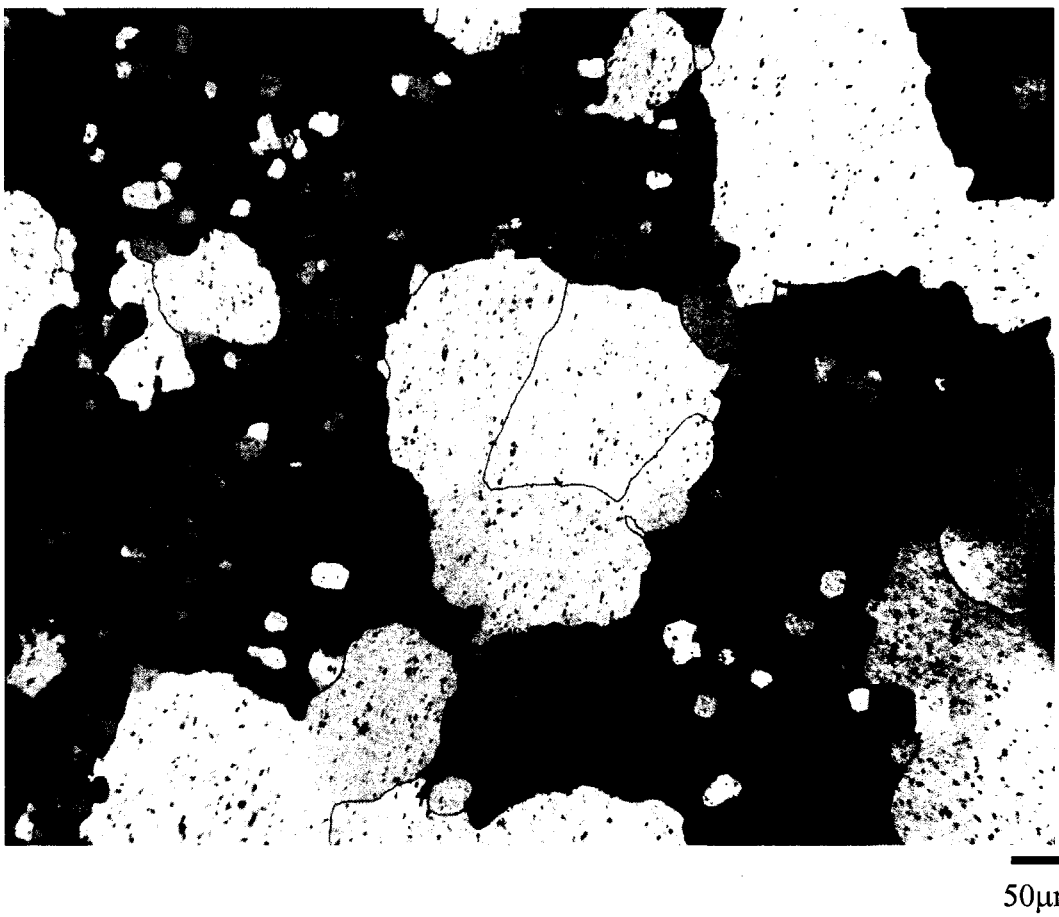

Figure 97: LOM micrograph showing abnormal grain growth in a 6063 torsion sample that underwent slow cooling after deformation (no water quench). The cooling rate was approximately 6.5 °C/s.

Another example of abnormal grain growth following deformation is seen in Figure 98 for the case of the extrusion sample 783 at the die exit. It was found that these abnormally growing grains grew primarily at the region closer to the boundary between the DMZ and fibrous/banded microstructure in the main deformation zone. In the extrudates characterized, evidence of abnormal grain growth was also encountered. Figure 99A is an EBSD orientation map of sample 788 extrudate's surface and Figure 99B is the same scanned region, but showing grain boundary misorientations of 15°

and higher. Again, in this case, the billet was left inside the container for approximately 60s after deformation and then water quenched to room temperature. The exact cooling rate while the material was left in the container could not be determined. The grains marked by arrows indicate grains that have a high pattern quality indicating they are recrystallized grains. EBSD pattern quality depends on the structure of the material. Deformed material will yield a lower pattern quality and fully annealed or recrystallized material will yield the best pattern quality. Additionally, these grains appear to be larger than the average grain size surrounding it. A similar case is shown in Figures 100 A and B for the same extrusion sample 788. Again, the growing recrystallized grain is marked by arrows in the both the orientation map and boundary maps.

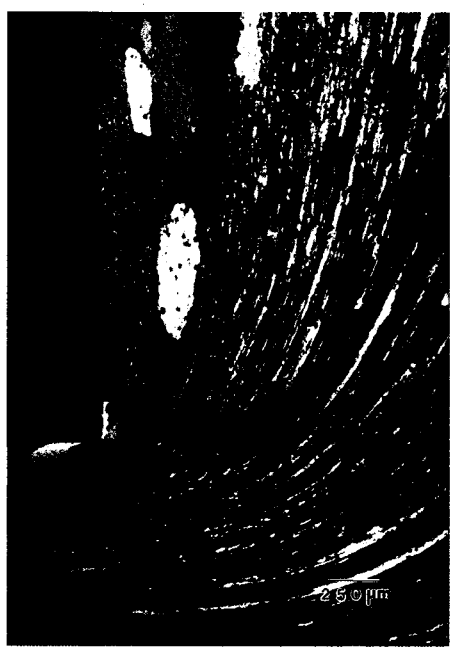

Figure 98: LOM micrograph from the die exit region of sample 783 billet discard showing coarse grain formation in the DMZ region. Note that the coarse grains are primarily growing close to the DMZ interface with the banded/fibrous grain microstructure.

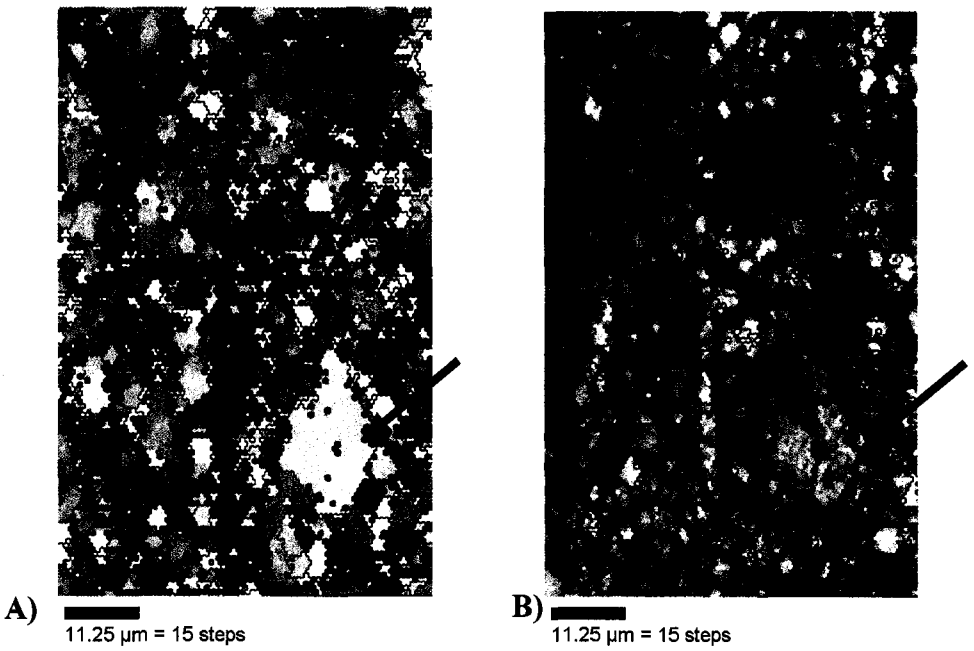

Figure 99: A) Orientation map from surface of extrudate 788 as it exits the die. B) Same region as A with boundary misorientations of 15° or higher in black. The grain marked by an arrow is presumably a recrystallized grain and has a diameter, D of 14μm. The $D_{avg.}$ of this map is 2.1μm.

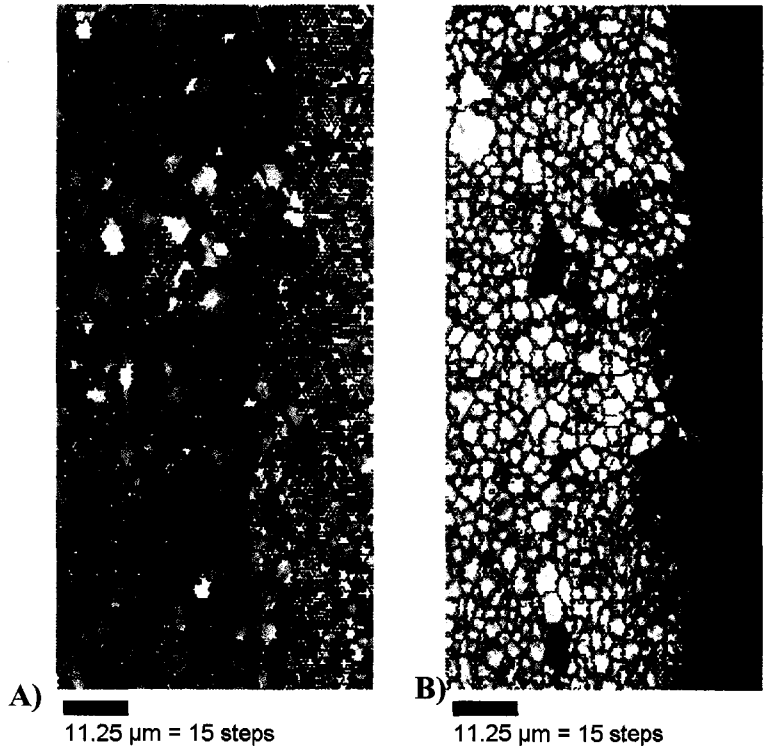

Figure 100: A) Orientation map from surface of extrudate 788 as it exits the die. B) Same region as A with boundary misorientations of 15° or higher in black. The grain marked by an arrow is presumably a recrystallized grain and has a diameter, D of 10μm. The $D_{avg.}$ of this map is 2.5μm.

6.3 Abnormal Grain Growth Theory in a Grain Assembly

The literature which comments on the annealing mechanisms as they relate to the PCG structure is based on traditional nucleation and growth mechanisms and kinetics. The results of this investigation have shown that coarse grain recrystallization on the surface can form very quickly, within a matter of seconds after the material exits the die orifice. A summary of the traditional theory of PCG structure development in a generic high stacking fault energy aluminum alloy is shown in Figure 101. In this sequence, the material used in extrusion is typically cast and homogenized and contains

an equiaxed grain structure (Figure 101a). As deformation progresses, the grains flatten or elongate, depending on the state of stress and imposed strain (Figure 101b). As the strain increases further, a fibrous, or banded structure develops, and the subgrains have a constant mean misorientation, size and dislocation density (Figure 101c). This is all based on the fact that the material has reached steady state deformation, as per Figure 6 from Section 2.2.1. Once the deformation ceases and the material exits the die, static annealing processes are active and act to lower the stored energy in the material (Figure 101D). This stored energy may be reduced by any number of mechanisms, such as Particle Stimulated Nucleation (PSN), Strain Induced Boundary Migration (SIBM), or subgrain coalescence. If one uses the premise that the PCG structure is produced via an abnormal grain growth process, a recrystallized grain assembly must first be made, which is comprised of high angle grain boundaries that have consumed the deformed structure. The statically recrystallized structure is shown in Figure 101E. If this was to occur, then abnormal grain growth can only occur when the particle dispersion, in this case fine Al(Cr,Mn)Si particles, would pin the high angle grain boundaries, which allows a special grain in the assembly to grow to a significant size (Figure 101F). In other words, the process by which abnormal grain growth would occur after deformation would need two acts to occur in succession. The first is nucleation and growth of the new statically recrystallized grains, and second, abnormal grain growth consuming the other smaller grains.

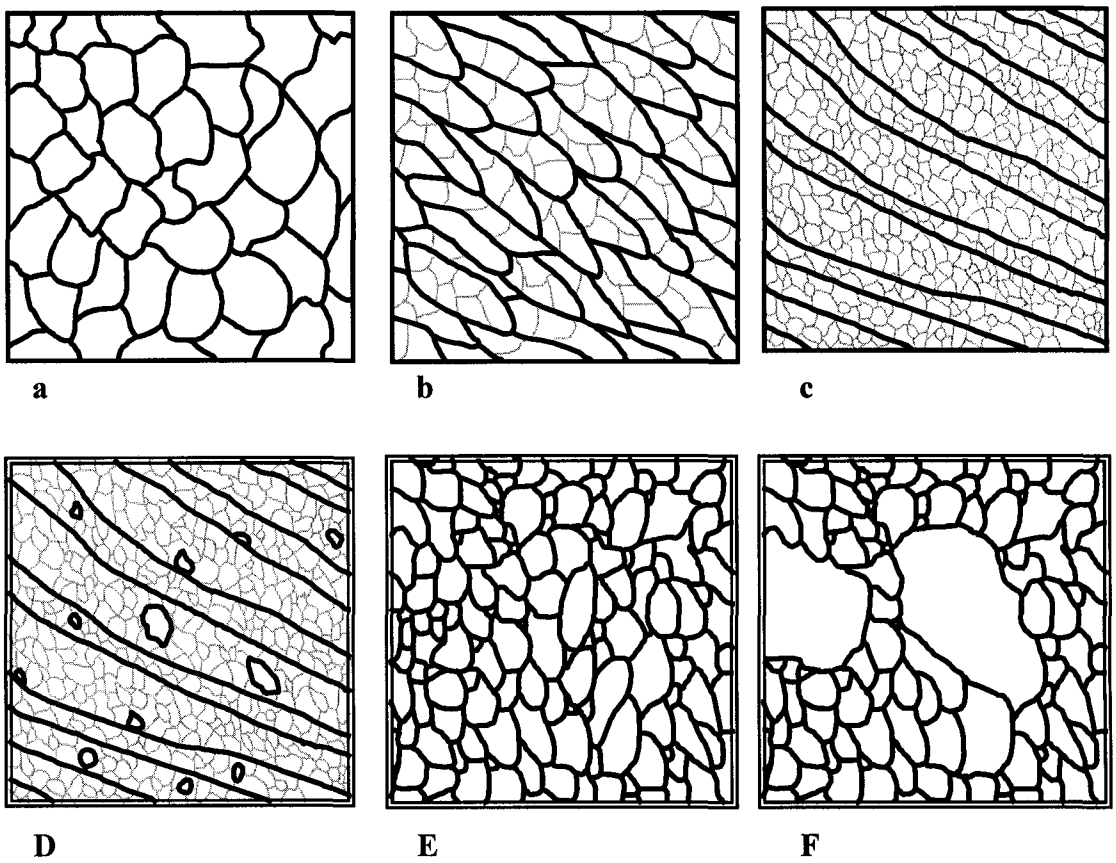

Figure 101: Summary of the author's interpretation of traditional theory for Peripheral Coarse Grain (PCG) structure formation. Frames a – c represent the microstructural evolution during deformation, while D – F represent the microstructural evolution during annealing. High angle grain boundaries are marked by dark lines and low angle grain boundaries by light gray.

Based on the results from physical simulation in this investigation, it can be seen that the formation of a coarse grained recrystallized structure is the result of an extremely complex set of mechanisms that must take place in succession. As a result of torsion experiments with very high quenching rates, it was determined that the alloys used in this research have the ability to form a fine, equiaxed grain structure as a result deformation to high strains. This has also recently been confirmed in the literature for a

similar alloy.[58] It stands to follow then, that an as-deformed microstructure that contains a fine, equiaxed grain morphology, can be used in the same regard as the grain structure following static recrystallization (Figure 101E). The differences in the structures, however, are the finer size of the grains, slightly higher aspect ratio, and presence of stored energy in the form of free dislocations. It should be noted that the presence of dislocations within the deformed fine equiaxed grains has not been confirmed in this research. In addition to the presence of the fine, equiaxed grain structure within the torsion specimens given a critical strain, the structure was also present within the DMZ and surface of extrudates from small – scale extrusion. Therefore, one can deduce that the grain assembly made up of the equiaxed grains, separated by high angle grain boundaries, provides an ideal precursor for abnormal grain growth to occur. Based on this assumption, a new theory for PCG structure development at the surface of an extrudate can be made as seen in Figure 102. In the early stages of deformation (Figures 102 a – c), the structure of the material behaves the same as the traditional context as seen in Figure 101 a – c. The main difference stems from the fact that at high strains, for example $\varepsilon_{eff.} > 2.5$ in the case of hot torsion, a fine equiaxed microstructure will develop (Figure 102d). At the end of deformation and as annealing begins, the as – deformed microstructure is made up of a high angle grain assembly. If the conditions for abnormal grain growth are met, as discussed in section 6.4, then abnormal grain growth will begin (Figure 102E) and consume the deformed microstructure until either quenching reduces the mobility of the moving boundary, or if the grain impinges on another broad high angle grain boundary (Figure 102F).

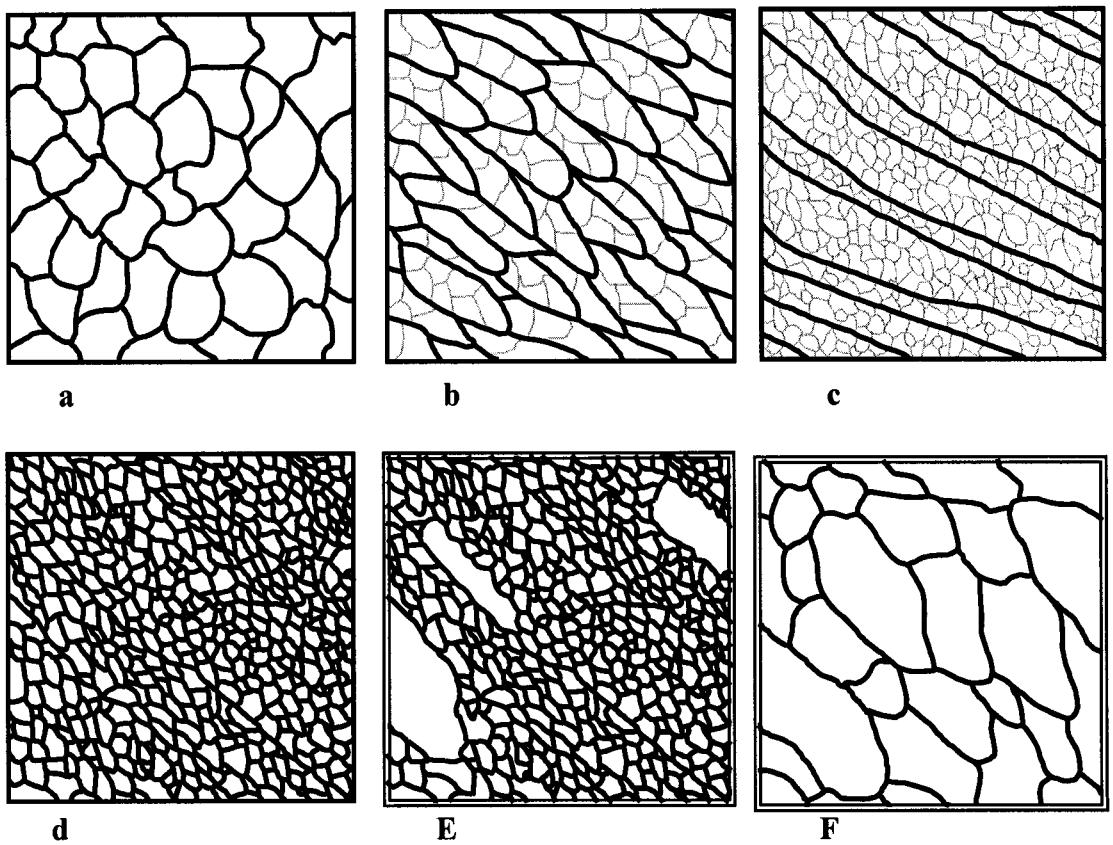

Figure 102: Proposed theory of Peripheral Coarse Grain (PCG) structure formation based on experimental results in this research. Frames a – d represent the microstructural evolution during deformation, while E – F represent the microstructural evolution during annealing. High angle grain boundaries are marked by dark lines and low angle grain boundaries by light gray.

6.4 Prediction of Coarse Grain Formation in Extrusion

Traditional models that predict the recrystallization behavior and kinetics of PCG structure development have been based on JMAK type relationships. Most JMAK kinetics data for industrial aluminum alloys are available for rolled non – heat treatable alloys such as 3xxx and 5xxx series. Additionally, most of this data have been

collected for rolled material that was annealed in a box or tube furnace. In general, the values of strain, strain rate and temperature have always been regarded as the most important values that determine the stored energy within the material. A decrease in the deformation temperature and increase in strain rate and strain all result in a higher dislocation density and therefore result in a higher stored energy. Upon annealing, the material releases the stored energy through annihilation of free dislocations (static recovery) and the nucleation and growth of new, dislocation free grains.

In an attempt to understand how best to predict the coarse grain depth in extrusion, a correlation between the depths from small – scale extrusion experiments are compared with well known deformation parameters. As a first attempt to predict the PCG depth of an extrudate, the value for average Zener Hollomon Parameter, $Z_{avg.}$, has been calculated based upon the extrusion conditions used in small – scale extrusion.

The average Z, Z_{avg}, for extrusion can be determined using a time average strain rate during extrusion, $\dot{\varepsilon}_{avg.}$ [59]:

$$\dot{\varepsilon}_{avg.} = \frac{6V \ln R}{D_b} \qquad (21)$$

where:

v = ram speed
R = extrusion ratio
D_b = starting billet diameter

This time average strain rate is used here to calculate the average Zener Hollomon parameter, Z_{avg} for extrusion using equation 2. Figure 103 shows a plot of

PCG depth measured from small – scale extrusion experiments in this research vs. log Z_{avg} calculated. It can be seen that there is no reasonable relationship that can be deduced from this approach. Therefore, an average Zener Hollomon parameter, based on a time average strain rate cannot be used. This may be primarily due to the fact that deformation in extrusion is extremely localized, especially at the surface of the extrudate rather than an average across the diameter. Therefore, a steep gradient in the strain, strain rate, and temperature of deformation will occur, as has been seen in this research.

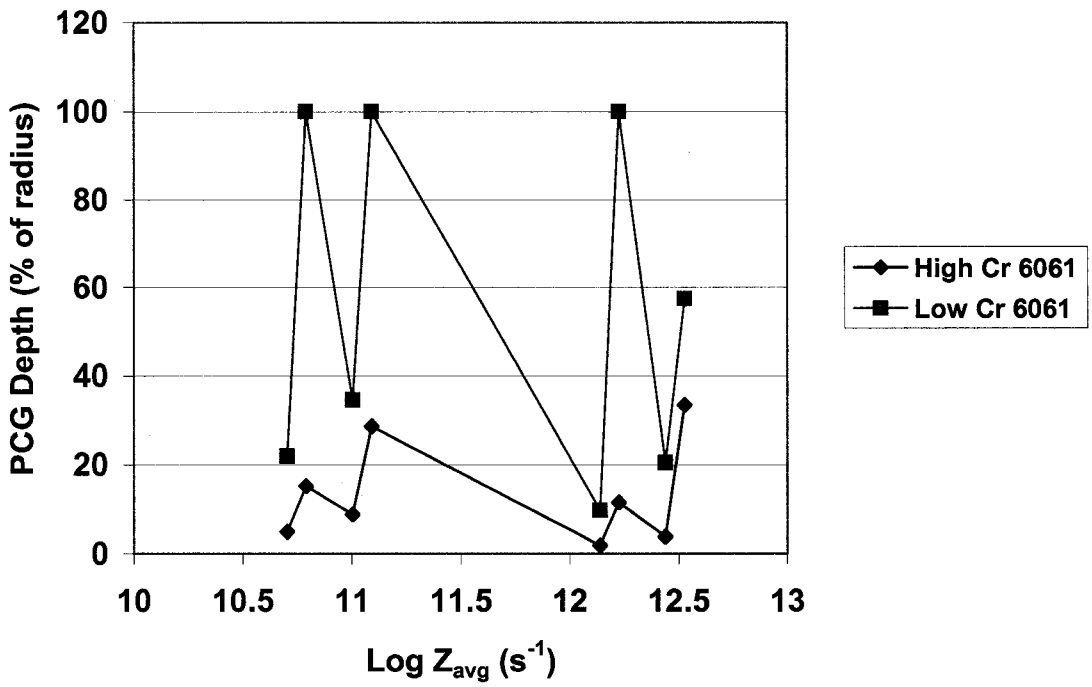

Figure 103: PCG depths measured from small – scale extrusion experiments as a function of the calculated average Zener Hollomon parameter, $Z_{avg.}$ for both alloys studied.

Most numerical models used in hot deformation are capable of producing material response data based on constitutive relationships from physical simulation. Numerical modeling results presented in Section 5.4 were used to determine the maximum Zener Hollomon parameter, Z, seen at the center and surface of extrudates in small – scale extrusion. The results are presented in Figure 104. It can be seen that the Zener Hollomon parameter, calculated using the maximum strain rate and deformation temperature, increases towards the surface and also with decreasing deformation temperature. However, the results from small – scale extrusion LOM characterization of PCG depths presented in Figures 34 and 35 showed that with increasing starting billet temperature, the PCG depth generally was higher, as was seen in similar research performed on the same alloys [57].

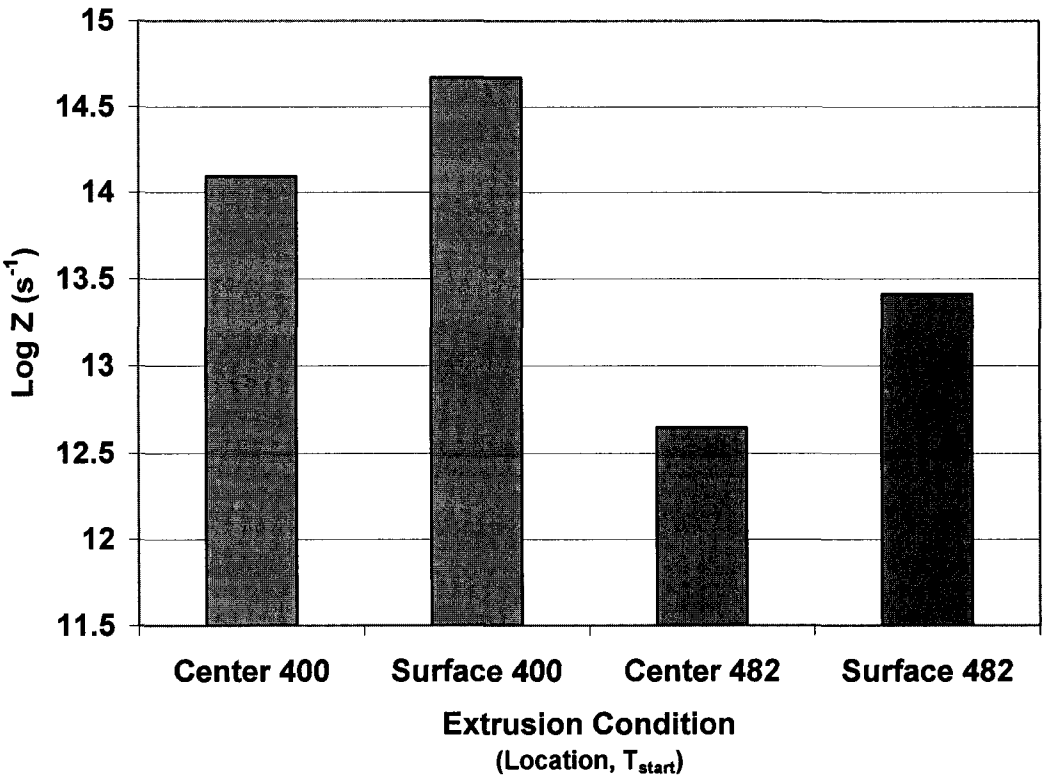

Figure 104: Plot of Log Z based on the maximum strain rate and temperature achieved at the center and surface of the extrusion from numerical simulation results.

The depth of coarse grains as a function of the maximum Zener Hollomon parameter at the surface for the same conditions (ram speed, extrusion ratio) is shown in Figure 105. It can be seen that the increase in the maximum Z at the surface results in a lower coarse grain depth. This relationship is the opposite of what is expected, whereby a higher Z should result in a higher stored energy and therefore more nucleation sites for recrystallization. Therefore, one cannot rely on localized values of Z alone as a fingerprint for PCG development.

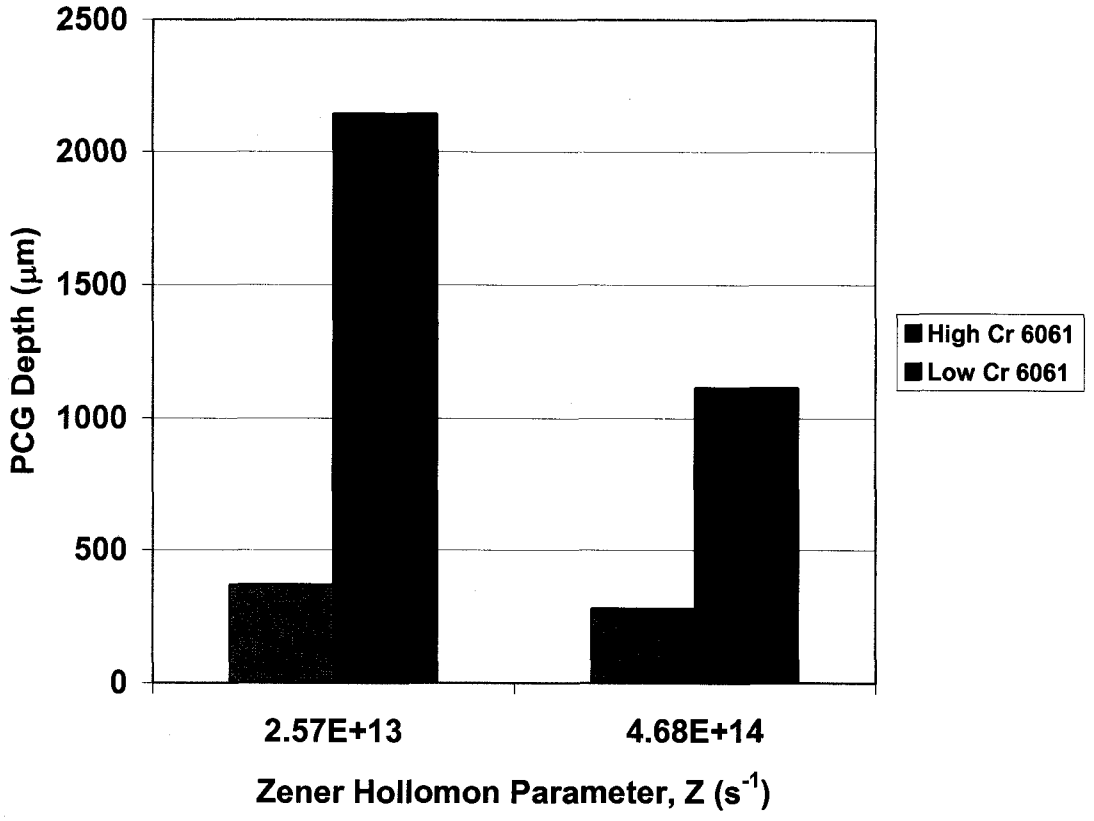

Figure 105: Depth of PCG versus values of the Zener Hollomon Parameter, Z at the surface of the extrudate based on Finite Element Model results. The extrusion parameters used were R = 40, and ram speed = 1.3 mm/s.

As was discussed in section 5.1.1 and 5.1.2, the microstructure at the surface of the extrudates in this investigation that had no PCG structure present were made up of fine, equiaxed grains with boundary misorientations greater than 15°. Additionally, the population of these fine, equiaxed grains also dramatically increased just before the PCG structure was encountered (Figure 45). Nucleation and growth, as it has been treated traditionally for aluminum alloy extrusion, of new grains is based upon a

structure that has high angle grain boundaries with significant substructure in the form of sub – boundaries. Models that have attempted to determine the depth of the PCG structure have relied on equations that relate the processing parameters to the microstructural evolution. These models have been introduced in section 2.2.1. In each model, the processing parameter used is the Zener Hollomon parameter, Z, which is then related to the subgrain size and subgrain misorientation in the deformed material. In contrast, in this research, the stored energy following hot deformation to large strains is not in the form of subgrains with low angle misorientation. Rather, the microstructure at the surface of the small – scale extrusion extrudates as well as the hot torsion samples with a $\varepsilon_{eff.} > 2.5$ consisted predominantly of high angle boundary grains and should therefore be treated as such when determining the annealing characteristics.

As mentioned in Section 6.2, it is proposed that the fine, equiaxed nature of the grains after high strains can be used as a precursor for abnormal grain growth and, thus, coarse grain formation. There is a distinct difference between the equiaxed grain structure of an as – deformed microstructure and one that has undergone traditional static nucleation and growth. First, the dislocation density of the cDRX/gDRX grain interior is likely higher than that of a statically recrystallized grain, although this would need to be confirmed by TEM investigation. Additionally, the grain boundary properties of the cDRX/gDRX grains are not known here beyond their misorientation angle. To the knowledge of the author, the difference in recrystallization kinetics between the cDRX/gDRX structure and that of a fibrous / banded microstructure with subgrains have never been studied.

As a first step to understanding the phenomenon of abnormal grain growth, a model from the literature is used here. Recently, Humphreys has developed a unified theory on recovery, recrystallization and grain growth based on the fundamental principles of a cellular structure [60]. The simple model, which is replicated here, uses a grain assembly as an example of a cellular structure with an average grain radius, $R_{avg.}$, average boundary mobility, $M_{avg.}$, and average grain boundary energy, $\gamma_{avg.}$. Under certain conditions, an individual special grain, which has its own grain radius, $R_{i.}$, boundary mobility, M_i, and grain boundary energy, γ_i, that are different from its surrounding grains is able to grow into the surrounding grain assembly.

In the absence of second phase particles, the average grain assembly will grow with a rate of:

$$\frac{dR_{avg.}}{dt} = \frac{M_{avg.}\gamma_{avg.}}{4R_{avg.}} \tag{22}$$

The growth rate of an individual special grain will be:

$$\frac{dR_i}{dt} = M_i\left(\frac{\gamma_{avg.}}{R_{avg.}} - \frac{\gamma_i}{R_i}\right) \tag{23}$$

When the presence of small particles that are able to pin the grain boundary movement is added, the particles will exert a pressure on the moving planar boundary as:

$$P_Z = \frac{3F_V\gamma}{d} \tag{24}$$

where:

F_v = volume fraction of pinning particles
d = diameter of pinning particles

In the case of the alloys used in this analysis, the Al(Cr,Mn)Si particles are primarily responsible for this pinning effect, due to their size, shape, and incoherent nature. The growth rates of the average grain assembly and the individual grain in the presence of the pinning particles is then:

$$\frac{dR_{avg.}}{dt} = \frac{M_{avg.}\gamma_{avg.}}{4R_{avg.}} - M_{avg.}P_{Z(avg.)} = M_{avg.}\gamma_{avg.}\left(\frac{1}{4R_{avg.}} - \frac{3F_v}{d}\right) \tag{25}$$

and

$$\frac{dR_i}{dt} = \frac{M_i\gamma_{avg}}{R_{avg}} - \frac{M_i\gamma_i}{R_i} - M_iP_Z = M_i\left(\frac{\gamma_{avg}}{R_{avg}} - \frac{\gamma}{R_i} - \frac{3F_v\gamma}{d}\right) \tag{26}$$

If the particle pinning term is replaced by a dimensionless parameter, W[1]:

$$W = \frac{P_{Z(avg)}R_{avg}}{\gamma_{avg}} = \frac{3F_vR_{avg}}{d} \tag{27}$$

then it follows that,

$$\frac{dR_{avg}}{dt} = \frac{M_{avg}\gamma_{avg}}{R_{avg}}\left(\frac{1}{4} - W\right) \tag{28}$$

and

$$\frac{dR}{dt} = M\left(\frac{\gamma_{avg}}{R_{avg}} - \frac{\gamma}{R} - \frac{W\gamma}{R_{avg}}\right) \tag{29}$$

According to this equation, normal grain growth will end when W = 0.25, thereby making $dR_{avg.}/dt = 0$. This condition is known as the particle limiting grain size R_{lim}:

$$R_{\lim} = \frac{d}{12F_v} \tag{30}$$

[1] In the derivation given by Humphreys, the dimensionless parameter used is Z. In order to avoid the confusion with the Zener Hollomon parameter, Z, the letter W is used here instead.

Physically, this limit represents the maximum average grain size for a grain assembly at a particular F_v / d ratio. Values of $R_{lim.}$ for different ratios of F_v / d are shown in Figure 106 and is denoted by the middle dashed line (W = 0.25). At values of W larger than 0.25, abnormal grain growth conditions are met, due to the restriction of the growth of the average grain assembly. From equation 26, it can be seen that abnormal grain growth will cease when W exceeds 1. At values of W less than 0.25, Humphreys notes that the grain assembly will undergo a broadening of the grain size distribution as well as normal grain growth.

Because of the simplicity of the model, there are many assumptions that must be made when using this model for grain structures in extrusion or torsion. First, the model is only applicable to high stacking fault energy materials such as aluminum. Second, there is an assumption that there is an average boundary mobility, $M_{avg.}$, and average grain boundary energy, $\gamma_{avg.}$ in the grain assembly. Since the gDRX grain structure has been highly deformed, it is not known how this type of structure affects $M_{avg.}$ and $\gamma_{avg.}$. The grain boundary energy is relatively constant at misorientations above 15°, and therefore it is assumed that the average grain assembly will therefore have an average grain boundary energy.

In the case of the extrusion and torsion surface microstructure encountered in this investigation, there was considerable evidence of abnormal grain growth (as discussed in Section 6.2). In order for abnormal grain growth to occur in a grain assembly, several conditions need to be met. First, a relatively homogeneous distribution (consistent interparticle distance) of stable particles needs to be in place to

exert the pinning pressure. This pinning pressure will stabilize the average grain assembly. Additionally, the abnormally growing grain must have some mobility advantage. Examples of this advantage are usually a special texture or some special grain boundary characteristic. In the case of the material encountered in this research, the texture of coarse grains in extrusion was typically Cube or Goss orientation, although several other deformation textures were present in the coarse grains. Finally, in a real microstructure, the individual special grain must have a size advantage over the average grains in the assembly.

Nevertheless, Humphreys has devised conditions in an average grain assembly where an abnormally growing grain will be favorable to grow. When the Humphreys model is used for the values of F_v / d in the alloys studied, an interesting prediction results. The case of the hot torsion microstructure from the low Cr 6061 alloy is shown in Figure 107. The approximate F_v / d for this alloy is marked by the solid vertical line. At a strain of 3.5, the resulting $R_{avg.}$(from Figures 90 and 91) for the high and low deformation temperature at the surface of the mid – gauge length are shown in Figure 107 as horizontal dashed lines. It can be seen that the material deformed at the higher deformation temperature has a larger $R_{avg.}$. Therefore, the conditions for normal and abnormal grain growth are met. The material deformed at the lower deformation temperature results in a lower $R_{avg.}$ and will only grow abnormal grains when the $R_{avg.}$ has grown and reached a values greater than W = 0.25. Therefore, at higher deformation temperatures (i.e., lower Z) coarse grain development based on abnormal grain growth theory is more favorable.

When the extrudate material exits the die, the average grain size at the surface will dictate whether coarse, recrystallized grains will grow. The annealing temperature and time will therefore play a role in how an abnormal grain will "nucleate." These results more closely represent the results from small – scale extrusion whereby a larger $R_{avg.}$ exists as a result of a higher starting billet temperature, and conditions for abnormal grain growth are more favorable. At the lower starting billet temperature, a much finer grain size will be expected and will result in a lower possibility of abnormal grain growth and therefore, less frequent coarse grain formation.

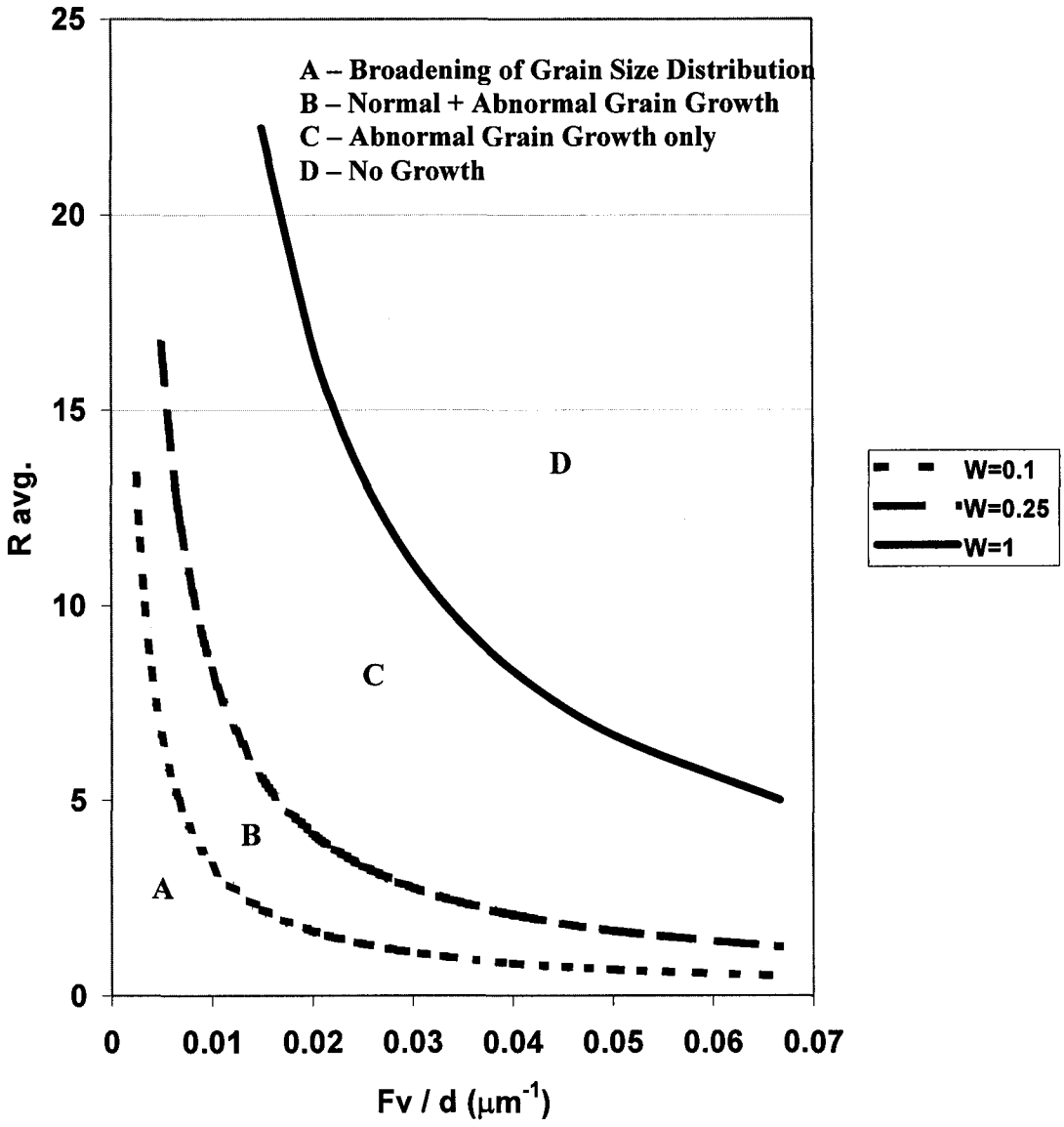

Figure 106: Average grain radius, $R_{avg.}$ as a function of volume fraction to particle diameter, F_v / d ratio. Lines represent regions where A) Broadening of Grain Size Distribution (W<0.1), B) Normal + Abnormal Grain Growth (0.1>W>0.25), C) Abnormal Grain Growth only (0.25>W>1), and D) No Growth occur (W>1).

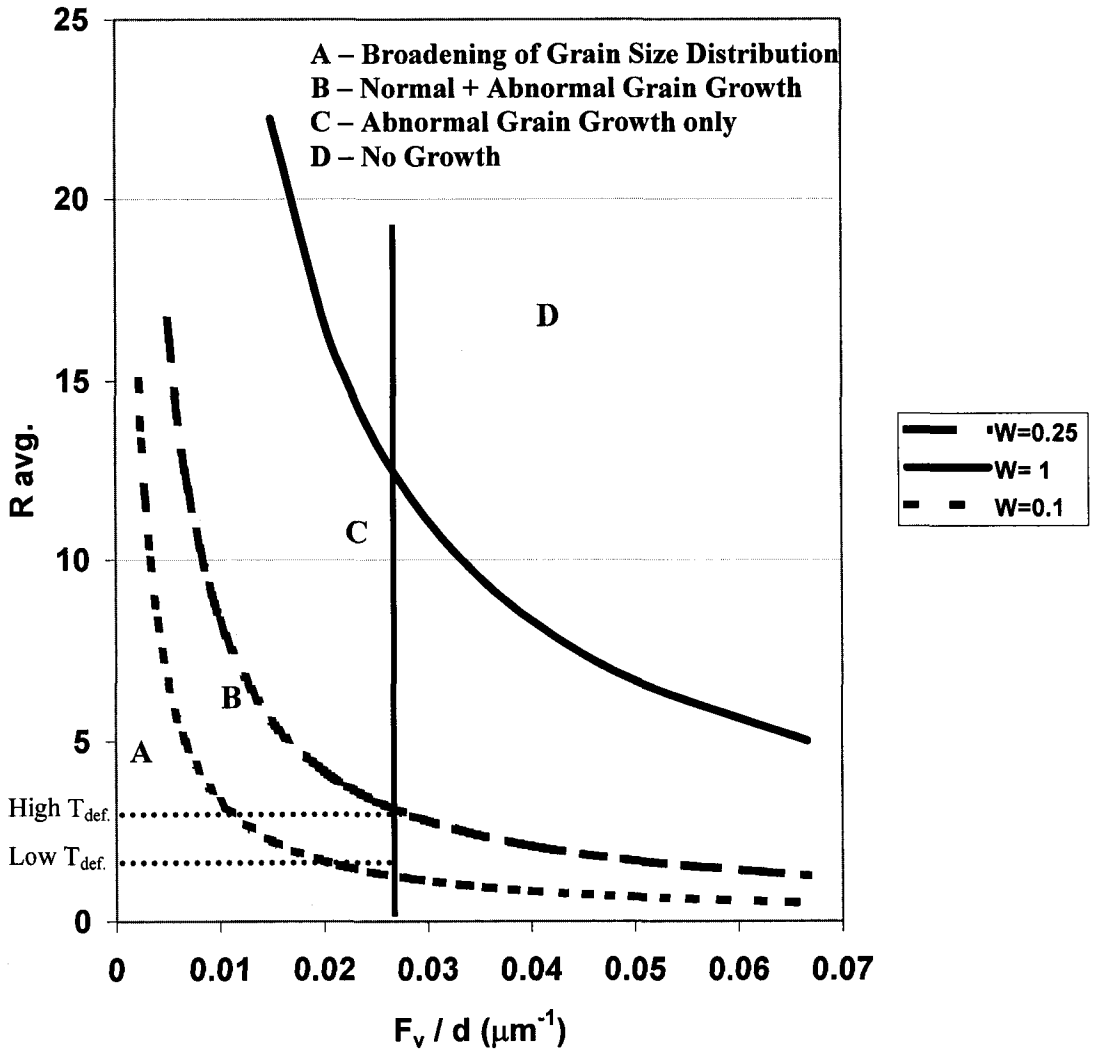

Figure 107: Average grain radius, $R_{avg.}$ as a function of volume fraction to particle diameter, F_v / d ratio. Lines represent regions where Normal Grain Growth, Abnormal Grain Growth, and No Growth occur. The F_v / d ratio for the low Cr 6061 alloy is shown as a dark vertical line. Average grain radius after high and low $T_{def.}$ torsion of the low Cr 6061 alloy are shown.

The model developed by Humphreys is used here as a first step to understanding the growth kinetics of coarse grains in the grain assembly of an extrudate's surface. A summary of the proposed general sequence necessary for coarse

grain development in a deformed structure for the alloys studied is shown in Figure 108. The starting material is made up of an average grain size with dispersoids of a particular diameter, d, and volume fraction, V_f. When the material is deformed under certain controlled processing conditions, the material response results in a unique microstructure. As described in Section 6.1, a fine, equiaxed microstructure can develop as a result of continuous dynamic recrystallization processes for the alloys studied. If the effective strain and Z are not adequate for continuous or geometric dynamic recrystallization, then the microstructure will be made up of deformation bands of high angle grain boundary misorientations and subgrain structure with a size and misorientation dependent on the deformation conditions. If the deformed microstructure undergoes cDRX or gDRX, then the microstructure will be made up of fine, equiaxed, predominantly high angle boundary grains with an average grain radius, $R_{avg.}$.

When deformation ceases, and the material is subjected to high ambient temperatures (i.e., after exiting the extrusion die, slow cooling after torsion, or annealed in a salt bath) then conditions may arise where the grain structure becomes unstable. In the case of the banded / fibrous grain structure, the deformed structure will likely recrystallize by traditional nucleation and growth mechanisms such as Particle Stimulated Nucleation, Strain Induced Boundary Migration, or subgrain coalescence.

In contrast, the microstructure that represents fine, equiaxed grains will follow the relationship presented in Figure 106 for a high angle boundary grain assembly. For a given F_v / d ratio, the grain assembly will be relatively stable below the curve of the

particle limiting grain size, $R_{lim.}$ As time progresses, the grain structure will grow until $R_{avg.}$ reaches the value where abnormal grain growth can take place. Once this condition is reached (W = 0.25), only abnormal grain growth is possible and no normal grain growth will occur due to particle pinning.

Abnormal grain growth will then continue until the material is quenched or when the abnormally growing grain impinges on a high angle planar boundary, such as another abnormal grain or a high angle deformation band. While the kinetics of abnormal grain growth mimic that of discontinuous static recrystallization, the actual kinetics for the fine, equiaxed grain structure here need to be further understood in order to make the model more applicable to the industrial processing conditions.

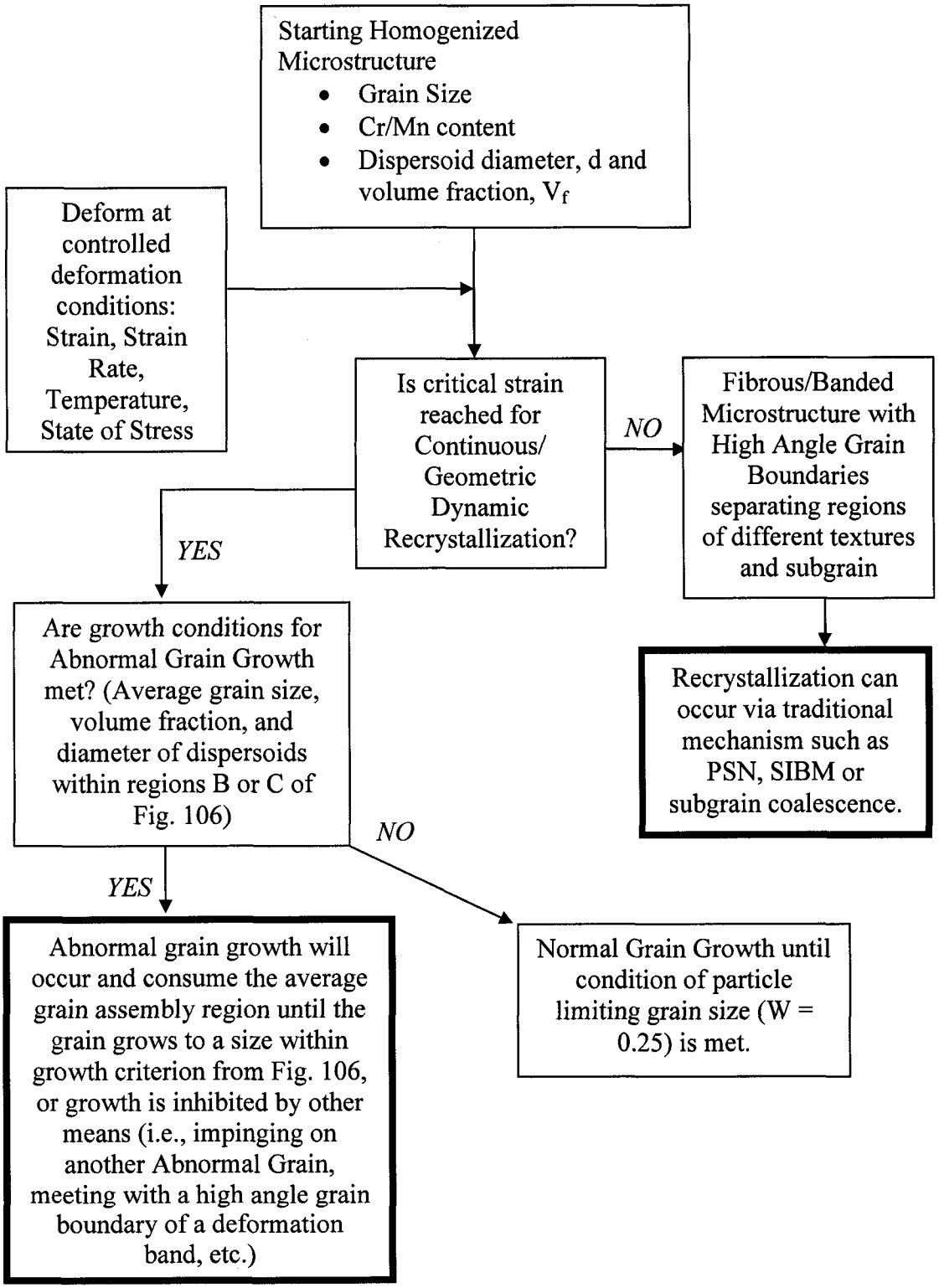

Figure 108: Flow chart showing conditions whereby Abnormal Grain Growth occurs in a high stacking fault material deformed to large strains.

7.0 CONCLUSIONS

The objective of this research was to understand the origin and metallurgical nature of the specific surface imperfection known as a Peripheral Coarse Grain (PCG) structure in extrusion of 6xxx series aluminum alloys. Based on the experimental results from small – scale and industrial scale extrusion, hot torsion testing and corresponding analysis of this research, the following conclusions can be made.

1) Based on results from small – scale indirect extrusion experiments, it was found that the depth of the PCG structure is related to the energy supplied to the deformed material. The PCG depth is also strongly related to processing parameters and increased with increasing ram speed, starting billet temperature, extrusion ratio, and a decrease in the amount of recrystallization inhibiting elements such as Cr. Additionally, industrial – scale direct extrusion confirmed that the depth of the PCG structure increases from the front to the rear of an extrudate. In both industrial and small – scale extrusion experiments, the size of the coarse recrystallized grains increased from the surface towards the center of the extrudate. It has been determined that the mechanism of coarse grain formation is a static process, due to the presence of coarse, recrystallized grains in the extrudate and absence in the discard. Through salt bath annealing experiments of water quenched extrudates, it was determined that the PCG structure forms very quickly, on the order of seconds after the material exits the die.

2) The Dead Metal Zone (DMZ) in indirect extrusion is comprised of a fine, equiaxed grain structure in a hemispherical shape after the billet has been extruded to 75% completion. The microstructure in the DMZ region after extrusion suggests that deformation conditions in the DMZ of an indirectly extruded billet are much more severe than have been assumed in visioplastic modeling research. At the die exit, the crystallographic orientation of the grains appears to rotate due to the imposed deformation conditions and develop a shear texture at the surface that most closely resembles a {332}<353> texture.

3) The as – extruded microstructure of an extrudate without any PCG structure results in a complex microstructure made up of a banded / fibrous region of high angle grain boundaries that separate regions of subgrains with alternating {121}<111> / {110}<111> orientations and {110}<001> / {100}<001> orientations. A fine, equiaxed microstructure exists at the surface of each extrudate in the absence of a PCG structure and is made up of high angle (>15° misorientation) boundaries. It was determined that the quantity of fine, equiaxed grains with diameters below 10 μm was relatively constant in the center of the extrudate and increased dramatically towards the surface just before the PCG structure is encountered. The texture at the surface of the extrudate in the absence of a PCG structure most closely resembles a {332}<353> texture. This texture is attributed to a {121}<111> orientation rotated approximately 45° about the normal direction due to the shear conditions at the die exit. The origin of this

texture has been confirmed in the EBSD analysis of the billet discard. When a PCG structure is present, the resultant texture is comprised of {100}<001> and {110}<001> orientations with other deformation textures present in lower amounts. The lack of a random texture at the surface signifies that Particle Stimulated Nucleation does not play a dominant role in the nucleation of PCG grains.

4) The results of hot torsion experiments revealed that the microstructure corresponding to the highest effective strain at the torsion sample surface resembles the fine, equiaxed structure seen in the DMZ and surface of the extrudates from small – scale extrusion testing. These grains are likely produced by a continuous dynamic recrystallization process such as geometric dynamic recrystallization. It can be reasonably concluded that the equiaxed grain microstructure is not a result of a static process due to the very high quenching rate after hot torsion testing. The critical effective strain for fine, equiaxed grain development in torsion was greater than 2.5 in torsion. At a strain of 3.5, it was determined that the as – deformed grain size decreased with higher values of Zener Hollomon parameter. The dominant mechanism of the break up of grainsat this strain appears to be cDRX at low values of Z and gDRX at high values Z. Further experimentation needs to be performed to understand the precise mechanisms as defined in the literature.

5) It was determined that traditional models for coarse grain development at the surface of 6xxx aluminum extrudate are fundamentally flawed because they are based on the premise that the microstructure is made up of subgrains with boundary misorientations <15°. Throughout this research, it has been found that the microstructure of the alloys studied grains after deformation to large strains (>~2.5) is comprised predominantly of high angle boundary (misorientation >15°). The microstructural development of coarse grain formation at the extrudate surface is the result of a complex series of microstructural phenomena that must occur in succession in order for abnormal grain growth to occur. A proposed theory for coarse grain development has been made, which is based on the microstructure development during deformation and subsequent annealing. The theory uses an abnormal grain growth model developed by Humphreys that relates the average diameter of the grain assembly to the volume fraction and diameter of dispersoids. For a given volume fraction and diameter of fine dispersoids, the model predicts that a microstructure that is made up of a high angle grain assembly with an average grain diameter will present ideal conditions for abnormal grain growth. The maximum and minimum grain diameters for abnormal grain growth are based on the geometry of the grains in relation to the particle dispersion.

8.0 FUTURE WORK

The conclusions made in this research have resulted in a fundamental change in the perspective of how coarse grains develop in extrusion of 6xxx series aluminum alloys. In order to fully understand how the microstructural evolution during deformation results in coarse grain formation at the surface, and how to predict the depth and characteristics of the coarse grain structure, there is a considerable amount of research work that still needs to be completed. The following future work is suggested.

In general, the mechanism of coarse grain development in this research has been based on the 6xxx aluminum alloy series. The results of this research should be used to study other alloy systems, particularly 2xxx and 7xxx aluminum alloys due to their significance in the aerospace industry. The much higher volume fraction of second phase particles will have a dramatic and complex effect on both the deformation and annealing behavior of these alloys.

8.1 Microstructural Evolution After Hot Deformation

The annealing characteristics of the as – extruded surface, which is made up of a unique microstructure, have rarely been studied. This microstructure is unique, because it is made up of highly misoriented equiaxed grains that have a strain history. While grain growth and abnormal grain growth kinetics of cast or statically recrystallized structures are comparatively well – studied, the annealing characteristics of an equiaxed deformed grain structure in the presence of small particles has not been

studied. Additionally, the theory of coarse grain development in extrusion presented here has only been based on the microstructure at the surface of the extrudate. The mechanism of very large isolated recrystallized grains forming at the subsurface and center of the extrudate represent a very complex situation where a combination of subgrains and high angle boundary grains are present. It is not known whether the model of abnormal grain growth shown in this research will apply to microstructures of mixed grain / subgrain structure.

Additionally, the results from small – scale indirect extrusion showed very unusual metal flow behavior, especially in the vicinity of the DMZ. Further analysis of the DMZ evolution during extrusion as well as an explanation of the occurrence of fine grained microstructure in this region need to be made and are already underway.

8.2 Coarse Grain Development Based on Abnormal Grain Growth Theory

The results from this investigation suggest that the dominant mechanism for coarse grain development in extrusion of 6xxx series aluminum alloys is based on the growth of individual, special grains that consume an average grain assembly at the surface. The model developed assumes that there exists an average grain boundary energy, γ_{avg}, and average grain boundary mobility, M_{avg} in the grain assembly. While the grain boundary energy is relatively constant above boundary misorientations of 15°, the mobility of these grains is not known. Additionally, the model assumes a relatively low dislocation density within the surface grains due to the high stacking fault energy of the material and elevated deformation temperature. It would be interesting and

beneficial to investigate the substructure and grain boundary properties of the surface grains by Transmission Electron Microscopy (TEM) to determine their properties.

It is suggested that future experimentation should concentrate on annealing of the fine, equiaxed deformed grain structure to understand the influence of annealing time and temperature on the texture development and kinetics of abnormal grain growth. While salt bath annealing experiments are ideal for comparing microstructures at similar times, it is not viable as a basis for kinetics data due to the lack of isothermal conditions. Instead, annealing experiments performed on a Gleeble thermo – mechanical simulator will provide the most accurate data of recrystallization kinetics. For example, following hot torsion testing, if the thermocouple is not lost during high strain rate testing, the Gleeble is capable of maintaining the deformation temperature for iterative times after deformation ceases. The kinetics and characteristics of abnormal grain growth can easily be obtained from these experiments, provided that a means of maintaining the thermocouple following deformation is possible.

The ultimate goal of the research direction initiated by this project is to develop a quantitatively predictive model for coarse grain development in extrusion. It was found in the course of this research that current commercially available numerical modeling packages do not have the capability to predict microstructures resulting from large strain deformation. The algorithms that are the basis of these modeling packages are much too broad and are based on generalized deformation and annealing constitutive relationships. If a predictive algorithm is made, it must take into large account the microstructural development during deformation.

Finally, the model of coarse grain development can be used in other applications, as has been identified in the literature. The most promising impact will be on the annealing characteristics of friction stir welded aluminum alloys. The fine grain nature of the deformed material following friction stir welding is analogous to the microstructure of the extrudate surface in this research. Many of the underlying mechanisms of microstructural evolution and annealing kinetics between these two processes overlap. Additionally, the production of aluminum alloys via hot rolling results in coarse grain formation at the surface under specific processing conditions. The same microstructural model for surface deformation and annealing will likely apply to hot rolling of aluminum alloys if large surface strains are encountered.

8.3 Industrial Extrusion

The physical simulation experiments in this research have been based on small – scale indirect extrusion. While indirect extrusion has industrial significance, the impact of the direct extrusion process has much more potential for economic and energy savings due to its higher production capacity. The industrial – scale extrusion experiments performed in this research did not have the capability to fully verify the results from small – scale extrusion experiments. Nevertheless, the results from small – scale extrusion and hot torsion experiments have shown how 6xxx series aluminum alloys that are deformed to large strains have the potential to develop a coarse grain recrystallized microstructure. In direct extrusion, the metal flow is markedly different and the origin of the extrudate surface typically lies in the shear intensive zone,

depending on the die design. The shear intensive zone in direct extrusion is an ideal region for fine, equiaxed grain development due to the large strain imposed.

9.0 REFERENCES

1. The Aluminum Association, *Aluminum Statistical Review for 1999*, Washington, D.C., 1999.

2. G. E. Dieter, Mechanical Metallurgy, McGraw Hill, New York, 3rd. Edition, 1986, p. 617.

3. K. Laue and H. Stenger, Extrusion, ASM International, Metals Park, OH, 1976.

4. P. Saha, Aluminum Extrusion Technology, ASM, Metals Park, OH, 2000, p. 26.

5. H. Valberg, "A Modified Classification System for Metal Flow Adapted to Unlubricated Hot Extrusion of Aluminum and Aluminum alloys," Proceedings of the 6th International Aluminum Extrusion Technology Seminar, Chicago, IL, Vol. II, 1996, p. 95.

6. H. Valberg, "Surface Formation in Al-Extrusion (Direct Extrusion)," Proceedings of the 4th Aluminum Extrusion Technology Seminar, Chicago, IL, vol. I, 1988, p. 309.

7. M. Lefstad, O. Reiso Vidar Johnsen, "Flow of the Billet Surface in Aluminum Extrusion," Proceedings of the 5th Aluminum Extrusion Technology Seminar ET '92, Chicago, IL, vol. I, 1992, p. 503.

8. R.D. Doherty, D.A.H., F.J. Humphreys, J.J. Jonas, D.J. Jensen, M.E. Kassner, E. King, T.R. McNelley, H.J. McQueen, A.D. Rollett, Materials Science and Engineering A, vol. A238, 1997.

9. M.A. Zaidi, J.A. Wert, Treatise on Materials Science, vol. 31, p. 137 – 168.

10. M. Hatherly, F. Humphreys, Recrystallization and Related Annealing Phenomena, ed. Pergamon, New York, 1995, p. 372.

11. C.M. Sellars and W.J. Tegart, International Metallurgical Reviews, vol. 17, 1972, p. 1.

12. H.J. McQueen, E. Evangelista, J. Bowles, G. Crawford, Metal Science, vol. 18, 1984, p.395.

13. R.D. Doherty, D.A.H., F.J. Humphreys, J.J. Jonas, D.J. Jensen, M.E. Kassner, W.E. King, T.R. McNelley, H.J. McQueen, A.D. Rollett, Materials Science and Engineering A, vol. A238, 1997.

14. H. Yamagata, Acta Materialia, Vol. 43, No. 2, 1995, pp. 723 – 729.

15. K.J. Gardner and R. Grimes, Metal Science, 1979, p. 216 - 222.

16. M. Hatherly, F. Humphreys, Recrystallization and Related Annealing Phenomena, ed. Pergamon, New York, NY, 1995, p. 364, 371.

17. R.D. Doherty, D.A.H., F.J. Humphreys, J.J. Jonas, D.J. Jensen, M.E. Kassner, W.E. King, T.R. McNelley, H.J. McQueen, A.D. Rollett, Materials Science and Engineering A, vol. A238, 1997, p. 226.

18. A. R. Bandar, S.R. Claves, W.Z. Misiolek J. Lu, A.M. Maniatty, and K.Matous, "A Methodology for Quantitative Three-Dimensional Comparison of Experimental and Computer Simulated Microstructural Textures of 6xxx Aluminum Alloys," Proceedings of the 8th International Extrusion Technology Seminar, Orlando, FL, 2004, (in press).

19. G.C. Hasson and C. Goux, Scripta Metallurgica, vol. 5, 1971, p. 889.

20. W.T Read, Dislocations in Crystals, McGraw Hill, New York, 1953.

21. H.E. Vatne, T. Furu, R. Orsund, E. Nes, "Modelling Recrystallization After Hot Deformation of Aluminum," Acta Materialia, vol. 44, No. 11, 1996, p. 4463.

22. T. Pettersen, H. Vatne, T. Furu, E. Nes, Materials Science Forum, vol. 331 – 337, 2000, p. 805

23. X. Duan and T. Sheppard, "The Influence of Die Shape on the Behavior of Surface Recrystallization," TMS Annual Meeting: Hot Deformation of Aluminum Alloys, May 2003, p. 99.

24. M.A. Zaidi, J.A. Wert, Treatise on Materials Science, vol. 31, p. 137 – 168.

25. F. Perocheau and J.H. Driver, International Journal of Plasticity, vol. 16, 2000, p. 73 – 89.

26. T. Aukrust, S. Tjotta, H.E. Vatne, P. Van Houtte, International Journal of Plasticity, vol. 13, 1997, p. 111 – 125.

27. M.A. Wells, D.J. Lloyd, I.V. Samarasekera, J.K. Brimacombe, E.B. Hawbolt, Metallurgical and Material Transactions B, vol. 29B, 1998, p. 621.

28. J. Hirsch, K. Lucke, Acta Metallurgica, vol. 36, 1988, p. 2863.

29. M. Hatherly, F. Humphreys, Recrystallization and Related Annealing Phenomena, ed. Pergamon, New York, NY, 1995, p.15.

30. C. Maurice, J.H. Driver, Acta Materialia, Vol. 45, No. 11, p. 4627.

31. R.D. Doherty, D.A.H., F.J. Humphreys, J.J. Jonas, D.J. Jensen, M.E. Kassner, W.E. King, T.R. McNelley, H.J. McQueen, A.D. Rollett, Materials Science and Engineering A, vol. A238, 1997, p.221.

32. R.D. Doherty, D.A.H., F.J. Humphreys, J.J. Jonas, D.J. Jensen, M.E. Kassner, W.E. King, T.R. McNelley, H.J. McQueen, A.D. Rollett, Materials Science and Engineering A, vol. A238, 1997, p.252.

33. S. Gourdet, F. Montheillet, "A Model of Continuous Dynamic Recrystallization," Acta Materialia, vol. 53, 2003, p. 2685.

34. C. Chovet, S. Gourdet, and F. Montheillet, "Large Strain Deformation Textures and Microstructures of an Al-Mg-Si Alloy," Materials Science Forum, vol. 331 – 337, 2000, p. 733.

35. H.J. McQueen O. Knustad, N. Ryum, and J.K. Solberg, "Microstructural Evolution in Al Deformed to Strains of 60 at 400 deg C," Scripta Mat., vol. 19, 1985, p. 73.

36. F.J Humphreys, Proc. 6th International conference of Strength of Metals and Alloys, e.d. Gifkins, Melbourne, Australia, vol. 1, 1982, p.625.

37. M. Hatherly, F. Humphreys, Recrystallization and Related Annealing Phenomena, ed. Pergamon, New York, NY, 1995.

38. McQueen, et al, Mat. Sci. & Engr. A, 2000.

39. The Aluminum Association, Aluminum Standards and Data, 1997.

40. J. H. Hatch, Aluminum: Properties and Physical Metallurgy (Metals Park, OH: American Society for Metals, 1984), 64.

41. J. W. Martin, Micromechanisms in Particle – Hardened Alloys, (Cambridge University Press, 1980).

42. R. Jeneski, "Effects of Cr Addition on the Microstructure and Mechanical Behavior of 6061 – T6 Continuously Cast and Rolled Redraw Rod," Materials Science and Engineering, A237, (1997), 52 – 64.

43. L. Lodgaard, N. Ryum, "Precipitation of Dispersoids Containing Mn and/or Cr in Al-Mg-Si Alloys," Materials Science and Engineering, A283, (2000), 144 – 152.

44. C.S. Smith, Transactions of the Metallurgical Society of AIME, American Society for Metals, vol. 175, p. 15, 1948.

45. E. Nes, N. Ryum, and O. Hunderi, Acta Metallurgica, vol. 33, p.11, 1985.

46. F.J. Humphreys, Acta Metallurgica, vol. 25, 1977, p. 1323.

47. F.J. Humphreys and P.N. Kalu, Acta Metallurgica, vol. 35, 1987, p. 2815.

48. P. Saha, Aluminum Extrusion Technology, ASM, Metals Park, OH, 2000, p.285.

49. T. Furu, H.E. Vatne, "Grain Structure Control of Flat Extruded AA6082 Alloy," Materials Science Forum, vol. 331 – 337, 2000, p. 843.

50. W. Libura, J. Zasadzinski, Proceedings of the 5th Aluminum Extrusion Technology Seminar ET '92, Chicago, IL, AA & AEC, vol. II, 1992, p.485 – 494.

51. H. Yang, Proceedings of the 7th Aluminum Extrusion Technology Seminar ET '00, Chicago, IL, AA & AEC, vol. I, 2000, p.371 – 380.

52. K. Laue and H. Stenger, Extrusion, ASM International, Metals Park, OH, 1976.

53. D. Ackland, Lehigh University, Private Communication.

54. Stuart Wright, EDAX/TexSEM Laboratories, Private Communication.

55. J. Suni, T. Rouns, "Dispersoid Evolution During Homogenization of 6xxx Alloys," Materials science Forum, vol. 396 – 402, 2002, p. 687.

56. H. Browne, "Evolution of Dead Metal Zone During Indirect Extrusion of 6061 Aluminum Alloy," M.S. Thesis, Lehigh University, April 2004.

57. W. Van Geertruyden, W. Misiolek, P. Wang, in ASM Conference, Pittsburgh, PA, October, 2003.

58. T. Pettersen, B. Holmedal, and E. Nes, "Microstructural Development during Deformation of Aluminum to Large Strains," Metallurgical and Materials Transactions A, vol. 34A, 2003, p. 2737.

59. G. E. Dieter, Mechanical Metallurgy, McGraw Hill, New York, 3rd. Edition, 1986, p.628.

60. F.J. Humphreys, "A Unified Theory of Recovery, Recrystallization and Grain Growth, Based on the Stability and Growth of Cellular Microstructures – II. The Effect of second Phase Particles," Acta Materialia, vol. 45, No. 12, 1997, p. 5031.

VITA

William was born to Herman and Annette Van Geertruyden on April 17, 1976 in Pittsburgh, PA. Upon graduating from Berkeley Preparatory School in Tampa, FL in 1994, William began attending Lehigh University with an interest in engineering. He graduated in June of 1998 with a Bachelor of Science degree in Materials Science and Engineering. In May of 2000, William graduated with a Master of Science in Materials Science and Engineering from Lehigh University. Throughout his graduate career, William has been a co – author of over 15 technical papers and presented at conferences both domestically and abroad. Upon completing his degree requirements, William plans to be employed full time by a company he co – founded, EMV Innovative Material Technologies, LLC.